

Department of Precision and Microsystems Engineering

Thermally Programmable Multi-stable Mechanical Metamaterial

Maurita Bloembergen

Report no : 2025.010
Coaches : P. Roberjot MSc, H.M. Bilyalova MSc
Professor : Dr. Ir. M. Tichem
Specialisation : High-Tech Engineering
Type of report : Master Thesis
Date : 28-03-2025

Abstract

Until recently, multi-stable mechanical metamaterials have been primarily used in passive energy absorption systems. However, the ability to actively program these structures has gained significant interest, expanding their functionality to enable on-demand adaptive deformation. While existing active programming methods effectively induce global state transitions, localized actuation remains largely unexplored. This study introduces a novel approach to actively programming multi-stable metamaterials via local thermal stiffness modulation at boundary conditions. Using a polymer bi-material design with distinct glass transition temperatures between the beam and boundary supports, the system can transition from a bi-stable to a mono-stable state, enabling controlled snap-back behaviour after deformation. An analytical model is developed to characterize the snap-through behaviour of the unit cell, providing insight into the geometric interactions and sensitivities associated with various design parameters. Experimental implementation, using multiple additive manufacturing techniques, revealed key limitations and design considerations. In particular, the importance of constraining the second buckling mode and careful material selection emerged as fundamental design requirements for ensuring functionality. This work contributes to the growing field of actively programmable mechanical metamaterials, with implications for compact motion systems in future work.

Acknowledgements

I would like to express my sincere gratitude to those who supported me throughout the process of my thesis. First and foremost, I want to deeply thank my supervisors, Marcel, Pierre, and Hava. Marcel provided me with constant guidance and enthusiasm for the research, which motivated me to persevere through difficulties. Pierre was always available for brainstorming sessions and offered valuable insights, while Hava encouraged me to consider different perspectives and was a constant source of support. Together, I am incredibly grateful for their invaluable supervision. I also want to extend my appreciation to the PME lab technicians, especially Patrick and Bradley, for their assistance in setting up the experimental framework. They were always willing to help me navigate obstacles and find practical solutions. Additionally, I am grateful to everyone involved in the MECOMOS meetings for their insightful discussions, which broadened my perspective on the topic. Lastly, I would like to thank my friends and family for their encouragement and support throughout this journey.

Contents

Abstract	i
Acknowledgements	ii
1 Introduction	1
1.1 Mechanical metamaterials	1
1.2 Bi- and multi-stability	3
1.3 Thesis research goal	7
2 Exploration of local one-directional programmability	11
2.1 One-directional programmability	11
2.2 Framework stimuli responsive actuation	12
2.3 Concept overview	13
2.4 Stimulus evaluation	15
2.5 Thermally programmed transducers	17
3 Design	22
3.1 Thermal softening as a programming approach	22
3.2 Detailed design	23
4 Modelling	26
4.1 Analytical model	26
4.1.1 Fixed-Fixed boundary conditions	26
4.1.2 Variable stiffness boundary conditions	30
4.1.3 Bi-material boundary conditions	33
4.1.4 Influence of beam material on stability	36
4.2 Finite Element Model	38
4.2.1 Variable stiffness boundary conditions	39
4.2.2 Temperature dependent stiffness	41
4.2.3 Example simulation of Actively Programmed Multi-Stable Structure	43
5 Experimental implementation	45
5.1 PolyJet printing	45
5.1.1 DMA PolyJet Materials	46
5.1.2 Printed samples PolyJet	47
5.2 Fused Filament Fabrication	50
5.2.1 DMA FFF Materials	50
5.2.2 Printed samples FFF	52
5.3 Heat application	52
6 Discussion	55
6.1 Influence of testing conditions	55
6.2 Influence of material properties	57
6.3 Refined flow chart of programming approach	60
7 Conclusion	62
7.1 Recommendations	63
References	65
A Literature review	70
A.1 State of the art passive programmability	70
A.2 State of the art active programmability	72

B Continuation of Analytical Model fixed-fixed boundary conditions	75
C Passive vs Active programmability	77

1

Introduction

Metamaterials are materials that exhibit enhanced or exotic macro-properties primarily due to an engineered microstructure, as opposed to their material composition alone [1, 2]. The term *engineered* (or *architected*) refers to the idea that the micro-structure is rationally designed by a human (or algorithm) with a particular function in mind. For example, the metamaterial can be designed to have specific properties for optical, mechanical, acoustic or electrical functionalities [3–5]. It is further important to note that the use of *micro* and *macro* refers to a general distinction between the scale at which the material’s structure is built (micro) and the scale at which its behaviour is observed (macro) [6]. Typically, metamaterials consist of assemblies of one or more materials arranged in repeating hierarchically structured geometric patterns [7]. This repeated microstructure is often based on a designed unit cell, as illustrated in fig. 1.1. The unit cell can be considered the fundamental building block, with its geometry playing a key role in determining the properties of the material. Metamaterials can be constructed at various length-scales (nano- to centimetre) and can also possess multi-scale arrangements [8]. However, there is some debate on which scale separates metamaterials from meta-structures. In this work, the term metamaterial will be applied regardless of scale, as the design principles explored here are intended to be scalable and potentially miniaturised in future developments.

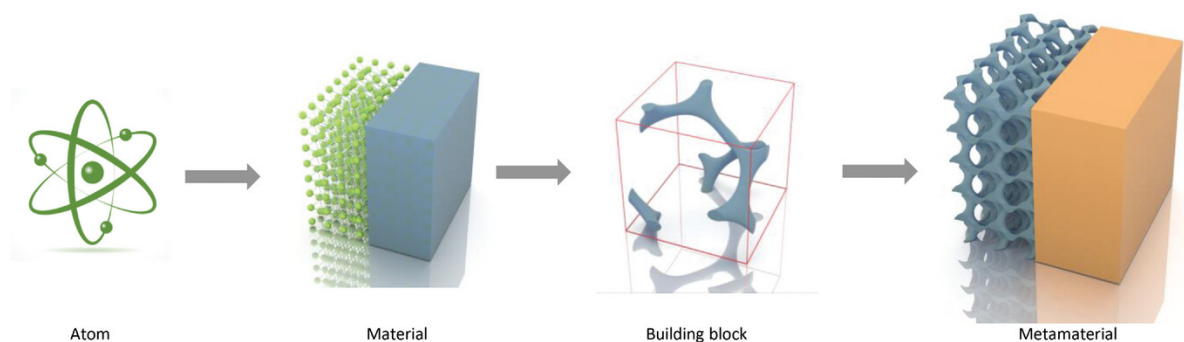


Figure 1.1: Typical build up of a metamaterial whereby the unit cell is labelled as building block [9]

1.1. Mechanical metamaterials

Among the different classes of metamaterials, mechanical metamaterials are specifically designed to enhance mechanical responses, such as achieving ultra-stiffness or ultra-lightweight properties [10]. However, their potential extends beyond mere enhancement, as they can also exhibit exotic and multifunctional behaviours, including properties that are rarely found in nature [11]. Notable examples include auxetics, negative compressibility, negative thermal expansion, and a vanishing shear modulus [6]. One of the earliest studies on synthetic auxetic materials was conducted by Lakes, who demonstrated these properties in polyurethane foams [12]. Auxetic materials possess a negative Poisson’s ratio, meaning they expand in the transverse dimension when subjected to an axial tensile load, in contrast to most natural materials which contract in transverse dimensions under the same conditions [6]. fig. 1.2

illustrates an idealized unit cell characterized by re-entrant behaviour from Lakes' original paper. The "re-entrant behaviour" refers to the structure possessing the capability to fold inward upon itself when subjected to compression, thereby exhibiting a negative Poisson's ratio.



Figure 1.2: Idealized unit cell of Lakes' auxetic foam [12]

Giving materials a designed structure to achieve enhanced properties is not necessarily a new development [13]. However, thanks to the advancement of additive manufacturing (AM), more complex and smaller architected structures have become obtainable [8]. By changing the structure at the scale at which the "size-effect" takes place (nano-scale) it is possible to tailor the mechanical properties of a material and optimize them for specific applications. In a broad sense, by using metamaterials, an engineer is no longer limited by the molecular composition of a material. Furthermore, the research of mechanical metamaterials is important not only because of the technological advancement but also because smart artificial materials could play a vital role in sustainable innovation [14].

There are several ways to classify mechanical metamaterials. One common distinction is made on the structural level, according to the design of the unit cells. In this manner, mechanical metamaterials can be categorised as origami, chiral, and lattice metamaterials [15]. This classification is illustrated in fig. 1.3. Numerous other studies have attempted to classify mechanical metamaterials, each proposing its own definitions and categorization schemes [6, 8, 15–17]. This variety of classifications suggests that no strict or universally agreed-upon framework currently exists.

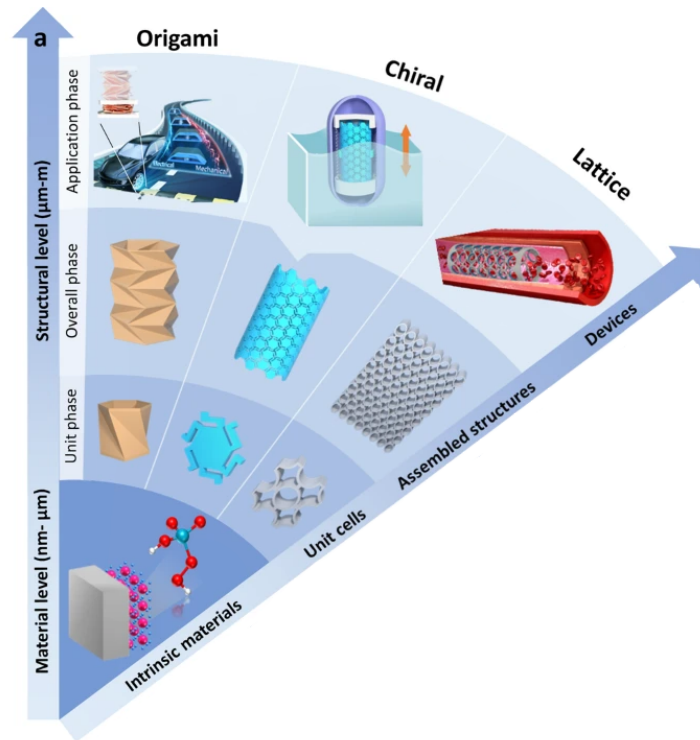


Figure 1.3: An example of structural classification of mechanical metamaterials. The unit phase, assembled form and an application is presented for each class [15].

Origami metamaterials are essentially mechanisms made up of plates linked by compliant hinges based on folded 2D sheets to form 3D structures. The general shape and properties of these types of metamaterials can be controlled by the order, number, and orientation of the folds [8]. Chiral metamaterials get their name from the chiral connections between periodic polygons [2]. They lack any planes of mirror symmetry. Lattice metamaterials are structures composed of multiple tessellated lattice elements, periodically assembled [15].

1.2. Bi- and multi-stability

A popular property explored in mechanical metamaterials is bi- or multi-stability. Bi-stable mechanisms, as the name suggests, possess two stable states. This means that the mechanism can shift from one stable state to another stable state when mechanically deformed beyond a certain energy threshold without requiring a continuously applied load (or other stimuli) to keep it in that deformed position [18]. To visualise this, a common bi-stable household object is a hairpin that is slightly bent upward. When pressing down on the curve, first a high resistance is experienced until it clicks or snaps into the stable downward position [19]. The stable states of the bi-stable mechanism can be recognized by the two local minima of potential energy pictured in fig. 1.4b [20]. As can be seen, at d_I the force versus displacement slope transitions from positive to negative. This is the point at which the mechanism starts to experience negative stiffness ($\frac{N}{m}$), until it reaches a new stable position at stage *III* where the force is zero and the slope is positive. This phenomenon, which in other circumstances can be an unwanted nuisance, is considered Euler buckling. However, buckling in this context is a desired effect, which is controlled and reversible. A mechanism can also exhibit pseudo bi-stable, or snap-through mono-stable, behaviour whereby the system self-recovers as the load is released. This can be seen in fig. 1.4C. Although the mechanism displays negative stiffness beyond F_{max} , the force never reaches a negative value, which means that the beam will snap-back upon the release of the load.

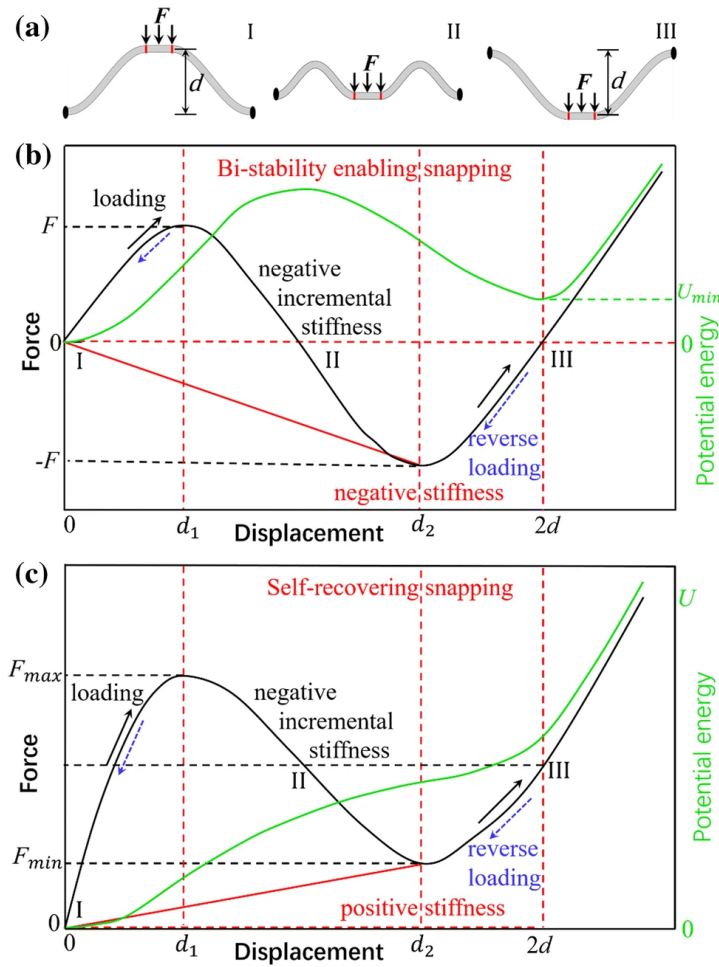


Figure 1.4: (a) Schematic and (b) graphical representation of bi-stability. (c) graphical representation of a self-recovering snapping mechanism (note that the force never reaches a negative value) [19]

Mechanical metamaterials can exhibit multi-stability when composed of bi-stable unit cells arranged in series and parallel. Additionally, individual unit cells themselves can be multi-stable in one or more degrees of freedom [21, 22]. This study focuses specifically on multi-stable mechanical metamaterials with single-degree-of-freedom bi-stable unit cells. These unit cells exist in various forms, as summarized by Xu et al. in fig. 1.5 [23]. Their classification distinguishes between 1D bi-stable structures, such as beams, trusses, and compliant mechanisms (first row), and 2D bi-stable shell structures, including curved surfaces and thin shell designs (second row).

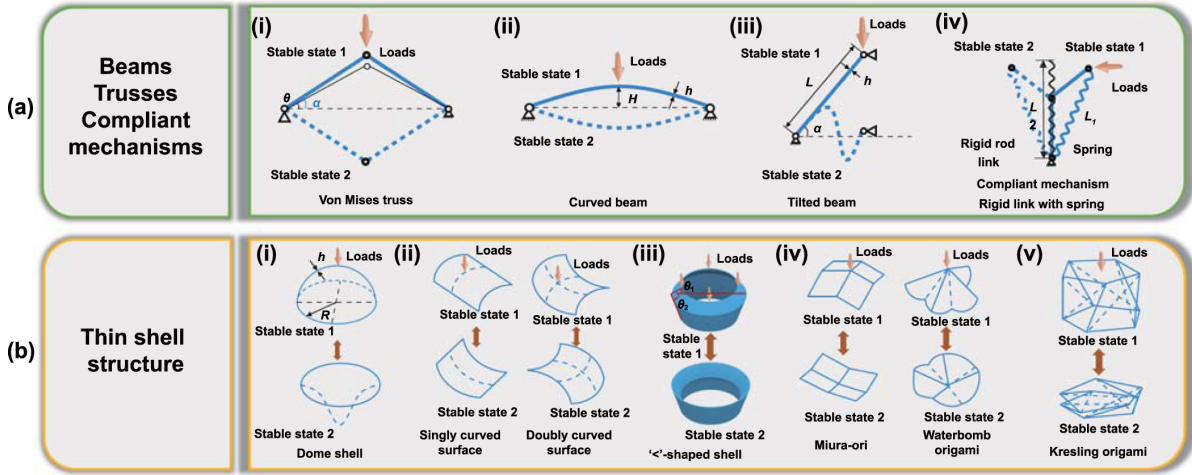


Figure 1.5: Common Bi-stable units. (a) Bi-stable beams, truss units and compliant mechanisms: (i) Von Mises truss; (ii) constrained curved beams; (iii) inclined straight beam; (iv) rigid connection compliant mechanism with spring. (b) Bi-stable thin shell unit: (i) dome shell; (ii) single curved surface and double curved surface [23]

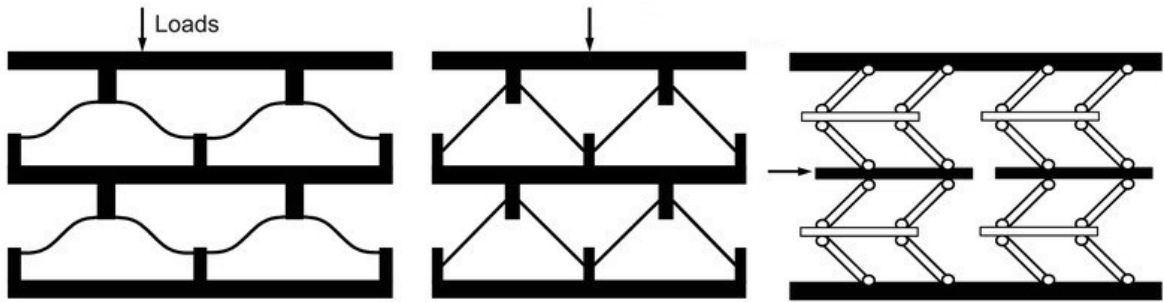


Figure 1.6: Conceptual structures of multi-stable mechanical metamaterials based on curved bi-stable beams, tilted beams and von Mises trusses, respectively [24].

The different structures and their geometric relations are described in detail by Xu et al. and Chi et al. [23, 24]. In fig. 1.6 some conceptual examples are shown of how these unit cells could be arranged to form multi-stable mechanical metamaterials with one degree of freedom (DOF).

The behaviour of bi-stable mechanisms is not only determined by their geometric design but also by the method of fabrication. Different manufacturing approaches can significantly influence the energy landscape of snap-through transitions, ultimately contributing to the metamaterial's functional response. There are three main ways to fabricate bi-stable curved beams, for which different analytical models have been developed to describe the snap-through behaviour. Hussein et al. collected these as follows [25]:

- Pre-compressed curved beams where the beam is fabricated rectilinear then it is compressed [26–28]
- Pre-stressed curved beams where during fabrication, the beam is buckled due to residual stress which is added by heating or oxidation [29].
- Pre-shaped curved beams where the beam is directly fabricated in the first buckling shape mode without residual stresses [30].

A schematic of the pre-compressed beam is represented fig. 1.7. The transverse deflection occurs when the compressive force P exceeds a critical value P_0 , the beam enters in the first buckling mode either upwards or downwards.

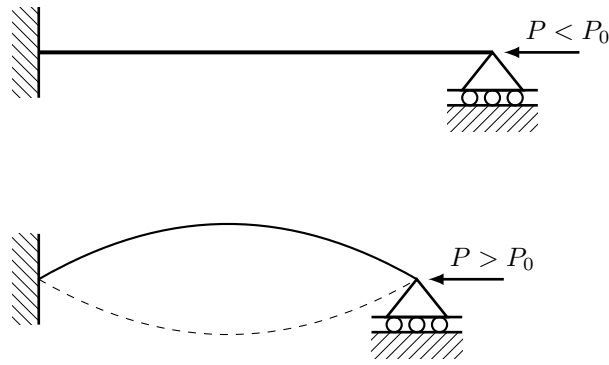


Figure 1.7: Straight beam axially loaded to buckle and form a bi-stable beam. Whereby $P < P_0$ and $P > P_0$ showing its two stable buckled configurations

The behaviour of a pre-compressed and pre-stressed curved beam is symmetrical between the two sides of buckling, in terms of the snapping force, beam shape and stresses evolution. This symmetric energy landscape is illustrated in (fig. 1.8) showing the two equal local minima. In contrast, when a beam is fabricated with intrinsic curvature, its initial geometry creates an energetically favourable state. This results in an asymmetric energy profile such that one stable state has a lower potential energy than the other (figure on the right in fig. 1.8).

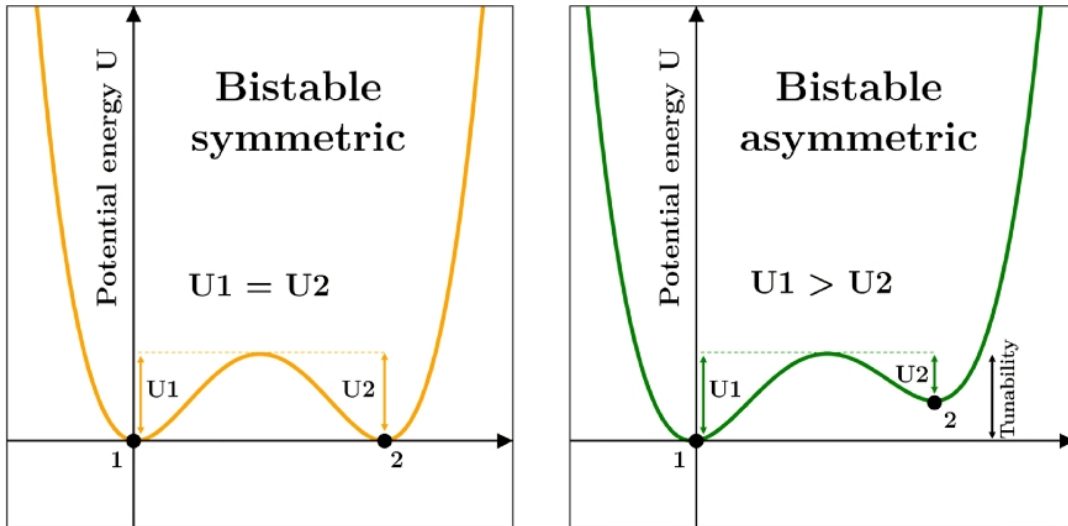


Figure 1.8: Symmetric energy landscape of (left) pre-compressed curved bi-stable beam and asymmetric energy landscape of (right) pre-shaped curved bi-stable beam. Note the tunability for the asymmetric energy landscape. [31]

The degree of asymmetry in the system can be controlled through the beam's geometry and boundary conditions. Structurally, the total energy in a curved beam consists of bending and compression energy. As the beam deflects downward, the bending energy increases, while the compression energy peaks at the midpoint and decreases beyond that point. If the reduction in compression energy exceeds the increase in bending energy, a negative force develops, indicating bi-stability [30]. Selecting a fabrication method is particularly crucial at the micro-scale. Pre-compressed beams are difficult to implement due to the challenges in applying and maintaining mechanical pre-compression at small scales. Pre-stressed beams, while allowing for monolithic fabrication (i.e. producing the structure as a single piece rather than assembling multiple components), present challenges in precisely controlling residual stress [25]. Alternatively, pre-shaped curved beams simplify fabrication by directly forming the structure in its buckled shape. Although this approach introduces asymmetry and requires specific geometric conditions for bi-stability, it offers greater feasibility for micro-fabrication. The conditions governing asymmetric snap-through behaviour in pre-shaped beams have been extensively analysed, making them a promising option for bi-stable unit cells in mechanical metamaterials [30].

1.3. Thesis research goal

The MECOMOS project (Mechanical Metamaterials for Compact Motion Systems) at TU Delft aims to advance research on precision motion components for high-tech applications [32]. By embedding motion functionality within metamaterials, it could potentially reduce the volume and mass of these systems significantly. Multi-stable mechanical metamaterials are particularly promising for this purpose because of their self-locking capabilities and ability to undergo controlled deformation in discrete steps. However, further research is required for the design and manufacturing of such structures to function as motion systems.

To investigate the potential of multi-stable mechanical metamaterials in line with the MECOMOS objectives, a literature review was conducted in an internal TU Delft report [33]. This review focused on the programmability of multi-stable mechanical metamaterials, specifically those designed to deform in a single degree of freedom (DOF) and constructed using beam-based bi-stable unit cells. In the context of deformable mechanical metamaterials, programmability refers to the ability to control their deformation behaviour either through design or on-demand adjustments. An example of an unprogrammed system with unpredictable behaviour is a multi-stable metamaterial composed of geometrically identical stacked layers. When subjected to a displacement load, the snapping sequence of the layers is determined by their relative stiffness, making it dependent on manufacturing variations rather than a pre-defined order. Consequently, the collapse sequence is random or difficult to predict. By programming the system, a specific deformation sequence can be designed. The TU Delft internal report classified programmability into two categories: passive and active.

- Passive programmability: Designing a pre-determined deformation sequence through micro-structural variance per layer
- Active programmability: Tuning or changing the deformation sequence and/or triggering state changes through external stimuli

A key distinction between passive and active programmability lies in their nature. Passive programmability is determined during the design phase and remains fixed after fabrication, whereas active programmability allows for re-programming of the system's arrangement. This capability for on-demand property modulation is also referred to as addressability. An overview of state-of-the-art examples from the literature is illustrated in fig. 1.9.

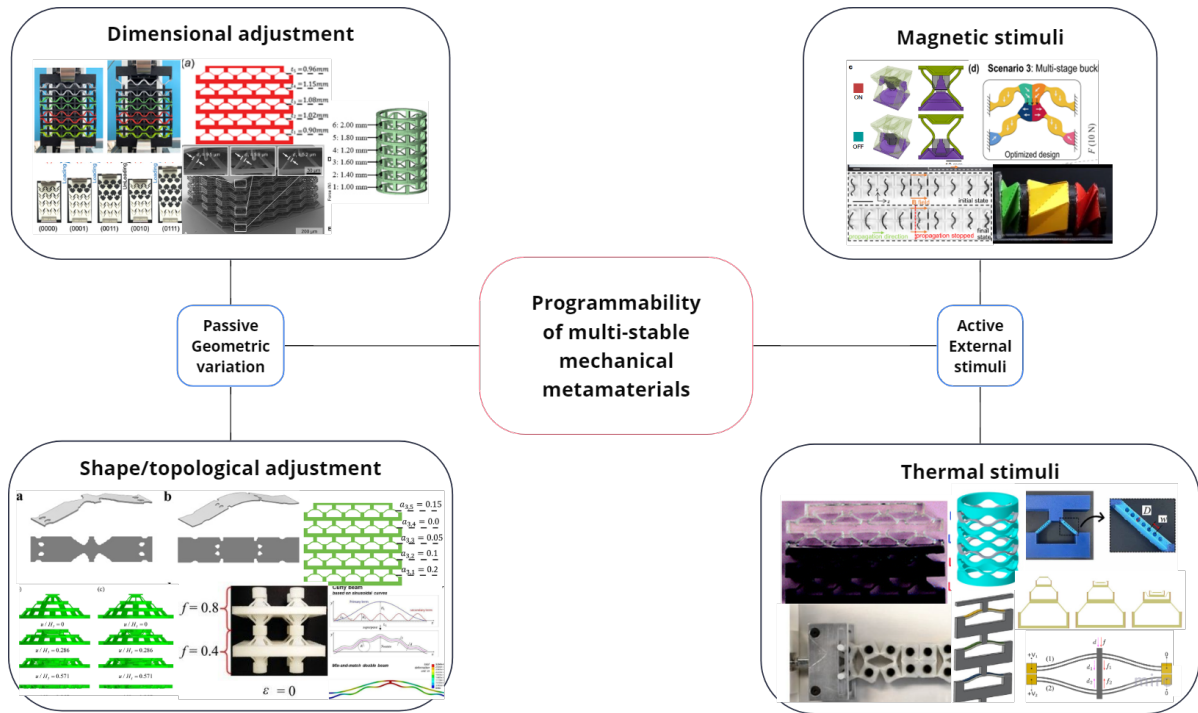


Figure 1.9: Visual categorization of different approaches to programming stiffness in multi-stable mechanical metamaterials

In passive programmability, most studies focus on geometric variations, which can involve dimensional adjustments or changes to shape and topology. In contrast, a common approach to achieve active programmability is by incorporating active materials and activating them through external stimuli. Under these stimuli, the metamaterials display varying properties, enabling them to meet application-specific requirements in real-time operational settings. Some studies also explore combining multiple stimuli for increased guidance. The literature review focused on the most prevalent stimuli (magnetic and thermal inputs) but there are examples of multi-stable mechanical metamaterials programmed using alternative stimuli, such as light or chemicals [34]. The more detailed table of passive and active programming approaches in recent literature can be found in appendix A. A number of research gaps related to the potential of multi-stable mechanical metamaterials as compact motion systems were highlighted in the conclusion of the review:

- Limited methods for **local** actuation to enable re-configurable positioning in mechanical metamaterials.
- Lack of exploration of mechanical metamaterials that achieve large motion range with high precision, such as designs with varying layer sizes.
- Lack of miniaturization of actively programmed multi-stable mechanical metamaterials.

The first research gap, local actuation, is critical because a motion system may require precise control over deformation states at specific locations. Current designs primarily rely on global actuation, limiting adaptability and fine positioning. The second gap concerns the balance between motion range and precision. Most existing designs do not incorporate variations in step sizes, which could allow for both coarse and fine positioning within the same system. The third gap relates to scalability. Almost all studies on actively programmed multi-stable mechanical metamaterials focus on macro-scale structures, whereas the intended application of compact motion systems requires functionality at micro-scale. Investigating how actively programmable multi-stable mechanical metamaterials can be effectively scaled down while preserving their functional properties remains relatively unexplored.

This thesis addresses the research gap of local actuation in multi-stable mechanical metamaterials. Specifically, the goal is to **design a multi-stable mechanical metamaterial with local one-directional programmability activated through external stimuli**. The approach targeted two main functional requirements, which are listed below:

- The design must allow for one-directional programmability through external stimuli.
- The design must be able to program layers individually through local actuation.

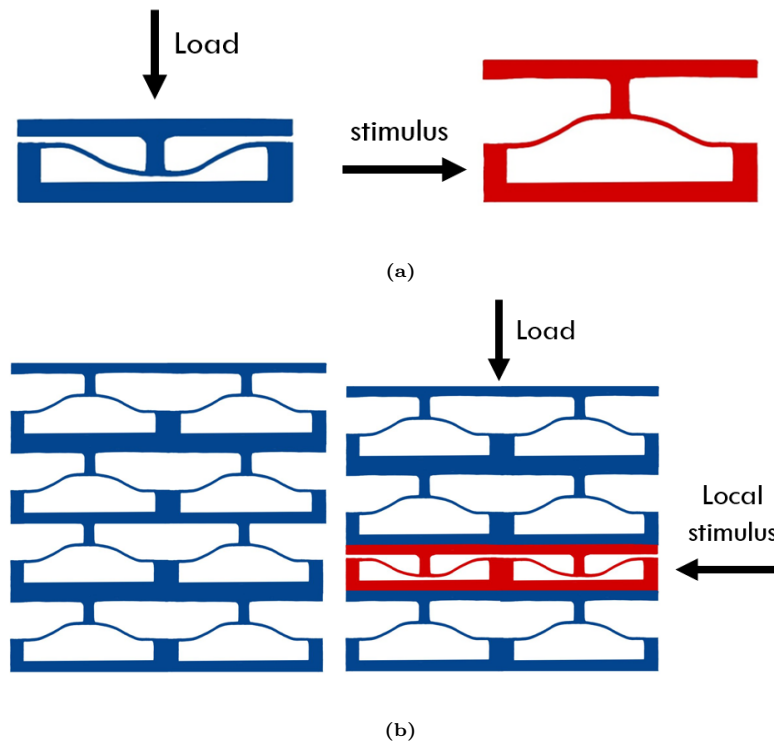


Figure 1.10: Visual representation of the desired programmability through the chosen functional requirements. (a) After mechanical loading, system unloads through external stimulus, (b) Use of combined mechanical load with local stimulus to adapt deformation sequence

One-directional programmability refers to the ability to trigger a unit cell or row to transition from one stable state to another without necessarily enabling reverse switching (bi-directional programmability). In this case, the structure can be mechanically deformed and subsequently activated to snap back using an external stimulus, as illustrated in fig. 1.10a. The motivation for this functional requirement lies in its potential to enable a reprogrammable multi-stable mechanical metamaterial, allowing the motion system to reset its position as needed. This capability enhances adaptability compared to a system that is only passively programmed. The second requirement describes the level of programmability that the design should be able to achieve. Currently, most state-of-the-art solutions program multi-stable mechanical metamaterials globally, adjusting the entire system. Through local actuation of individual layers, one could have more addressable control. Furthermore, one could use local actuation for an adjustable deformation sequence (see fig. 1.10b) by combining a mechanical load with locally applied stimuli to specific layers. A higher form of programmability would be at the unit cell level, which could, for example, be used to introduce tilted stable positions [22]. However, for a system which functions as a one-degree-of-freedom stepper, tuning layers will provide sufficient addressability.

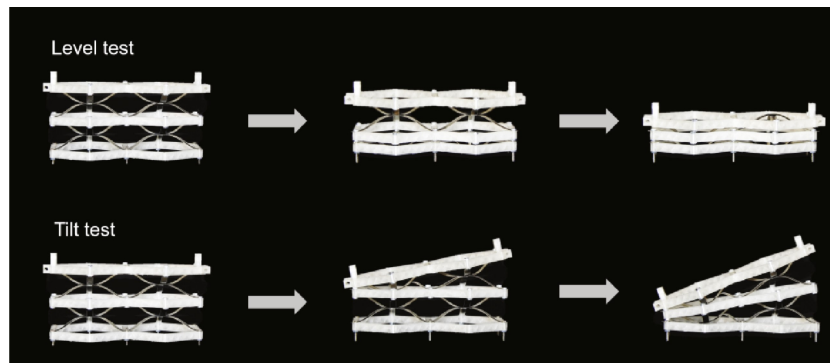


Figure 1.11: Tilted positions of multi-stable mechanism by Zhang et al. [22]

This thesis begins with an exploration of concepts that aim to achieve local one-directional programming in chapter 2. These concepts were primarily inspired by existing literature, providing a foundation for identifying strategies that could be further developed. Following a broad evaluation of the expected performance and feasibility of the proposed concepts, thermal stimuli emerged as the most promising and suitable for the intended functionality. A more detailed review of existing thermally activated solutions was conducted, which ultimately led to the selection of thermal softening of boundary conditions as the chosen programming approach. The approach and design are detailed in chapter 3, followed by the analytical and finite element model in chapter 4. In an attempt to verify the approach, physical samples were manufactured for an experimental setup, described in chapter 5. Throughout the experimentation process, several challenges were encountered, offering valuable insight into the working principle of the design and its limitations. These results are discussed in chapter 6. Finally, a conclusion of the key findings and recommendations for future work are presented chapter 7.

2

Exploration of local one-directional programmability

In this section, various concepts are proposed to achieve local one-directional programmability of unit cells in multi-stable mechanical metamaterials. The primary focus is on enabling one-directional transitions at the unit cell level, which could later be extended to a layer. First, the motivation behind achieving one-directional programmability in these systems is briefly explained. This is followed by the construction of a framework for stimuli-responsive actuation for desired kinematics, to inspire potential approaches in section 2.2. The subsequent section provides a structured overview of some of these concepts in section 2.3. Finally, the stimuli are holistically evaluated, aimed at current and future feasibility. The outcome of this evaluation provides the programming approach chosen for the thesis project, which will be detailed in chapter 3.

2.1. One-directional programmability

To illustrate the motivation behind achieving one-directional programmability in multi-stable mechanical metamaterials, consider a passively programmed system with two layers that can be mechanically loaded and unloaded. A system with n layers has 2^n stable configurations; therefore, this system has four unique configurations: $(0,0)$, $(1,0)$, $(1,1)$, and $(0,1)$, where 0 represents an open layer and 1 represents a closed layer. The achievable deformation sequences for this system are presented in fig. 2.1a.

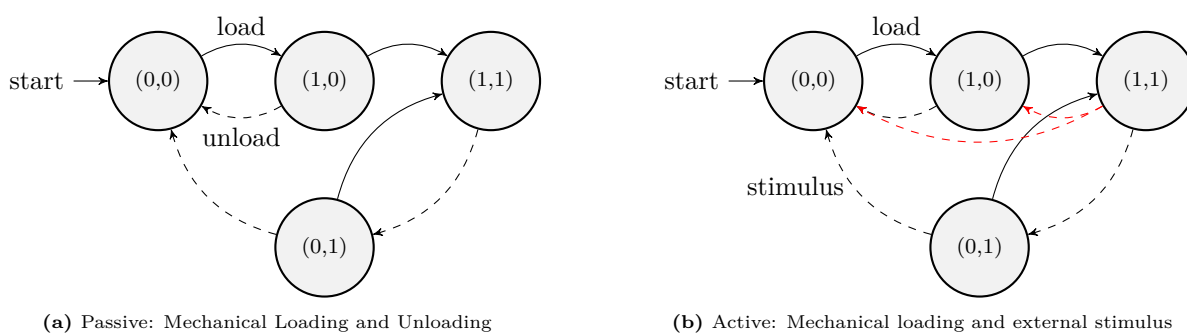


Figure 2.1: State Transition Diagrams for Different Actuation Methods

Starting from the fully open position $(0,0)$, applying one global mechanical load (black arrow) causes the first layer to snap, transitioning the system to $(1,0)$, as this layer has the lowest energy threshold. If the system is then unloaded (dashed arrow), it returns to its initial $(0,0)$ position. If the system is loaded twice, it reaches the fully closed state $(1,1)$. However, when unloading from $(1,1)$, the system does not revert to $(1,0)$, but instead transitions to $(0,1)$ because, during unloading, the first layer again has a lower energy threshold. This reveals a key limitation of passive programmability for motion

systems: to transition from (1,1) to (1,0), the system must be fully unloaded back to (0,0) and then reloaded, rather than directly transitioning. In contrast, a system with one-directional programmability via an external stimulus introduces additional transition paths, as illustrated in fig. 2.1b. In this system, the black arrows again represent global mechanical loading, while the dashed arrows indicate stimulus-induced transitions. Compared to the passive system, two new paths (highlighted in red) are introduced, allowing direct transitions between configurations without full unloading. Specifically, a localised stimulus can be applied to the second layer to reset it to its initial state, allowing the system to override the predetermined deformation sequence imposed by its geometry. As the number of layers increases, the available transition paths in the actively controlled system grow exponentially, far surpassing those of the passive system (see appendix C for a more detailed explanation). This enhanced tunability highlights the advantages of local and one-directional programmability in multi-stable mechanical metamaterials, thereby demonstrating the motivation behind this research.

2.2. Framework stimuli responsive actuation

Decroly et al. introduced a framework for programmable stimuli-responsive actuators in soft robotics, providing a valuable categorization of potential design approaches for this exploration [35]. The framework comprises four main sections that describe the programming of stimuli-responsive mechanisms for specific deformations: **stimulus**, **transducer**, **extrinsic asymmetry**, and **kinematics**. The key take-away is that in order to obtain guided kinematics, there must be at least some form anisotropy/directionality in either the stimulus or the transducer. Otherwise, the directionality must be integrated through extrinsic asymmetry. Each separate section is detailed as follows:

Stimulus

The stimulus is the source of energy activating the mechanism. Stimuli are categorized as either **isotropic** or **anisotropic**:

- **Isotropic stimuli:** These lack intrinsic directionality, examples include pressure, light, thermal, or chemical stimuli (e.g. pH or solvents).
- **Anisotropic stimuli:** These inherently have directionality, examples include electric or magnetic fields.

Isotropic stimuli can gain directionality when applied locally, allowing them to mimic the effects of anisotropic stimuli.

Transducer

The transducer transforms the energy from the stimulus into mechanical deformation. In addition to deformation, transducers may also produce other effects, such as stiffness variation or converting stimulus energy into another form (e.g. light to heat). Transducers can take the form of stimuli-responsive materials (e.g. shape memory polymers) or structures (e.g. dielectric elastomers). Transducers are further categorized as **isotropic** or **anisotropic**:

- **Isotropic transducers:** These produce uniform mechanical deformation. To achieve specific directional movement, they require **extrinsic asymmetry**, which provides guidance for a particular motion.
- **Anisotropic transducers:** These exhibit intrinsic asymmetry and can directly generate guided deformation. (e.g. magnetized components, dielectric elastomer)

Extrinsic asymmetry

Extrinsic asymmetry guides the deformation into the desired kinematics through mechanical constraints. Asymmetry can, for example, be integrated through **material customisation**, **multi-material designs**, and **geometry modification**. As mentioned extrinsic asymmetry is necessary to guide isotropic transducers but it can also be applied to anisotropic transducers for increased guidance. Decroly et al. classifies passive asymmetry as mechanical constraints which do not rely on simulation and active asymmetry which is controllable and triggered by an additional stimulus. However, in their framework, there

is only one example of this which is stiffness variation. In this study only passive extrinsic asymmetry will be considered.

Kinematics

The author sorts the four basic kinematics as: shear, twisting, bending and elongation-compression (see fig. 2.2). When considering a beam with a fixed extremity, it corresponds to the six degrees of freedom of the other extremity.

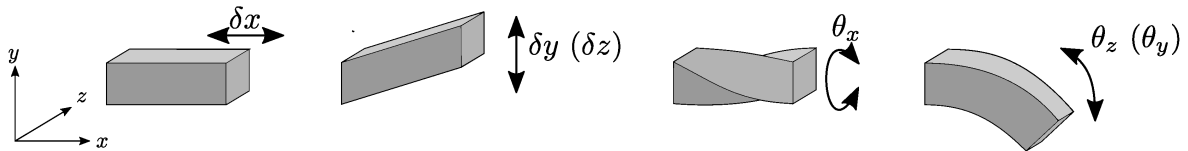


Figure 2.2: Four basic actuator kinematics corresponding to the six degrees of freedom of a surface when considering the other side fixed: three translations (elongation/compression δ_x and shear δ_y and δ_z) and three rotations (twisting θ_x and bending θ_y and θ_z). [35]

The roadmap illustrated in fig. 2.3 shows an overview of the various programming methods discussed in the paper by Decroly et al. It serves as inspiration for how the concepts for this study can be categorised.

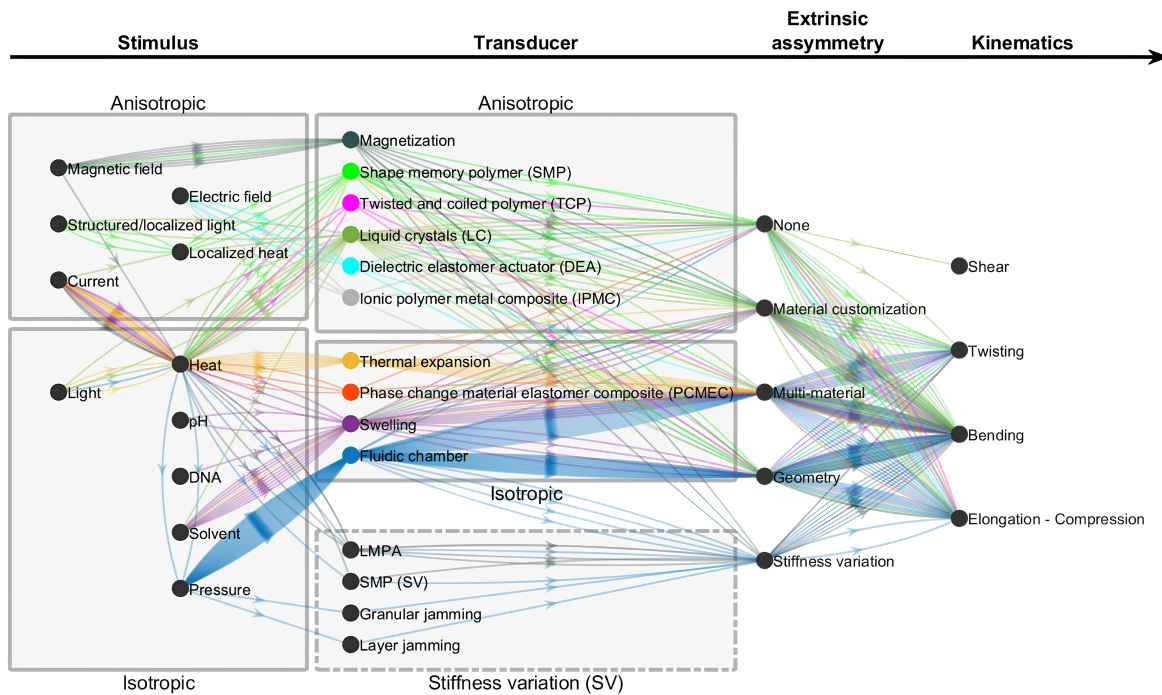


Figure 2.3: Roadmap of actuator design from stimulus to actuation. Each actuator reviewed in the paper by Decroly et al. is represented by a set of arrows. The arrow colours indicate the main transducer principle used to generate a deformation. [35]

2.3. Concept overview

A framework tailored to the focus of this study is constructed, based on the one presented in fig. 2.3. Modifications were made to focus specifically on programming curved bi-stable beams rather than the broader category of soft robotics. Certain transducers were excluded due to their incompatibility with bi-stable beams, while trans-cis isomerisation (light based) and thermal softening (an effect in amorphous polymers) were added due to their potential in achieving the desired one-directional programmability.

This refined framework is presented in fig. 2.4. To narrow down the scope of this exploration in this study, mainly solutions for bending and elongation were used as desired kinematics in the framework of this study. Another addition is the location of where the kinematics is activated by the stimuli and transducer. This is specified as either being at the boundaries or on the bi-stable beam. The revised framework includes potential paths to achieve the desired kinematics, of which many have been incorporated in a table of concepts presented in table 2.1 and table 2.2. To enhance feasibility, most concepts draw inspiration from existing literature on programming bi-stable mechanisms. However, some paths in the framework represent potential solutions that have not been (fully) explored in prior research. In some cases, the entire pathway from stimulus to kinematics is novel, for example, using light actuation to trigger trans-cis isomerisation to bend boundary conditions of a bi-stable beam. In other cases, only a specific aspect remains unexplored, such as the use of localised heat for thermal softening. The novel paths are indicated by dotted lines in the framework.

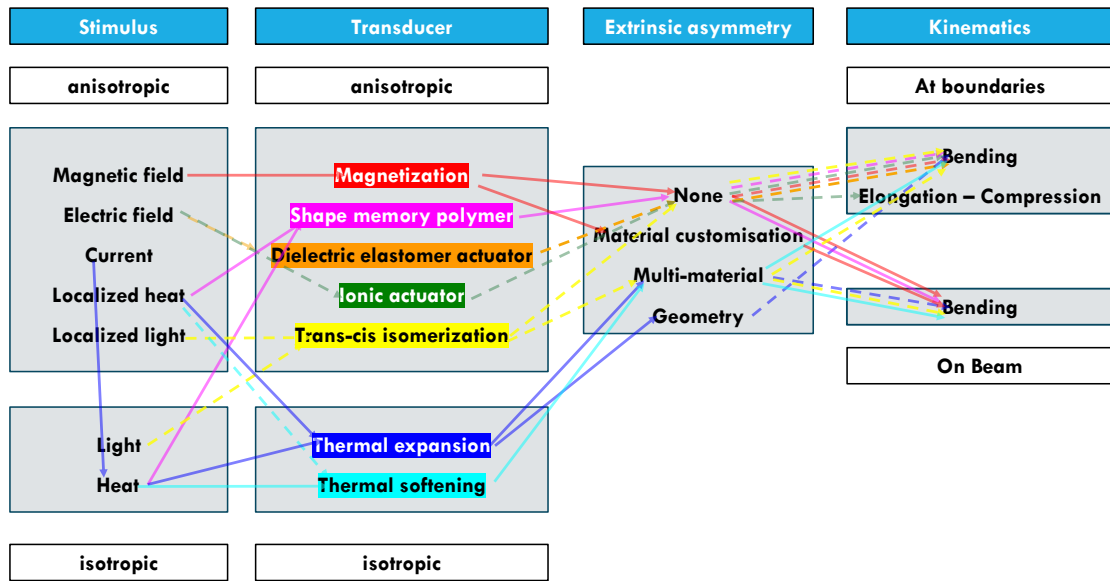
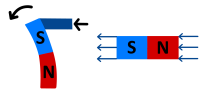
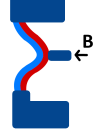
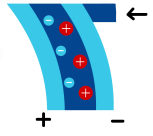
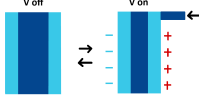


Figure 2.4: Framework for stimuli-responsive actuation for one-directional programmability of bi-stable beams

The tables 2.1 and 2.2, show some of the potential approaches for one-directional programmability of bi-stable beams. The tables are divided between their location of activated kinematics, either at the boundaries or on the beam. For the concept images of the activation at the boundaries, just the boundary is illustrated. The literature used as inspiration is noted for each concept alongside the field of application intended by the authors.

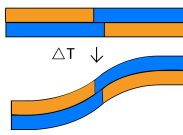
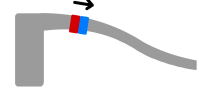
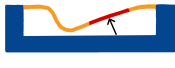
Table 2.1: Activation at Boundaries

Concept Image	Stimulus	Transducer	How It Works	Application in Literature
	(Localized) heat	Thermal softening or SMP	Heat reduces stiffness allowing bending of side supports	Adaptive structures, self-deployable structures [36, 37]*
	(Localized) heat	Thermal softening or SMP	Heat reduces stiffness of allowing bending bottom plate	Adaptive structures, deployable metamaterials [38]*

	(Localized) heat	Thermal expansion, geometry	Difference in thermal expansion of arms causes supports to bend	Aerospace, MEMS, microfluidics [39]
	Magnetic field	Magnetization	External magnetic field induce bending of boundaries	Microfluidics, droplet transport [40]
	Magnetic field	Magnetization	External magnetic field induce bending of boundaries	Soft reconfigurable electronics, magnetic switching [41]
	Electric	Ionic actuation	Electric fields cause ion migration inducing bending of boundaries	Biomedical devices, soft robotics [42]
	Electric	Dielectric elastomers	Applied voltage induces deformation of boundaries	MEMS, soft robotics, biomedical devices [42]

* Indicates reference paper also aimed at programming bi-stable unit cells.

Table 2.2: Activation on the Beam

Concept Image	Stimulus	Transducer	How It Works	Application in Literature
	(Localized) Heat	Thermal softening, multi-material	Heat lowers stiffness of activated beam material, inducing snap-back	Adaptive structures, deployable metamaterials [38]*
	(Localized) Heat	Thermal expansion, multi-material	Distinct thermal expansion causes beam to bend	Soft micro actuators [43]
	Magnetic field	Embedded hard magnets	External magnetic field exert torque causing bending of beam	Aerospace, biomedical, flexible electronic devices [44]*
	Magnetic field	Magnetization, material customization	External magnetic field induce snap through of beam	Robotics, MEMS, programmable devices [45]*
	(Localized) Light	Trans-cis isomerization	Light triggers molecular conformation changes leading to bending of beam	Micro robotic structures [46]

* Indicates reference paper also aimed at programming bi-stable unit cells.

2.4. Stimulus evaluation

The concepts presented in tables 2.1 and 2.2 are not exhaustive but represent potential approaches for achieving one-directional programmability. Numerous other methods exist for programming bi-stable unit cells to achieve controlled deformation, as reviewed by Zhang et al. [47]. To refine the selection,

the stimuli are compared on the basis of their advantages and limitations. Given that this research is in an exploratory phase, the primary objective is to demonstrate feasibility rather than optimise factors such as speed, precision, or efficiency. As a result, simplicity in both the stimulus and its applicable transducer is a key criterion in determining the most suitable solution direction. Additionally, the challenges associated with integrating the selected approach into three-dimensional structures must be considered, as this will be crucial for future applications requiring multi-degree-of-freedom compact motion systems. Since the goal is to achieve local programmability, isotropic/globally applied stimuli are excluded from the evaluation.

Evaluation of Stimuli			
Stimulus	General properties	Applicable Transducers	3D Transferability Risks
Magnetic Field	Wireless control, fast response rate but requires bulky actuation setup	Magnetization-based transducers	Magnetic fields may cause interference between adjacent units, requiring precise alignment or shielding.
Electric Field	Rapid response, suitable for micro-scale applications, but requires wired integration.	Dielectric elastomer actuators, Ionic actuators	Wiring complexity can limit scalability; miniaturization may be needed for compact systems.
Localized Heat	Simple implementation, but low efficiency and precision.	Shape memory polymers, Thermal expansion, Thermal softening	Heat dissipation may affect neighbouring structures; thermal gradients need careful management.
Localized Light	High spatial precision, but requires complex optical setup.	Trans-cis isomerisation, Photothermal actuators	Optical pathways may become difficult to reach inside 3D-tessellated structures

Table 2.3: Evaluation of Stimuli Based on Ease of Actuation, Applicable Transducers, and 3D Transferability Risks

Although magnetic and electric field-based actuation offers fast response times, they introduce additional complexity due to tuning of an external field. Localised light also offers spatial precision, but may become more challenging to implement in a 3D structure. In contrast, localised heating, while less energy-efficient and precise, provides the simplest and most experimentally achievable approach. As a result, localised heating was selected as the preferred stimulus for this study. This choice is further supported by the availability of compatible transducers, such as shape memory polymers (SMPs), thermal expansion, and thermal softening, all of which have been explored in recent literature for programming mechanical metamaterials. However, compared to SMPs and thermal softening, thermal expansion remains relatively unexplored. Consequently, it was not considered further in this study. The following section will provide a detailed description of the two more common thermally programmed transducers, SMPs and thermal softening, based on recent studies, to justify the selection of the most suitable approach for this research.

2.5. Thermally programmed transducers

Building on the evaluation in Section 2.4, this section examines the Shape Memory Materials (SMMs) and thermal softening, to achieve programmable deformation in bi-stable structures. SMM are materials which possess a unique capability to be programmed into temporary configurations and subsequently return to a predefined initial configuration upon exposure to various stimuli such as heat, light, water/humidity, and magnetic fields [48]. They are an attractive mode of actuation for this study due to their reversible and “directional” nature. An example where SMPs are used to program a deforming lattice structure via heat is presented in fig. 2.5a [48]. The authors focus on programming a specific transformation time or deploying sequence through geometric variance under a uniform stimulus (heat). In the context of this study’s framework, their design employs an anisotropic transducer in combination with extrinsic asymmetry (geometry) to increase the guidance of the deformation. A lattice structure with varying layers is presented in fig. 2.5b.

The programming method in this example consists of the following steps, represented graphically in fig. 2.5a. During the loading stage, a displacement load is applied to the top of the structure at 62°C until $t = 100$ s. In the cooling step, the temperature is reduced to 22°C over 15 s while the structure remains fixed, maintaining this temperature until $t = 200$ s. During the unloading step, the displacement constraint is released, resulting in a small recovery strain in the structure. The deformed configuration in this step is commonly referred to as the temporary configuration. Finally, during the heating process, the structure is heated up to a temperature of 62°C within 15 s, and this temperature is maintained until the structure fully recovers its original shape. An important distinction is that this programming method does not work if the unit cells are bi-stable. It fails to return to its original shape because the thermal recovery stress cannot overcome the strain energy barrier of these bi-stable structures. Therefore a limitation of using shape memory to program is that it does not have inherent self-locking capability and always needs to be re-programmed under stimulation to the temporary shape.

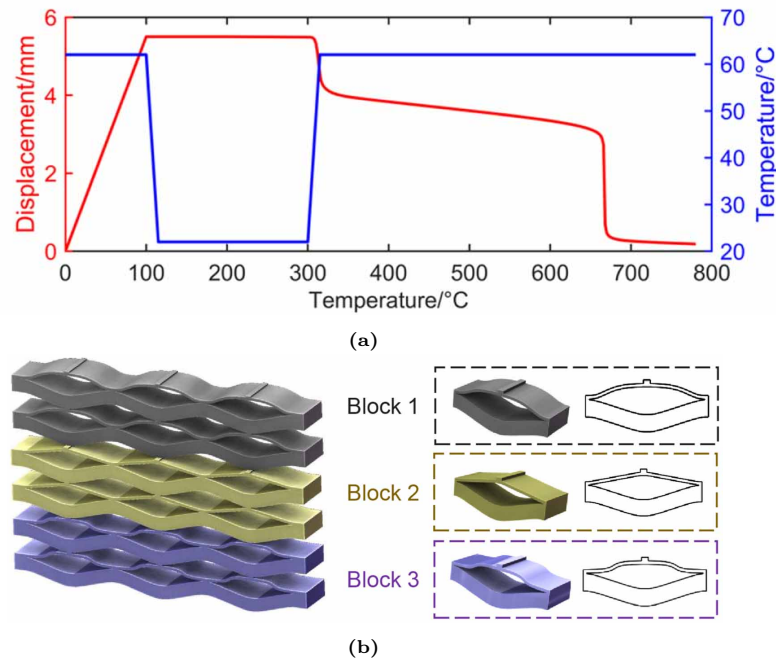


Figure 2.5: (a) FE simulation of the shape memory process of a classical V-beam structure: Displacement and temperature over time. (b) Three-dimensional model of an SMP lattice structure and its building blocks of varying geometry [48].

Due to this disadvantage, a suggested alternative to SMPs is using thermal softening to mimic the shape memory effect [36, 49]. With this approach, there is no programming step required to give the structure a temporary shape, as only the stiffness is tuned to transition a deformed bi-stable beam into its initial state. The working principle requires an asymmetric energy bias for the initial state. This is

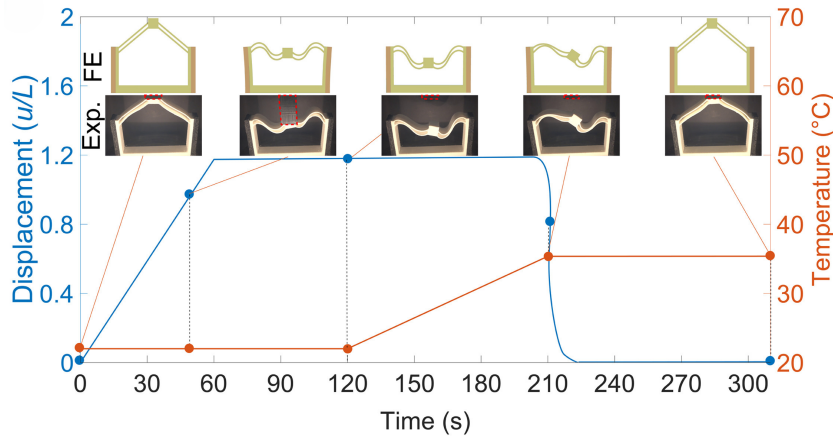


Figure 2.6: Displacement – time response and snapshots of FE and experimental analyses for a 1D unit cell [36]

an intrinsic property of curved bi-stable beams which are manufactured into their shape rather than a straight beam tensioned to buckle, as described in chapter 1. An example of this programming approach is displayed in fig. 2.6 from a paper by Niknam et al. [36]. The unit cell is deformed mechanically into its second stable state at room temperature. When the temperature is increased, the unit cell restores its original shape at a certain transition temperature.

This is a significantly more simple programming approach compared to SMPs and has been demonstrated in literature through various designs and materials [36, 38, 49–52]. However, unlike SMPs, thermal softening is an isotropic transducer, which means an extrinsic asymmetry is required to achieve a directed kinematic response. The most common technique in literature is the use of multi-material designs. A so called “active” material can be applied either directly to the beams or at their boundaries, while the base material of the beam is commonly constructed out of a “passive” material. The passivity comes from its relatively independent stiffness over the entire operating temperature range, whereas the active material will undergo drastic variation in stiffness. This measure of stiffness is more commonly described as its elastic or storage modulus (E'). The storage modulus is the measure of elasticity of material, or the ability of the material to store energy elastically. It is commonly measured with a dynamic mechanical analysis (DMA), which can also be used to measure the loss modulus (E''). This represents the viscous part or the amount of energy dissipated in the sample being tested. If the storage modulus is greater than the loss modulus, then the material can be regarded as mainly elastic. Conversely, if loss modulus is greater than storage modulus, then the material is predominantly viscous (it will dissipate more energy than it can store, like a flowing liquid) [53]. The ratio of the loss modulus to the storage modulus is defined as the damping factor or loss factor and denoted as $\tan \delta$. $\tan \delta$ indicates the relative degree of energy dissipation or damping of the material. The peak of the loss factor can be used as an indication of the T_g . These moduli and their relation to each other are illustrated in fig. 2.7.

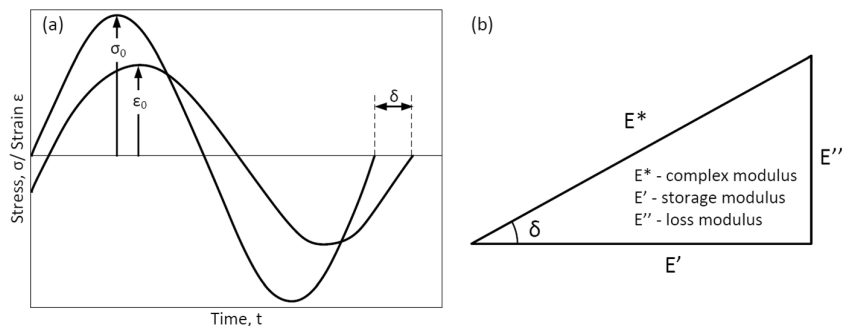


Figure 2.7: a. Applied strain and measured stress for materials with damping-like behaviour, where a phase angle appears between input and output. b. Relation between modulus components and the measured phase angle δ [54]

All polymers that are amorphous or contain amorphous regions (semi-crystalline polymers) exhibit a glass transition temperature T_g . Below the T_g , these materials behave as rigid, glassy solids, whereas above this temperature, they become significantly softer and more flexible, functioning either as elastomers or highly viscous liquids. In this transition region, mechanical properties undergo substantial changes, with the storage modulus potentially decreasing by over three orders of magnitude as the temperature increases. Due to these drastic property variations, T_g is considered a key characteristic defining the mechanical behaviour of polymers [55].

Programming a bi-stable beam to become mono-stable through thermal softening can be achieved via two possible combinations of storage moduli of the active and passive materials in the bi-stable design. The passive beam material can either have a T_g far below or far above the operating temperature. For the design with a beam T_g far above the operating temperature, there are two variations where either the beam is more or less stiff than the support. These three possibilities are illustrated in fig. 2.8. The storage moduli presented in these figures are arbitrary and merely indicate the potential options for applying this programming approach.

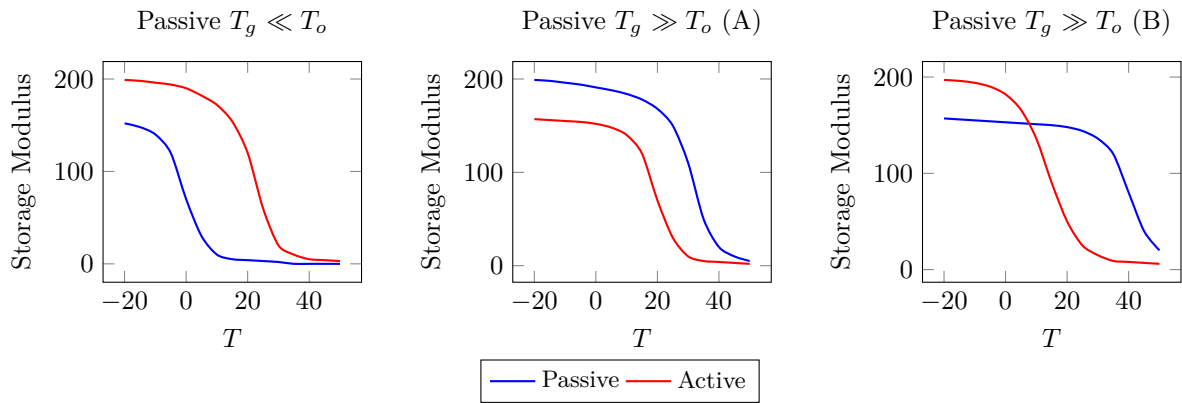


Figure 2.8: The three possible combinations of storage moduli of the active and passive material for thermal softening as a programming approach.

An example of a design using a beam with a T_g below the operating temperature, meaning the beam is in its rubbery-state, was presented in fig. 2.6. Niknam et al. uses a beam made out of Thermoplastic Polyurethane (TPU) and bi-material boundaries of TPU and Carbon-Fiber-Reinforced (CFR) Nylon. The CFR Nylon is the active material and acts as a stiff material which is placed at the boundaries. The storage modulus and loss factor ($\tan \delta$) of the two materials are presented in fig. 2.9.

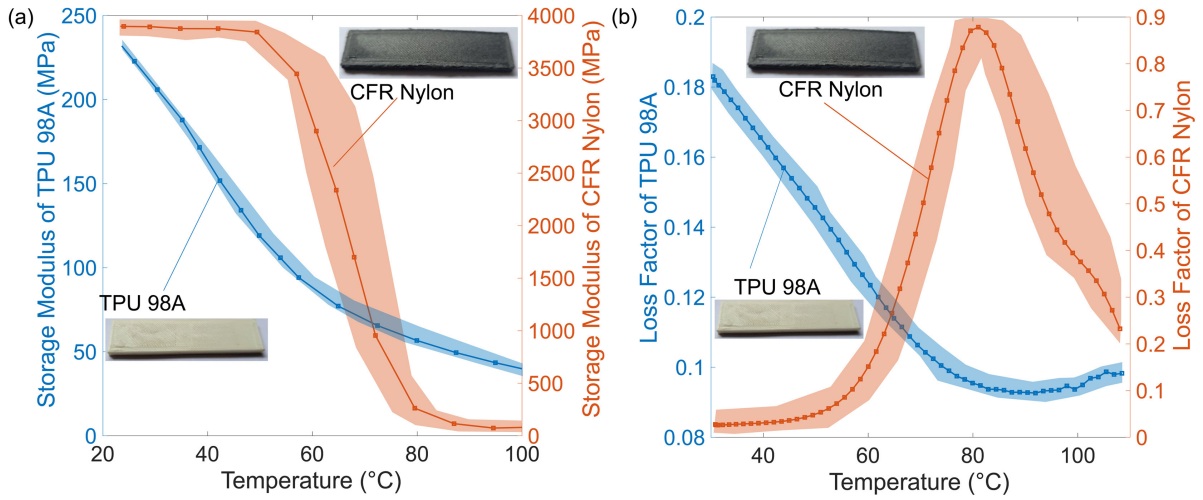


Figure 2.9: This figure presents the average results for storage moduli versus temperature of the materials used in the unit cell. The standard deviation is shown by highlighted areas.[36]

The softening effect can be observed in both materials, however, the trend is quite different. In the case of TPU, we observe a monotonic decrease of storage modulus, while for CFR-Nylon there is a sharp drop between 45°C and 80°C which represents its glass transition. This is further illustrated by the peak in Nylon’s loss factor. By increasing the relative width of the stiffer material in the supports of the unit cells, the equivalent stiffness of the wall increases. This directly affects the bi-stability of the beam and thereby the transition temperature, at which the system becomes mono-stable. To illustrate this effect, designs with varying wall thicknesses and strut angles are investigated through finite element analysis, displayed in fig. 2.10.

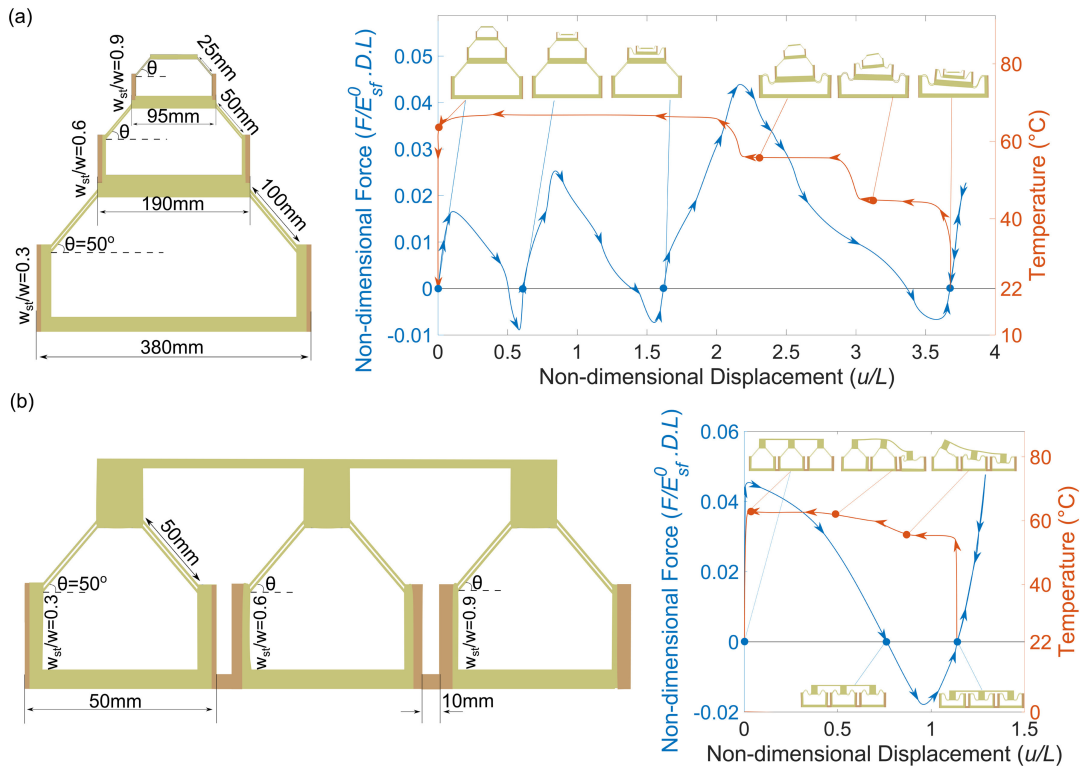


Figure 2.10: (a) Force-displacement and temperature-displacement diagrams for a hierarchically tessellated thermally bi-stable structure with $\theta = 50^{\circ}$ and $\frac{t}{L} = 0.028$. (b) Force-displacement and temperature-displacement diagrams for horizontal and heterogeneous tessellation of thermally bi-stable structures with $\theta = 50^{\circ}$ and $\frac{t}{L} = 0.028$ and alternative $\frac{w_{st}}{w}$ [36]

3

Design

In chapter 2, concepts were proposed to tune the energy landscape of asymmetrically bi-stable beams to transition to mono-stability via external stimuli. The selected solution enables this effect using localized heat to tune the stiffness of the boundary conditions of the beam. In order to reach the desired kinematics of the beam an extrinsic asymmetry is implemented by using multiple materials in the design. In this section the programming approach is fully described and a novel design is proposed.

3.1. Thermal softening as a programming approach

As described in section 2.5, thermal softening can be implemented in different ways, leading to varying degrees of programmability. The possible outcomes based on different design choices are summarised in fig. 3.1. The fundamental requirement for this approach is that the beam must exhibit asymmetric bi-stability. This can be achieved by fabricating the beam with an intrinsic curvature. A key design choice is whether the structure is composed of a single material (mono-material) or multiple materials (multi-material).

- **Mono-material:** Mono-material structures cannot achieve a transition from bi-stability to mono-stability through temperature variation. This limitation arises because the approach relies on a change in relative stiffness between the boundaries and the beam. If both components experience an identical change in storage modulus with temperature, there will be no change in relative stiffness. This means the critical force magnitudes may vary, but the overall shape of the force-displacement curve remains unchanged. However, mono-material structures can still be programmed to control deformation sequences. By applying localised heat to specific layers, their stiffness can be selectively tuned so that under mechanical loading, those layers snap first. This type of programmability has been demonstrated in previous studies [50].
- **Multi-material:** Multi-material structures introduce a passive beam material and an active boundary material. This enables a more versatile programming approach. The beam material can either be:

- in its rubbery state ($T_g \ll T_o$), or
- in its glassy state ($T_g \gg T_o$).

The active material must always have a T_g above the neutral operating temperature (T_o) but within the overall operating range.

After this selection, the geometry must be tuned so that at neutral T_o , the boundaries function as near-fixed constraints but become sufficiently soft at the transition temperature T_t .

- **In theory:** If the glass transition temperatures of the materials are sufficiently spread out, a transition temperature T_t will always exist.

- **In practice:** The desired T_t may not align with achievable dimensions due to fabrication limitations. If the ideal T_t cannot be achieved, the system can still be programmed for specific deformation sequences. The addition of a second material inherently increases the programmability compared to a mono-material structure and can be used to modify the force-displacement curve.

In an optimal scenario, the geometry and material properties can be precisely tuned so that a transition temperature T_t exists at the desired temperature, and the system can be manufactured with the required dimensions. This would allow for full programmability of bi-stability to mono-stability through thermal stiffness modulation of the boundary conditions.

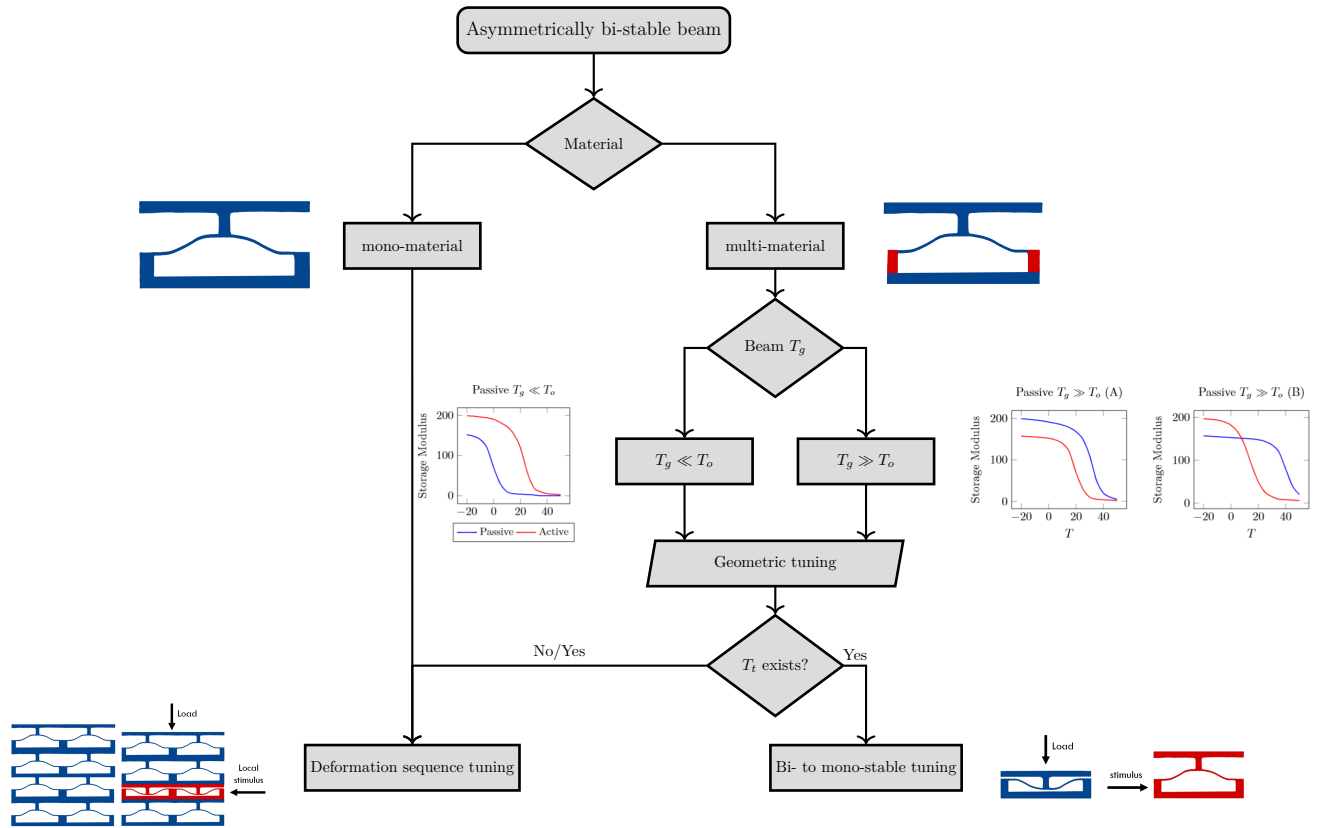


Figure 3.1: Flowchart of thermal softening as a programming approach for asymmetrically bi-stable beams.

3.2. Detailed design

The two most relevant studies from the literature that utilise thermal softening as a programming method for bi- to mono-stable tuning were discussed in section 2.5. These works highlight significant variations in design approaches, particularly in beam shape, material selection, and support geometry and composition. For instance, Niknam et al. used a truss-shaped beam whereas Zhang et al. made use of curved beams. While both designs relied on activating the material in the support boundaries, their designs differ in support composition. Niknam et al. used bi-material supports with a relatively stiff active material and a flexible passive material. In contrast, Zhang et al. employed a relatively flexible active material in single material supports. The relative stiffness of the active and passive materials strongly influences the geometry of the support system. For the mechanism to maintain bi-stable behaviour at T_o , the boundary conditions must be sufficiently stiff to reach near-fixed conditions. If the active material has a relatively low elastic modulus at T_o , the width (w_s) relative to the height (h_s) of the supports must be increased to compensate. The geometry of the supports will in turn influence the mechanics during deformation, whereby bending stiffness dominates when $\frac{h_s}{w_s} > 0.8$, and shear stiffness governs at lower ratios [56]. This demonstrates the potential variations of this programming approach.

For this project, the curved beam shape introduced by Qiu et al. [30] has been chosen due to the extensive analytical models available for its snap-through behaviour. The remaining design choices can be systematically organized in a table to identify novel directions for further exploration, see table 3.1. Note that both Zhang et al. and Niknam et al. make use of a multi-material design but that the table distinguishes whether the support is single or multi-material.

Beam T_g	Support Stiffness	Support Composition	Reference
$T_g \ll T_o$	Bending	Multi-material	Niknam et al. (2022) [36]
$T_g \gg T_o$	Bending	Multi-material	This study
$T_g \ll T_o$	Bending	Single-material	-
$T_g \gg T_o$	Bending	Single-material	-
$T_g \ll T_o$	Shear	Multi-material	-
$T_g \gg T_o$	Shear	Multi-material	-
$T_g \ll T_o$	Shear	Single-material	-
$T_g \gg T_o$	Shear	Single-material	Zhang et al. (2021) [49]

Table 3.1: Overview of design choices, tested configurations, and novel possibilities.

The decision to investigate a design with a rubbery or glassy beam is closely related to the future applications of the MECOMOS project. This project explores the potential of PolyEther Ether Ketone (PEEK) as a base material for mechanical metamaterials in compact motion systems. PEEK is a high-performance polymer known for its superior mechanical properties and chemical resistance, making it widely used in the automotive, aerospace, industrial equipment, and biomedical industries [57]. With a relatively high glass transition temperature of approximately 145 to 150°C, PEEK beams are expected to remain in their glassy state under most operating conditions. In fig. 3.2, one can see the DMA results of PEEK and another high-performance polymer, Polyetherimide (PEI), along with a composite whereby the material undergoes both glass transitions.

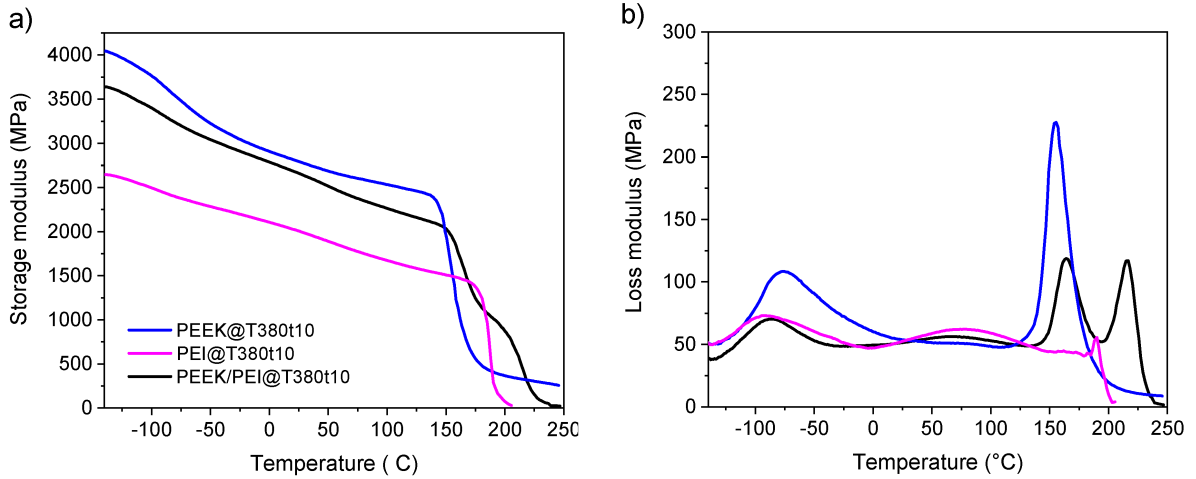


Figure 3.2: DMA plots of multilayer PEEK/PEI, PEEK and PEI (a) storage modulus and (b) loss modulus (at 5Hz) [58]

As a result, this study focuses on programming unit cells with glassy beams. A choice must also be made regarding the geometry and composition of the supports. Using bending beams offers the advantage of tuning support stiffness by adjusting their length. Additionally, bending beams can be easily connected to a straight bottom plate, whereas shearing supports may introduce challenges due to the beam requiring enough vertical space for its second stable position. Specifically, if the support height is shorter than the beam's apex height, the bottom plate may require modifications to accommodate snap-through behaviour. Therefore, while shearing supports present an interesting area for further study, bending

beams offer a simpler and more practical implementation. Furthermore, opting for multi-material supports expands the range of usable materials. Softer materials can be reinforced with the passive beam material, maintaining a bending-dominant geometry. A potential drawback of using multi-material supports is the added complexity in the fabrication process. However, since the overall design already integrates multiple materials between the beam and support for functional purposes, this approach could be used to create smoother transition between the beam and support, improving both adhesion and structural cohesion.

The parametric model of the design is illustrated in fig. 3.3a. The row design is guided by the decision to employ bending supports (see fig. 3.3b). Unlike the work by Zhang et al., this design incorporates a gap for the bending of the supports. Furthermore, the heat stimulus will be localized to enhance programmability, offering a notable improvement over the current state of the art. The final selection results in a novel design for the thermal programming of multi-stable mechanical metamaterials.

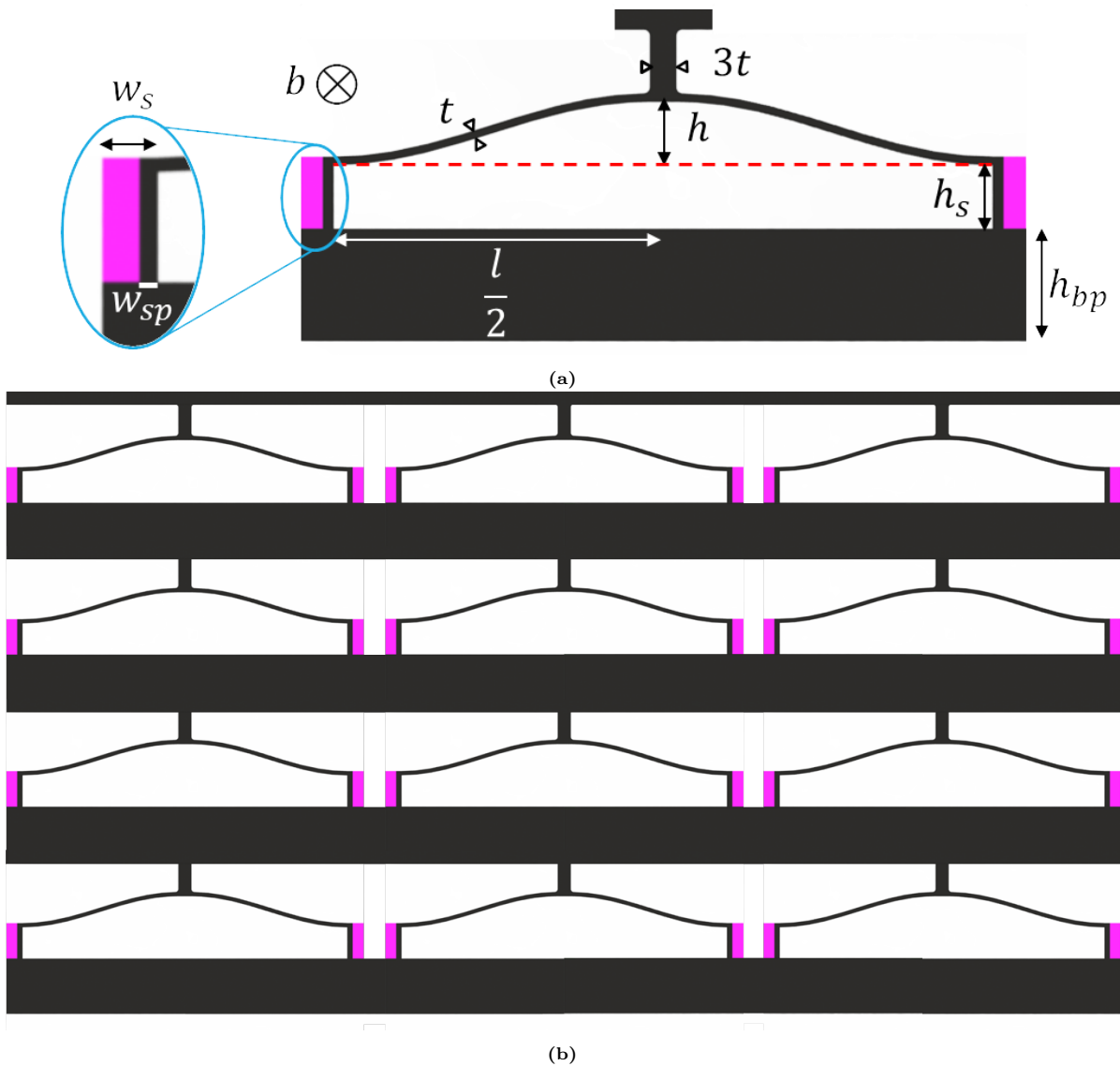


Figure 3.3: (a) Dimensions of proposed design for unit cell and (b) indication of a 4x3 layered structure for multi-stable mechanical metamaterial

4

Modelling

This chapter develops an analytical model to describe the snap-through behaviour of a bi-stable unit cell with temperature-dependent boundary stiffness. By extending existing models for curved bi-stable beams, it incorporates multi-material boundary conditions which are temperature dependent. This gives insight on the stability thresholds and transition behaviour of the proposed design. Subsequently, finite element analysis is used to verify the analytical predictions and explore more complex geometries beyond analytical constraints in section 4.2.

4.1. Analytical model

The analytical model for the design proposed in chapter 3 is built upon existing literature. The foundation was established by Qiu et al. with an analytical model describing a fixed-fixed curved bi-stable beam [30]. This model uses superposition of different buckling modes, whereby the first three modes play a significant role in determining the beam's bi-stability. Building on this work, variations are introduced where the fixed-fixed boundary condition is replaced by boundaries with variable stiffness [49, 59]. The last adjustment implements boundaries made up of two distinct materials with varying geometry and elastic modulus. The final analytical model is able to describe the snap-through behaviour a bi-stable unit cell supported by multi-material boundary conditions with temperature dependent stiffness.

4.1.1. Fixed-Fixed boundary conditions

Qiu et al. introduced an analytical model for a fixed-fixed (or clamped-clamped) pre-curved beam which is based on the principle of mode superposition [30]. It is inspired from a bi-stable buckled straight-beam, where a straight beam is axially compressed to buckle to two stable positions. First the straight beam is described, which will be the mathematical foundation for the buckling analysis of the pre-curved beam. Based on small deformation hypothesis from Timoshenko et al. [60], the buckling equations describes a straight beam subjected to axial load p :

$$EI \frac{d^4 w}{dx^4} + p \frac{d^2 w}{dx^2} = 0 \quad (4.1)$$

where w is the lateral beam displacement, E is the Elastic modulus of the beam, and I is the moment of inertia of the beam. For clamped-clamped conditions, the following boundary conditions are in place

$$w(0) = w(l) = 0, \left(\frac{dw}{dx} \right)_{x=0} = \left(\frac{dw}{dx} \right)_{x=l} = 0 \quad (4.2)$$

The axial force can be normalized by

$$N^2 = \frac{pl^2}{EI} \quad (4.3)$$

In order to have nonzero solutions, N must satisfy

$$\sin\left(\frac{N}{2}\right) \left[\tan\left(\frac{N}{2}\right) - \frac{N}{2} \right] = 0 \quad (4.4)$$

This allows two kinds of solutions, namely

$$w_j(x) = C \left[1 - \cos\left(N_j \frac{x}{l}\right) \right], \quad N_j = (j+1)\pi \quad \text{for } j = 1, 3, 5, \dots \quad (4.5)$$

and

$$w_j(x) = C \left[1 - \frac{2x}{l} - \cos\left(N_j \frac{x}{l}\right) + \frac{2 \sin\left(N_j \frac{x}{l}\right)}{N_j} \right], \quad N_j = (2j+1)\pi \quad \text{for } j = 2, 4, 6, \dots \quad (4.6)$$

where C is an arbitrary constant, N_j is the j^{th} mode of the normalised axial force N . In order to apply this analytical model to a pre-curved beam, Qiu et al. suggests to take the shape of the straight beam buckled in its first mode, $j = 1$, to be the as-fabricated shape of the beam. It has proven to be an adequate estimation for describing snap-through behaviour and has been adopted in numerous papers as analytical model [37, 59, 61]. The shape of the beam in its first buckled mode is described as follows:

$$\bar{w}(x) = \frac{h}{2} \left[1 - \cos\left(2\pi \frac{x}{l}\right) \right] \quad (4.7)$$

Whereby $\bar{w}(x)$ represents the as-fabricated shape over the position x along the beam, h the initial apex-height, l the horizontal span of the beam. This is visually presented in the schematic in fig. 4.1.

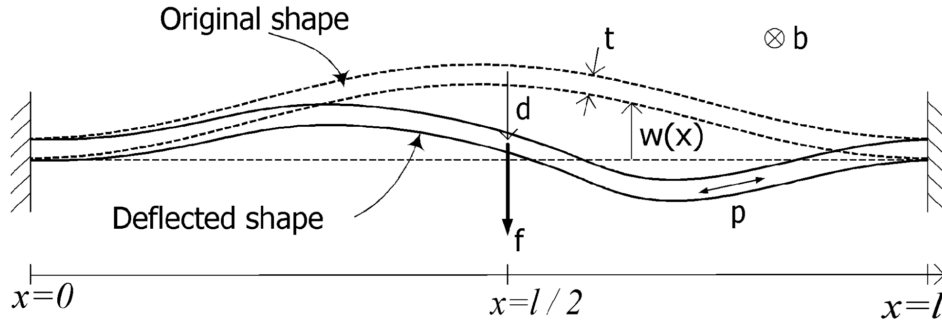


Figure 4.1: Schematic diagram of fixed-fixed beam [30]

The geometry constant Q is critical in determining the behaviour of the mechanism, as will be seen later in the model and is defined as:

$$Q = \frac{h}{t} \quad (4.8)$$

In fig. 4.1 both the original shape of the beam, described by eq. (4.7), and the deflected shape due to a vertical load f in the center of the beam are illustrated. The vertical load introduces a displacement d .

$$d = \bar{w}\left(\frac{l}{2}\right) - w\left(\frac{l}{2}\right) \quad (4.9)$$

Due to the vertical displacement the axial length will change accordingly, described by s .

$$s = \int_0^l \sqrt{1 + \left(\frac{dw}{dx}\right)^2} dx \approx \int_0^l \left[1 + \frac{1}{2} \left(\frac{dw}{dx}\right)^2 \right] dx \quad (4.10)$$

Axial force p occurs due to this change in length s relative to the initial length $s_{w=\bar{w}}$. Considering Hooke's law for axial deformation this can be described as:

$$p = Ebt \left(1 - \frac{s}{s_{w=\bar{w}}} \right) \quad (4.11)$$

Whereby b represents the out-of-plane thickness and t the thickness of the beam (see fig. 4.1). During deflection, the beam undergoes bending and compression. These effects can be observed in the change in bending energy, u_b , compression energy, u_s , and u_f , actuation energy.

$$\partial(u_b) = \partial \left[\frac{EI}{2} \int_0^l \left(\frac{d^2\bar{w}}{dx^2} - \frac{d^2w}{dx^2} \right)^2 dx \right] \quad (4.12)$$

$$\partial(u_s) = -p \partial(s) \quad (4.13)$$

$$\partial(u_f) = -f \partial(d) \quad (4.14)$$

The buckling mode superposition is used to solve the beam deflection. Since the modes of the clamped-clamped straight beam in eqs. (4.5) and (4.6) form an orthogonal set, they can be used as the superposition for the pre-curved beam. The variables are normalised in order to simplify the superposition:

$$X = \frac{x}{l}, W(X) = \frac{w(Xl)}{h} \quad (4.15)$$

This results in the superposition of the beam shape as follows

$$W(X) = \sum_{j=1}^{\infty} A_j W_j(X) \quad (4.16)$$

where

$$\left. \begin{array}{l} W_j(X) = 1 - \cos(N_j X) \\ N_j = (j+1)\pi \end{array} \right\} \quad j = 1, 3, 5, \dots \quad (4.17)$$

and

$$\left. \begin{array}{l} W_j(X) = 1 - 2X - \cos(N_j X) + \frac{2 \sin(N_j X)}{N_j} \\ N_j = 2.86\pi, 4.92\pi, \dots \end{array} \right\} \quad j = 2, 4, 6, \dots \quad (4.18)$$

The normalized as-fabricated beam shape then is

$$\bar{W}(X) = \frac{1}{2} W_1(X) \quad (4.19)$$

Next the applied force f and parameters can be normalised according to

$$F = \frac{fl^3}{EIh}, \quad \Delta = \frac{d}{h}, \quad S = \frac{sl}{h^2}, \quad N^2 = \frac{pl^2}{EI}, \quad U_b = \frac{ul^3}{EIh^2}, \quad U_s = \frac{ul^3}{EIh^2}, \quad U_f = \frac{ul^3}{EIh^2} \quad (4.20)$$

The rest of the derivation is detailed in appendix B. The eqs. (B.1), (B.3), (B.9), (B.10) and (B.12) to (B.14) define the $F - \Delta$ relation of the curved beam. The higher modes will be neglected to obtain closed form solutions. From eqs. (B.1), (B.9) and (B.12) and neglecting all modes above 3 we obtain a first solution:

$$F_1 = \frac{3\pi^4 Q^2}{2} \Delta \left(\Delta - \frac{3}{2} + \sqrt{\frac{1}{4} - \frac{4}{3Q^2}} \right) \left(\Delta - \frac{3}{2} - \sqrt{\frac{1}{4} - \frac{4}{3Q^2}} \right). \quad (4.21)$$

Note the dependence on Q , whereby the value must be greater than $\sqrt{16/3}$. The effect of this is shown in fig. 4.2. From eqs. (B.1), (B.3), (B.9) and (B.13) we obtain the second solution:

$$F_2 = \frac{N_1^2(N_2^2 - N_1^2)}{8} \left(\frac{N_2^2}{N_2^2 - N_1^2} - \Delta \right) = 4.18\pi^4 - 2.18\pi^4 \Delta \quad (4.22)$$

Which exists if both the second mode is not constrained and, by eqs. (B.3), (B.9) and (B.13), $Q > \frac{2N_2}{\sqrt{3}N_1} = 1.67$. From eqs. (B.1), (B.3), (B.9) and (B.14) we obtain the third solution:

$$F_3 = \frac{N_1^2(N_3^2 - N_1^2)}{8} \left(\frac{N_3^2}{N_3^2 - N_1^2} - \Delta \right) = 8\pi^4 - 6\pi^4 \Delta \quad (4.23)$$

which exists if both the second mode is constrained and, by eqs. (B.3), (B.9) and (B.14), $Q > 2N_3/\sqrt{3}N_1 = \sqrt{16/3}$.

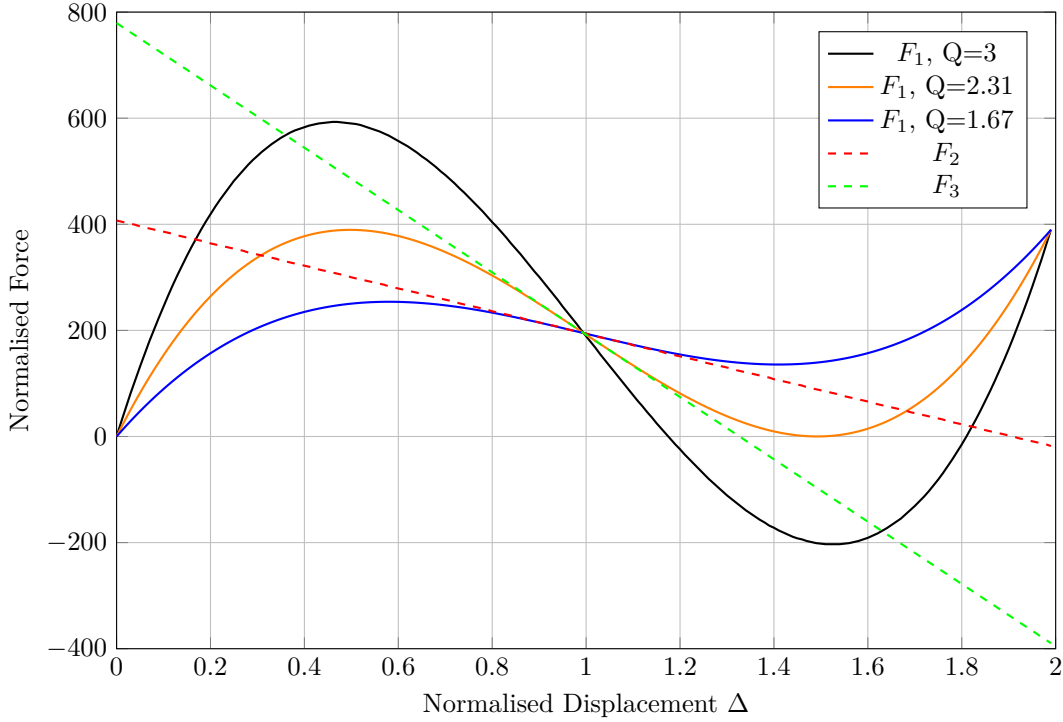


Figure 4.2: Normalised force-displacement showing several solutions

Influence of Q on buckling modes

The solutions eqs. (4.21) to (4.23) are shown in fig. 4.2, over the normalized vertical displacement $\Delta = 0$ to 2. F_2 and F_3 are straight lines with a negative slope that do not depend on Q . F_3 can exist only if mode 2 is constrained. F_1 depends on Q , but its values at $\Delta = 0, 1, 2$ are constants. Moreover, at $\Delta = 1$, F_1 , F_2 , and F_3 pass through the same point. The higher the Q , the higher the curving of F_1 . With $Q = 1.67$, F_1 becomes tangential to F_2 at $\Delta = 1$. With $Q = 2.31$, F_1 becomes tangential to F_3 at $\Delta = 1$. When Q is larger than those tangential values, curve F_1 has two more intersections with either F_2 or F_3 besides $\Delta = 1$. These two additional intersections are where the axial force equals that of the second mode or the third mode. Between these two intersections, either F_2 or F_3 exists, while outside this interior range of Δ , only F_1 exists. The actual $F-\Delta$ curve is therefore a hybrid curve that switches between the F_1 curve and either the F_2 or F_3 curve at these two intersections. The F_2 curve is always above zero except for its small negative value before $\Delta = 2$, which means that with the second mode free, even with a very high Q , the curved beam can be at most marginally bi-stable. On the other hand, the F_3 curve has a large portion below zero force. With the second mode constrained, the curved beam is bi-stable with $Q > 2.31$.

Let us consider the area covered by the negative force-displacement plot as “bi-stable energy” of a system with constrained second mode. If the plot does not reach negative forces, it will not have bi-stable energy and so the system is considered to be mono-stable. We can plot bi-stable energy vs Q to show the stability condition of $Q > \sqrt{16/3}$ or 2.31 in fig. 4.3. This plot gives the first geometric relation, namely between the apex height and the beam thickness, which can be used to tune the bi-stable behaviour. However, it is only valid for fixed-fixed boundary conditions. For this study, the boundaries exhibit variable stiffness which is addressed in the subsequent section.

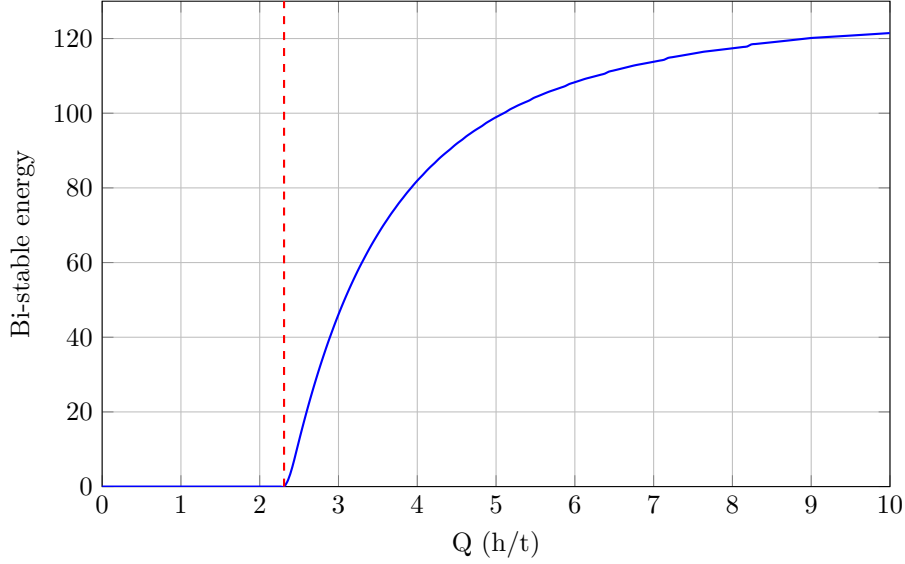


Figure 4.3: Normalised bi-stable energy versus Q (h/t). The red dashed line indicates the stability threshold of $Q = 2.31$

4.1.2. Variable stiffness boundary conditions

It is highly likely that in physical (non-simulated) bi-stable unit cells in metamaterials, the boundary conditions will not be fixed-fixed. That is because the unit cells in rows would experience cross-talk, as it is difficult to ensure sufficient fixed conditions for each unit cell. In this study, the purpose is to make use of this otherwise undesired variable stiffness in the boundary conditions and therefore it is an important feature to integrate into the analytical model. There are multiple approaches in literature which attempt to do so, and two of these will serve as inspiration for the final model of this design. Zhang et al. uses different material with certain stiffness dependent on temperature [37]. Hua et al. makes use of a gap in between each unit cell, allowing the supports of the unit cell to be bent [59]. In this design, the variable stiffness of the boundary conditions comes from both materials which have temperature dependent stiffness and a gap between each unit cell to allow for bending. Firstly, Zhang et al. introduces a variation in the axial compression energy, which stems from the equivalent stiffness of the supports. Since the non-fixed boundary conditions allow for more displacement along the beam, the axial force p is decreased accordingly. A dimensionless parameter c is defined to describe the relative stiffness of the support (k_s) and the axial stiffness of the beam (k_a). It is defined in such a way that if the support material is infinitely stiff, the value of c approaches 1, resulting in an axial force p under clamped-clamped boundary conditions. Adapting eq. (4.13) with this parameter c gives the following variation

$$p = \left(\frac{k_a k_s}{k_a + k_s} \right) (s_0 - s) = \left(\frac{k_a}{\frac{k_a}{k_s} + 1} \right) (s_0 - s) = ck_a (s_0 - s) \quad (4.24)$$

Where

$$s = \int_0^\lambda \sqrt{1 + \left(\frac{dw}{dx} \right)^2} dx \approx \int_0^\lambda \left[1 + \frac{1}{2} \left(\frac{dw}{dx} \right)^2 \right] dx \quad (4.25)$$

$$c = \frac{1}{\frac{k_a}{k_s} + 1} \quad (4.26)$$

After integration of parameter c into the calculations, the solution for the first mode F_1 , eq. (4.21), becomes

$$F_{c1} = \frac{3\pi^4 Q_c^2}{2} \Delta \left(\Delta - \frac{3}{2} + \sqrt{\frac{1}{4} - \frac{4}{3Q_c^2}} \right) \left(\Delta - \frac{3}{2} - \sqrt{\frac{1}{4} - \frac{4}{3Q_c^2}} \right). \quad (4.27)$$

where $Q_c = Q\sqrt{c}$. Zhang et al. define k_s in terms of compression into an elastic slab of finite thickness. However, the supports in this design are smaller in width than in height and act as cantilever beams. Hua et al. expressed the bending stiffness of the supports in terms of Euler beam theory:

$$k_s = \frac{bE}{4Q_2^3}, \quad Q_2 = \frac{h_2}{t_2} \quad (4.28)$$

Where h_2 and t_2 represent the height and thickness of the beam see fig. 4.4.

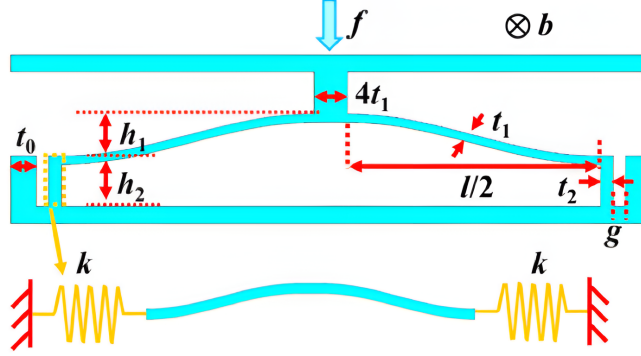


Figure 4.4: Parametric model of Hua et al. and its representation of the bending beams as springs with an equivalent stiffness k [59]

Note that the variable support stiffness by Hua et al. only takes into consideration one material, and thus one elastic modulus. The solution for Hua et al. is as follows:

$$F_{Hua} = \left(\left(\left(\frac{3}{2} - \Delta \right)^2 - \frac{1}{4} \right) \frac{3PQ_1^2}{P + 8Q_2^3} + 4 \right) \frac{\Delta\pi^4}{2} \quad (4.29)$$

Where P is equal to $\frac{l}{t}$. We can compare these two approaches by defining the support stiffness in the formulation of Zhang et al. in eq. (4.26) with bending stiffness and considering a mono-material system. Equating eq. (4.29) to eq. (4.27) then results in the following derivation:

$$c = \frac{P}{P + 8Q_2^3} \quad (4.30)$$

We then define k_a (axial beam stiffness) and k_s (support bending stiffness). Note that the axial stiffness is defined for half of the beam $\frac{l}{2}$:

$$k_a = \frac{2Ebt}{l}, \quad k_s = \frac{3EI}{h_s^3}, \quad I = \frac{bw_s^3}{12} \quad (4.31)$$

In which w_s and h_s represents the width and height of the support, respectively. This gives:

$$\frac{k_a}{k_s} = \frac{8th_s^3}{lw_s^3} \quad (4.32)$$

Substituting into eq. (4.26), we find that the solutions are identical:

$$c = \frac{\frac{l}{t}}{\frac{l}{t} + 8\frac{h_s^3}{w_s^3}} = \frac{P}{P + 8Q_2^3} \quad (4.33)$$

In this study, the formulation by Zhang et al., which incorporates a relative stiffness term c , will be adopted to integrate the elastic modulus of the second material. However, before introducing the multi-material case, we first examine the impact of variable stiffness boundary conditions on the stability criteria for a mono-material system. Unlike in a fixed-fixed configuration, where stability is governed solely by Q , the threshold in this case also depends on the relative stiffness c . To establish the new

stability criterion, we normalise h and t as h/l and t/l . Furthermore, we combine the support dimensions in the ratio h_s/w_s . Given that $Q_c > \sqrt{16/3}$, the exact stability threshold can now be defined as:

$$Q_c = \frac{h l}{l t} \sqrt{\frac{1}{8 \frac{t}{l} (\frac{h_s}{w_s})^3 + 1}} > \sqrt{\frac{16}{3}} \quad (4.34)$$

This is best illustrated by seeing how the minimum value of Q , which was previously 2.31, now significantly increases with increasing h_s/w_s in order to maintain a bi-stable system (see fig. 4.5). This represents the bi-stability criteria for a system with bending supports, made out of a single material. The red line in the plot indicates the exact threshold which is defined by eq. (4.34). To put this in perspective, it is the same bi-stable energy plotted in fig. 4.3 and as can be seen the critical value of Q now increases from 2.31 as the ratio of h_s/w_s increases.

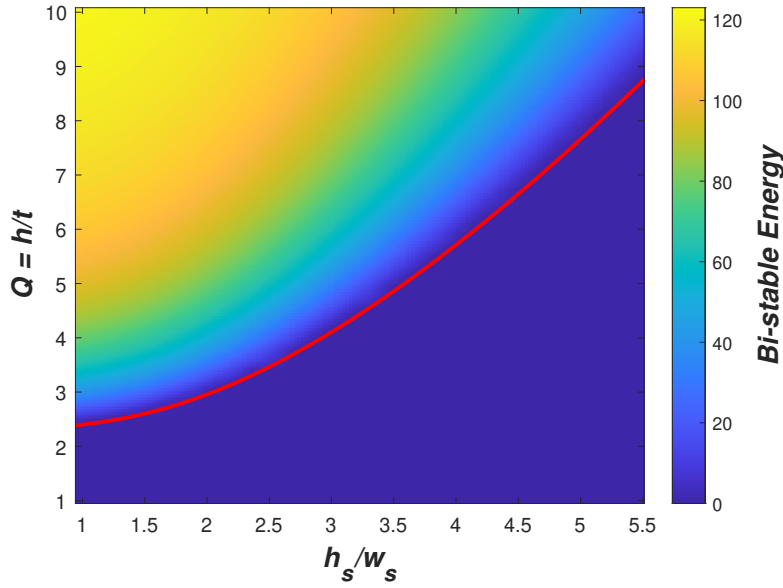


Figure 4.5: Q vs h_s/w_s at constant value of $t/l = 0.01$

Since the design makes use of two materials, the integration of the variable stiffness by Zhang et al. is more suitable as the second Young's modulus can be inserted in the definition of k_s , by simply using E_2 instead of E . This in turn, increases the complexity of the stability criteria. The ratio of the beam and support elastic modulus E_1/E_2 is now introduced as follows:

$$Q_c = \frac{h l}{l t} \sqrt{\frac{1}{8 \frac{t}{l} (\frac{h_s}{w_s})^3 \frac{E_1}{E_2} + 1}} > \sqrt{\frac{16}{3}} \quad (4.35)$$

As the model introduces multiple materials, its stability is influenced not only by its geometry but also by the ratio of elastic moduli, E_1/E_2 (fig. 4.6). The impact of E_1/E_2 can be interpreted in two ways. First, one can assess whether a system with a given geometry (defined by Q and h_s/w_s) will exhibit bi-stability or mono-stability depending on the relative elastic modulus E_1/E_2 . Second, E_1/E_2 can be considered in relation to temperature, where an increase in E_1/E_2 corresponds to an increase in temperature. For the analytical model, the exact transition temperature cannot be determined without incorporating the specific storage moduli of materials. However, it is possible to identify the ratio of E_1/E_2 at which the system shifts from bi-stability to mono-stability, which would correspond to a certain temperature. For instance, consider a system with $Q = 6$ and $h_s/w_s = 2$. In both fig. 4.6a and fig. 4.6b, it can be observed that when $E_1/E_2 > 10$, the system transitions to mono-stability. To achieve a lower transition temperature, either Q can be decreased or h_s/w_s can be increased. The effect of these changes can be significant; for example, a system with $Q = 5$ already transitions when $E_1/E_2 > 6$. This demonstrates the sensitivity of the system to geometric variations. It is further observed that when

$E_1/E_2 < 1$, meaning the beam is less stiff than the supports, the influence of h_s/w_s is considerably smaller, and the system remains bi-stable even at high values of h_s/w_s .

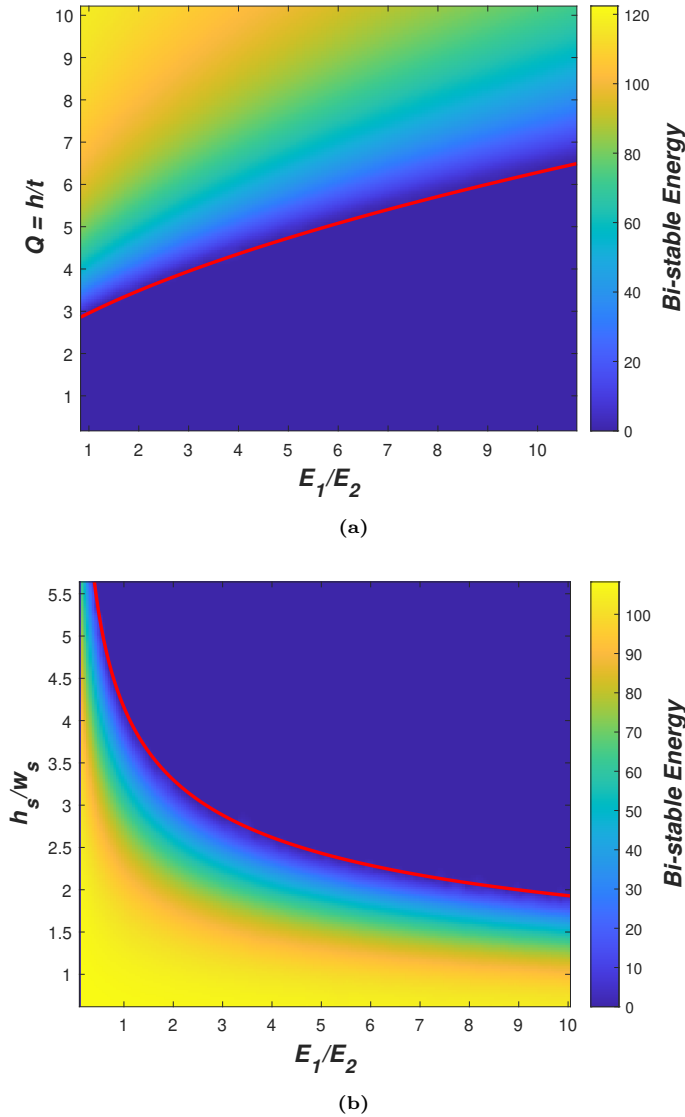


Figure 4.6: Comparison of analytical plots showing the relationship between key parameters. The $t/l = 0.01$ for both plots. (a) A constant value of $h_s/w_s = 2$ is chosen for this plot. (b) A constant value of $Q = 6$ is chosen for this plot.

4.1.3. Bi-material boundary conditions

The last addition to this analytical model is the use of multi-material supports. The analysis of solid beams in bending assumes that elongation and contraction of longitudinal fibres are proportional to their distance from the neutral axis [62]. For beams with multiple materials, the problem becomes statically indeterminate and requires principles of static equilibrium, geometric compatibility, and superposition. Beam theory also assumes no slippage between materials and that all remain elastic, allowing the radius of curvature to determine strains. To overcome this, Niknam et al. [36] employ the method known as transformed sections. This enforces strain compatibility by converting one material into an equivalent of another, which allows the member to be analysed as a homogeneous section. The approach is illustrated in fig. 4.7.

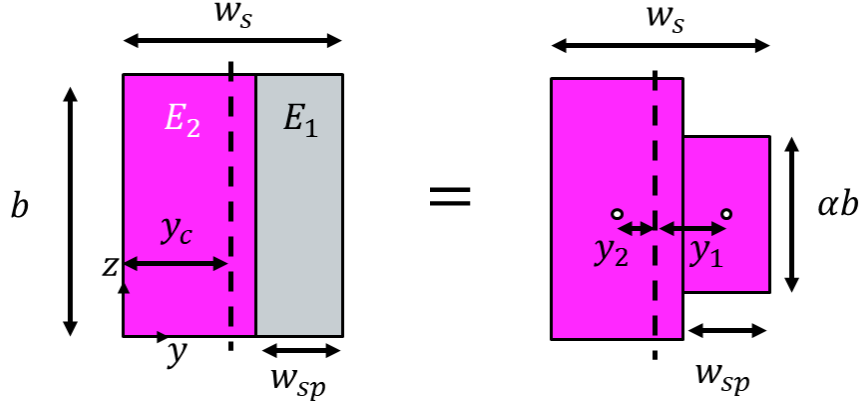


Figure 4.7: Schematic to represent transformed sections

To transform the passive material into the active material first the ratio of the Elastic modulus is required:

$$\alpha = \frac{E_1}{E_2} \quad (4.36)$$

Then the equivalent surface area of the sections can be transformed as follows:

$$w_s = w_{sa} + w_{sp}, \quad A_1 = \alpha b w_{sp}, \quad A_2 = b w_{sa} \quad (4.37)$$

Where w_{sp} and w_{sa} represent the width of the passive and active material in the beam, respectively. Next the neutral axis (y_c) is calculated:

$$y_c = \frac{A_1 y_1 + A_2 y_2}{A_1 + A_2}, \quad y_1 = \frac{w_{sp}}{2}, \quad y_2 = w_{sp} + \frac{w_{sa}}{2} \quad (4.38)$$

The equivalent moment of inertia becomes:

$$I_{eq} = \frac{\alpha b w_{sp}^3}{12} + A_1 (y_c - y_1)^2 + \frac{b w_{sa}^3}{12} + A_2 (y_c - y_2)^2 \quad (4.39)$$

Now we can substitute eq. (4.39) into eq. (4.31) which results in:

$$k_s = \frac{3E_2 I_{eq}}{h_s^3} \quad (4.40)$$

This last addition of multi-material supports provides the final stability threshold. To work with the previously defined dimensionless ratios, some terms must be re-expressed. We express E_1 as $E_2 \cdot \frac{E_1}{E_2}$. We let β represent the fraction $\frac{w_{sp}}{w_s}$, and $\frac{E_1}{E_2}$ as α for clarity. Substituting these into $\frac{k_a}{k_s}$ gives:

$$\frac{k_a}{k_s} = \frac{8\alpha h_s^3 t (\alpha\beta - \beta + 1)}{l w_s^3 (\alpha^2\beta^4 - 2\alpha\beta^4 + 4\alpha\beta^3 - 6\alpha\beta^2 + 4\alpha\beta + \beta^4 - 4\beta^3 + 6\beta^2 - 4\beta + 1)} \quad (4.41)$$

By dividing the present components from the previous stability threshold ($8 \frac{t}{l} \frac{E_1}{E_2} (\frac{h_s}{w_s})^3$) from this equation we are left with the resultant influence of the composition of the bi-material beam as:

$$\gamma = \frac{(\alpha\beta - \beta + 1)}{(\alpha^2\beta^4 - 2\alpha\beta^4 + 4\alpha\beta^3 - 6\alpha\beta^2 + 4\alpha\beta + \beta^4 - 4\beta^3 + 6\beta^2 - 4\beta + 1)} \quad (4.42)$$

Resulting in the final threshold to be:

$$Q_c = \frac{h}{l} \frac{l}{t} \sqrt{\frac{1}{8 \frac{t}{l} (\frac{h_s}{w_s})^3 \frac{E_1}{E_2} \gamma + 1}} > \sqrt{\frac{16}{3}} \quad (4.43)$$

Finally, the stability thresholds for the complete analytical model can be plotted, which are indicated by the red contours, derived from eq. (4.43). The plots in figs. 4.8 to 4.10 reveal non-linear relationships

between the various parameters. In fig. 4.8, the effect of the storage modulus ratio $E_1/E_2 = 5$ is evident: as the proportion of passive material in the support increases, the minimum value of Q to hold bi-stability decreases.

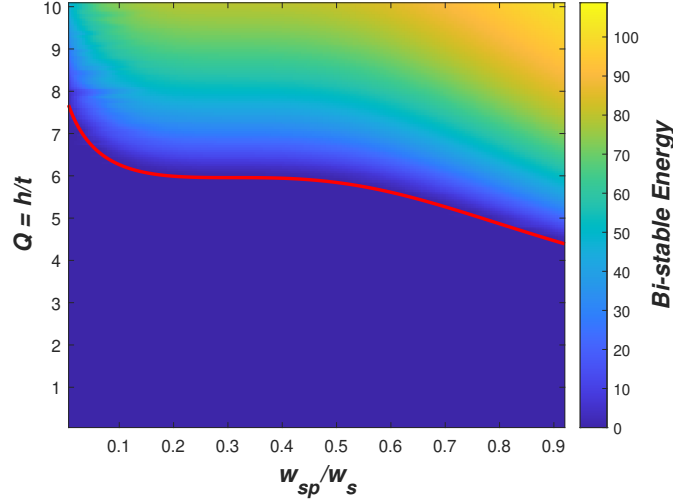


Figure 4.8: Q vs. w_{sp}/w_s for $E_1/E_2 = 5$, $h_s/w_s = 3$.

In fig. 4.9, the value of Q is set to 6, with $h_s/w_s = 3$. As anticipated, when $w_{sp}/w_s = 1$, indicating a support composed entirely of passive material, there is no noticeable change in bi-stable behaviour over the range of $E_1/E_2 > 1$. Furthermore, the plot shows that higher E_1/E_2 values are required for the system to transition to mono-stability as w_{sp}/w_s increases. This suggests a potential method for tuning the transition temperature: increasing the passive material ratio within the support raises the transition threshold. Notably, the sharp rise in the bi-stability threshold around $w_{sp}/w_s = 0.7$ may indicate that, beyond this point, achieving mono-stability becomes increasingly difficult through temperature. However, the exact point may vary depending on the specific values of Q and h_s/w_s .

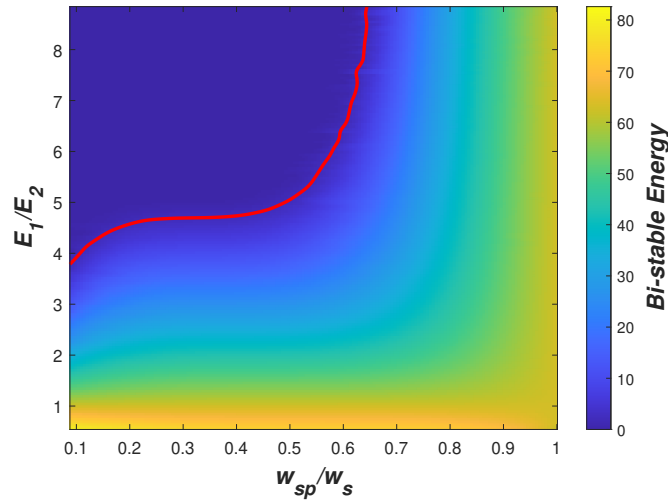


Figure 4.9: E_1/E_2 vs. w_{sp}/w_s for $Q = 6$, $h_s/w_s = 3$.

The influence of h_s/w_s and w_{sp}/w_s on the stability threshold is examined in fig. 4.10, with constants $E_1/E_2 = 5$ and $Q = 6$. Given that the storage modulus of m_1 is five times that of m_2 , it is not surprising that increasing w_{sp}/w_s enhances the stability of more flexible supports (higher h_s/w_s values).

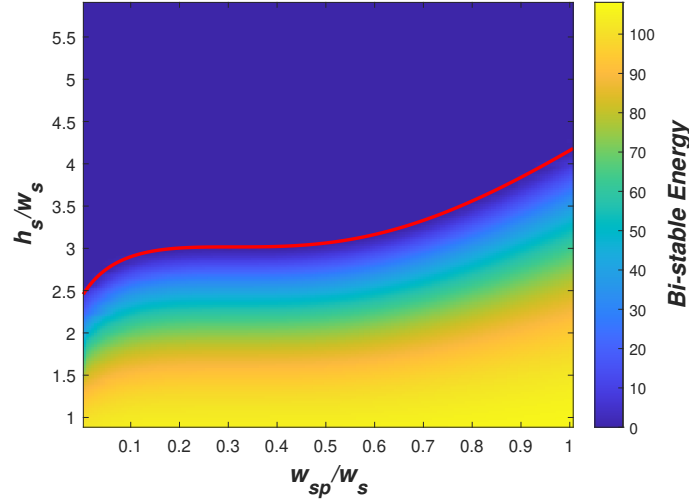


Figure 4.10: h_s/w_s vs. w_{sp}/w_s for $Q = 6$, $E_1/E_2 = 5$.

4.1.4. Influence of beam material on stability

Niknam et al. observed that in samples composed of TPU and CFR Nylon, an increase in the ratio of the stiffer active material (CFR Nylon) within the supports resulted in a higher transition temperature [36]. This translates to requiring a higher E_1/E_2 as w_{sp}/w_s decreases. At first glance, this observation may appear to contradict the trend shown in fig. 4.9, where an increase in passive material, w_{sp}/w_s , leads to a higher stability threshold. However, a key distinction is that Niknam et al. employed a rubber-state beam, which had a significantly lower elastic modulus than the active material. In their case, the stiffness ratio at operating temperature was $E_1/E_2 = 0.05$. To illustrate this effect more clearly, fig. 4.11 presents the stability behaviour when the range of E_1/E_2 is restricted to 0.1 to 1. Under these conditions, a different stability trend emerges. By slightly adjusting the fixed parameters to $h_s/w_s = 4$ and $Q = 5$, the trend observed by Niknam et al. is reproduced: a higher fraction of active material ($w_{sp}/w_s \rightarrow 0$) increases stability, thereby requiring a higher E_1/E_2 for the system to transition to mono-stability. This highlights a fundamental difference in how transition temperature tuning is influenced by the choice of beam material.

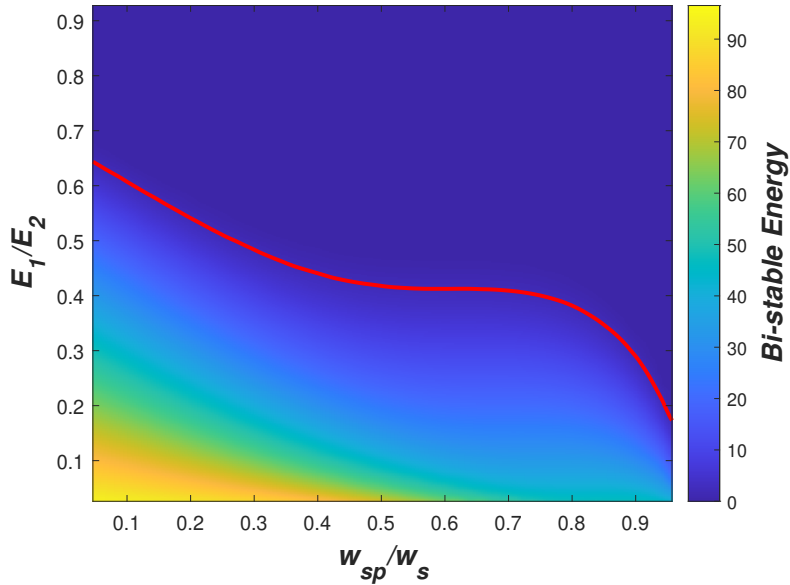


Figure 4.11: Effect of active material fraction on transition temperature with a rubber-state beam

So far it has been demonstrated that the bi- to mono-stability threshold is determined at the point where $Q_c < \sqrt{16/3}$. Since Q is a geometric parameter, it will remain constant over temperature. As previously stated, the relationship is given by:

$$Q_c = Q\sqrt{c}, \quad (4.44)$$

where

$$c = \frac{1}{8 \frac{t}{l} \left(\frac{h_s}{w_s}\right)^3 \frac{E_1}{E_2} \gamma + 1}. \quad (4.45)$$

For every value of Q , there exists a corresponding critical value of c , denoted as c_r , at which the stability threshold is reached:

$$c_r = \frac{16}{3Q^2}. \quad (4.46)$$

Thus, if $Q = \sqrt{16/3}$, then $c_r = 1$, and as Q increases, the critical relative stiffness decreases. Notably, c is independent of the normalised apex height h/l . This allows us to examine how the critical stiffness shifts with increasing Q , which is achieved by maintaining a fixed t/l while varying h/l . To visualise this, the relative stiffness is plotted for a constant t/l and h_s/w_s over a given range of E_1/E_2 and w_{sp}/w_s . The stability thresholds are now defined by c_r rather than Q_c , as was previously done in figs. 4.8 to 4.10. For two distinct ranges of E_1/E_2 , the relative stiffness are plotted in figs. 4.12 and 4.13. To maintain consistency in comparing the two cases, the fixed constant h_s/w_s was doubled for the inverse range in fig. 4.13 to ensure that the same values of Q appear as in fig. 4.12. It can be observed that for both ranges of E_1/E_2 , the required composition of the support, w_{sp}/w_s , to induce a bi-stable to mono-stable transition changes significantly with Q . For instance, in fig. 4.12, when $Q = 4$, the stability threshold remains relatively unchanged until $w_{sp}/w_s \approx 0.8$, beyond which it increases sharply. This indicates that up to this point, the system is capable of transitioning to mono-stability within the given range of E_1/E_2 . Conversely, for $Q > 6$, the likelihood of achieving a transition is significantly reduced, requiring the support to consist of minimal or no passive material. In general, for a system with a feasible range of $E_1/E_2 = 1$ to 10, lower values of Q can tolerate a higher proportion of passive material in the support while still enabling a transition. Increasing either Q or w_{sp}/w_s raises the transition temperature.

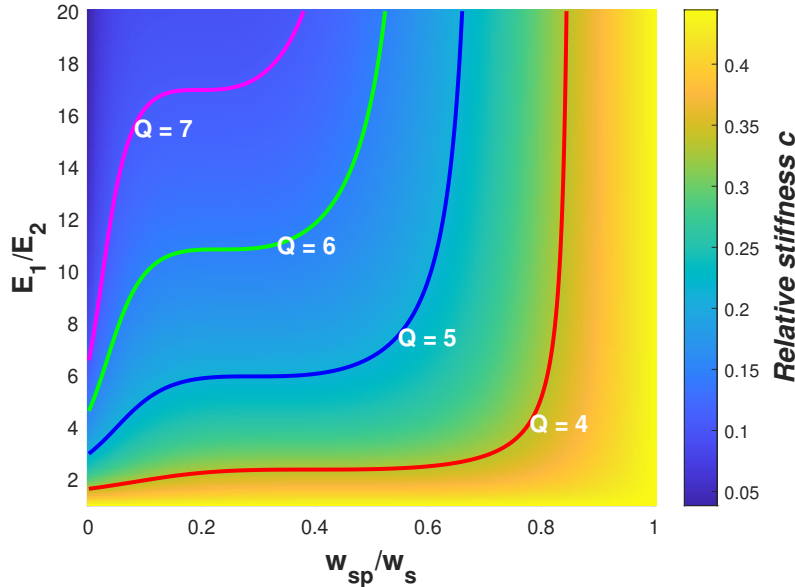


Figure 4.12: Critical stiffness contour for passive material in glass state, with constants: $t/l = 0.01$, $h_s/w_s = 2.5$.

In contrast, for a system with $E_1/E_2 = 0.1$ to 1, a higher Q provides a broader range of w_{sp}/w_s values within which a transition remains possible. This can be observed by comparing $Q = 7$ and $Q = 4$ in

fig. 4.13. For the lower Q values, if the fraction of passive material in the support is too high, rather than remaining bi-stable across the full range of E_1/E_2 , the system may already be mono-stable across the full range of E_1/E_2 . Similarly to the range in fig. 4.12, increasing Q increases the transition temperature, but in contrast, decreasing w_{sp}/w_s raises the transition temperature. It is important to note that these observations are specific to a system with particular values of t/l and h_s/w_s , and while they provide a general understanding, variations in these constants may slightly alter the results. Overall, these findings illustrate how the system's geometry and material properties influence the sensitivity of the stability threshold and the feasible transition temperatures.

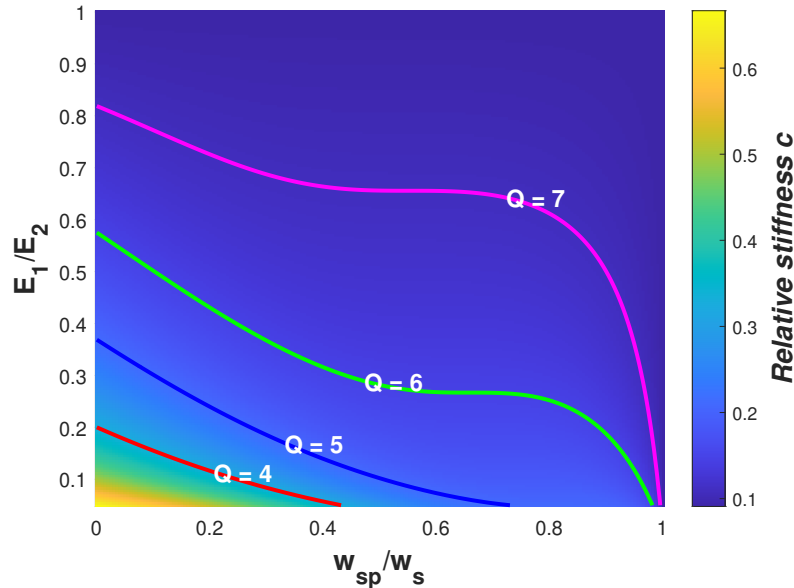


Figure 4.13: Critical stiffness contour for passive material in rubber state, with constants: $t/l = 0.01$, $h_s/w_s = 5$.

4.2. Finite Element Model

With Finite Element Analysis (FEA), the proposed design can be calculated numerically. This alternative method can be used to verify the analytical model to a certain degree while also being able to simulate the behaviour of more complex geometries. Additionally, FEA can incorporate boundary conditions that more accurately reflect those of a physical sample, rather than relying on idealized assumptions. For example, the assumption in the analytical model of using the relative stiffness c . This can be investigated and determined how accurately it affects the snap-through behaviour, compared to the numerical model. The disadvantage of FEA is the long computational time, which is why only a selection of specific geometries can be compared.

The chosen FE software is Ansys workbench with a transient structural analysis. The design is analysed in 2D rather than 3D, reducing computation time. Plane stress assumptions were chosen over plane strain as it is expected that the stresses in the out-of-plane direction are negligible compared to the in-plane stresses due to the beam's relatively low thickness. The elements are PLANE183 and the size of the elements was chosen such that there were 5 elements along the thickness of the beam. Overall, the amount of elements was around 6560 and 21293 nodes per unit cell. The existing analytical model for fixed-fixed boundary conditions has already shown strong agreement with FE models and experimental results [30]. Therefore, in this study, the FE model is used to assess the adjustments introduced, specifically the implementation of variable stiffness boundary conditions (bending supports) and temperature-dependent stiffness. A second FE model of a layered system with more complex geometry was simulated. This was done to evaluate the active programmability of the proposed design, involving a sequence of mechanical loading followed by selective thermal stimulation of one layer.

4.2.1. Variable stiffness boundary conditions

In the analytical model, the stiffness of the supports was reflected by a stiffness k_b , which was based on Euler-Bernoulli beam theory. The assumptions made in Euler-Bernoulli beam theory are:

- Cross sections of the beam do not deform in a significant manner under the application of transverse or axial loads and can be assumed as rigid.
- During deformation, the cross section of the beam is assumed to remain planar and normal to the deformed axis of the beam.

In general, this is met when the beam is a slender beam with small rotations [56]. This translates to a ratio h_s/w_s that should be larger than 10 and the rotation of the neutral axis should be smaller than 5° . In the analytical model, it was observed that the larger the ratio of h_s/w_s , the more the system tends to mono-stability. In order to maintain bi-stability, the other parameters need to be adjusted to compensate for the large h_s/w_s ratio. The minimum Q value for a system with $h_s/w_s = 10$ decreases as the thickness decreases according to eq. (4.34). Some of the calculated values from the analytical model are presented in table 4.1.

Beam Thickness/Length (t/l)	Minimum Q
1	206.6
0.1	65.3
0.01	20.7
0.001	6.6

Table 4.1: Beam thickness-to-length ratio (t/L) and corresponding minimum Q for $h_s/w_s = 10$.

With the fabrication method at centimetre-scale in mind, the minimum thickness will roughly be 1 mm, and the beam length could be up to 100 mm to limit the size of the overall unit cell. This corresponds to a minimum Q value of around 20.7, which translates to an apex height of 20 mm, in order to uphold the assumptions of Euler-Bernoulli. Depending on the material's properties, this may result in relatively high forces and stresses in the system. Therefore, a lower h_s/w_s would be more suitable for the design space of this study. Through FEA we can investigate whether the snap-through behaviour with smaller ratios of h_s/w_s can still agree with the analytical model based on slender supports. It is expected, that the analytical model will overestimate the stiffness of the supports at lower values of h_s/w_s . This is because the analytical model does not account for shearing. For this comparison, a mono-material design is used as the multi-materials will be addressed in the temperature dependent section in section 4.2.2. The material is considered to be linear elastic. The changing variable is the ratio of h_s/w_s to see how the variation in boundary conditions is reflected in both models in the force-displacement curve. The chosen dimensions are listed in section 4.2.1 and the loading and constraint conditions are illustrated in fig. 4.14. The Elastic modulus was extracted from the DMA results in section 5.2.

Parameter	Value
b	10 [mm]
t	1 [mm]
h_s	12 [mm]
h	5, 6 [mm]
l	90 [mm]
w_s	3, 4, 6 [mm]
E	1285 [MPa]
Q	5, 6
h_s/w_s	4, 3, 2

Table 4.2: Model Dimensions and Parameters

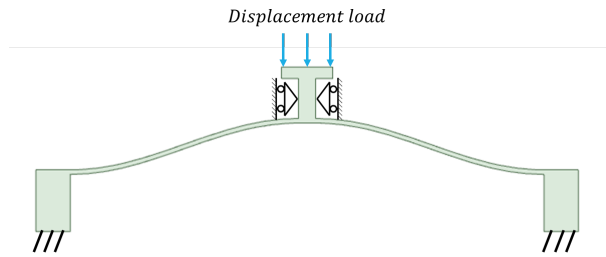


Figure 4.14: FE Constraints for the mono-material model. Frictionless supports are placed at the sides of the top beam to constrain the second buckling mode. The supports have fixed boundary conditions to the ground.

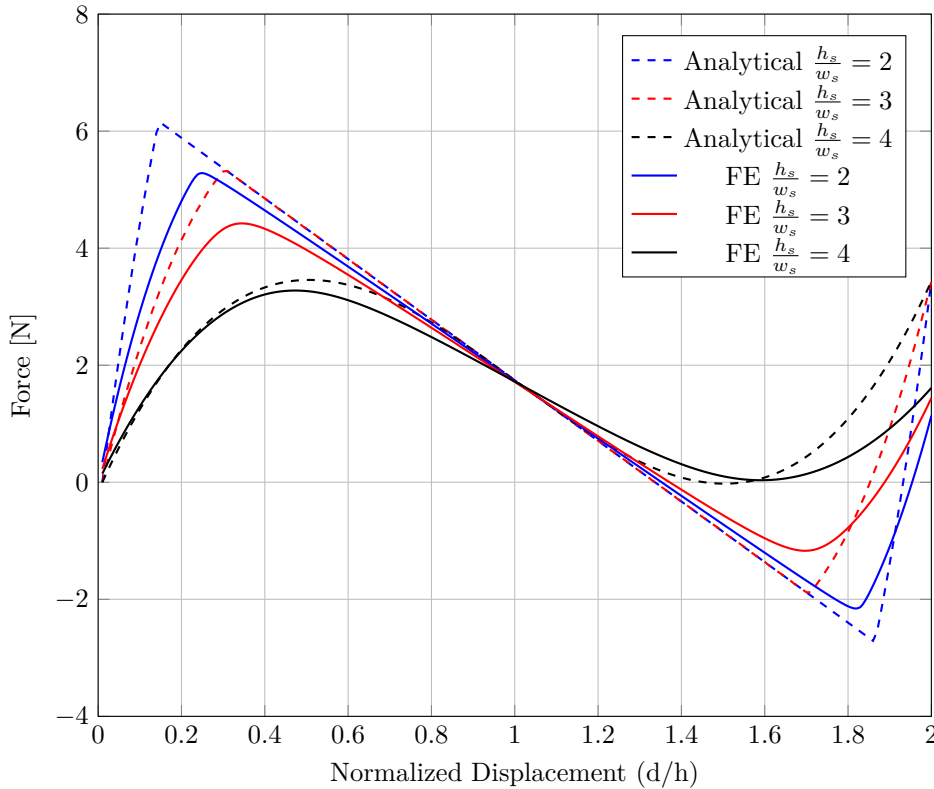


Figure 4.15: Comparison of Analytical (dashed) and FE (solid) Force vs. Normalized Displacement Curves.

In fig. 4.15, both the analytical and FE results demonstrate a clear reduction in bi-stability as the ratio h_s/w_s increases. The analytical results exhibit slightly larger magnitudes, with the discrepancy growing as h_s/w_s decreases. This trend aligns with the expectation that the Euler-Bernoulli assumptions are not fully satisfied. Additionally, differences in force magnitudes between the analytical and FE models may arise because only the first three buckling modes are considered in the analytical approach. Qiu et al. observed that incorporating higher-order modes enhances the accuracy of snap-through behaviour, resulting in more rounded peaks at critical forces. Furthermore, while the FE model captures a slight variation in the negative stiffness slope for the cases where $h_s/w_s = 3, 4$, the analytical model maintains an identical slope as the system enters the negative stiffness regime. This is because the analytical model exclusively employs the third buckling mode for systems with $Q > 2.31$ and switches to the second mode for lower Q values. Including additional higher modes could potentially reflect these deviations. Finally, in both models, increasing h_s/w_s shifts the displacement point at which both the minimum and maximum critical forces occur closer to $\Delta = 1$. This results in a more gradual transition compared to the nearly fixed boundary conditions observed for lower h_s/w_s values. This behaviour is likely due to the increased flexibility of the supports, allowing for greater horizontal displacement before sufficient compression is reached to trigger buckling.

To further investigate the impact of satisfying the Euler-Bernoulli assumption, an additional comparison was conducted with $h_s/w_s = 10$ to assess whether it improves the agreement between the two models. The dimensions used are listed in table 4.3, with the Elastic modulus of PEEK applied [63]. The corresponding force-displacement plot is presented in fig. 4.16. It is observed that, during the initial displacement phase, the two models exhibit nearly identical behaviour. However, as the FE model transitions into the negative stiffness region, it does so at an earlier stage compared to the analytical model, which maintains a sharper critical force. At the minimum critical force, the FE model again shows a smoother transition relative to the analytical model. Although ensuring $h_s/w_s = 10$ to meet the Euler-Bernoulli assumption improves the alignment between the two models to some extent, minor discrepancies persist. These remaining differences are likely due to the exclusion of higher-order buckling modes in the analytical model, reinforcing the importance of their inclusion for enhanced accuracy.

Overall, it can be stated that the analytical and FE models show agreement with the varying boundary conditions both in general trends of the snap-through behaviour and the order of magnitude.

Parameter	Value
b	1 [mm]
t	0.01 [mm]
h_s	0.1 [mm]
h	0.1 [mm]
l	10 [mm]
w_s	0.1 [mm]
E	3.6 [GPa]
Q	10
h_s/w_s	10

Table 4.3: Model Dimensions and Parameters

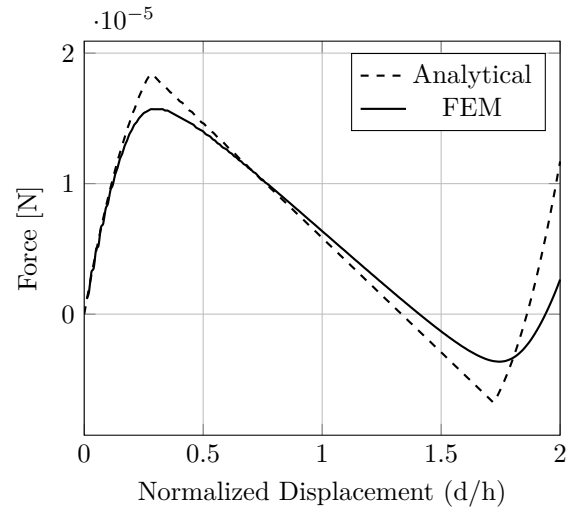


Figure 4.16: Comparison of Analytical (dashed) and FE (solid) Force vs. Normalized Displacement Curves.

4.2.2. Temperature dependent stiffness

The next comparison between the analytical and FE results incorporates multi-material supports and temperature dependence. Since the force-displacement curves are already compared for multiple variations of h_s/w_s in section 4.2.1, this section focuses on determining the transition temperature. Additionally, the effect of the support ratio between active and passive material, w_{sp}/w_s , is examined. To compare the analytical model's stability threshold with the FE model, two models with $Q = 5$ and $Q = 6$ are simulated with varying ratios of w_{sp}/w_s . The support materials have a bonded connection between the contact region. This enforces that no sliding or separation between the faces is allowed. In the loading sequence, applying a force rather than a displacement allows the system to be positioned into its deformed stable state. Subsequently, by gradually increasing the temperature after removing the force load, the system may eventually snap back to its original configuration, or remain in place. The temperature increased by roughly 0.2 °C per step. The storage moduli are extracted from the DMA results in section 5.2. Some key temperatures and the respective storage moduli for this comparison are indicated in table 4.5. The loads and constraints are depicted in fig. 4.17. The dimensions of the models are presented in table 4.4.

Table 4.4: Model Dimensions and Parameters

Parameter	Value
b	10 [mm]
t	1 [mm]
h_s	12 [mm]
h	5, 6 [mm]
l	90 [mm]
w_s	6 [mm]
Q	5, 6
h_s/w_s	2

Table 4.5: Temperature and Elastic Moduli of Materials

Temp. (°C)	E_1 (MPa)	E_2 (MPa)	E_1/E_2
30	1285	1823	0.7
62	1210	480	2.5
63	1206	238	5.0
65	1195	113	10.6

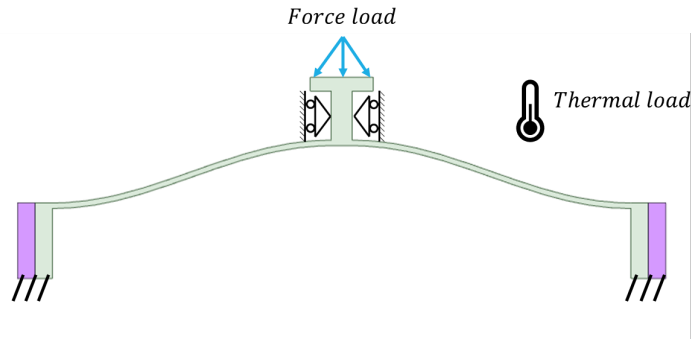


Figure 4.17: Constraints and loads on multi-material support FE model. The frictionless supports constrain the second buckling mode. The thermal load is applied globally.

The transition temperature is linked to the stiffness ratio E_1/E_2 for a given combination of materials. Consequently, the critical value of E_1/E_2 corresponding to each transition temperature obtained from the FE model can be derived. The results of the transition temperature and the critical stiffness ratio E_1/E_2 with variable w_{sp}/w_s are illustrated in fig. 4.19 and fig. 4.18, respectively, where both the analytical and FE model are compared.

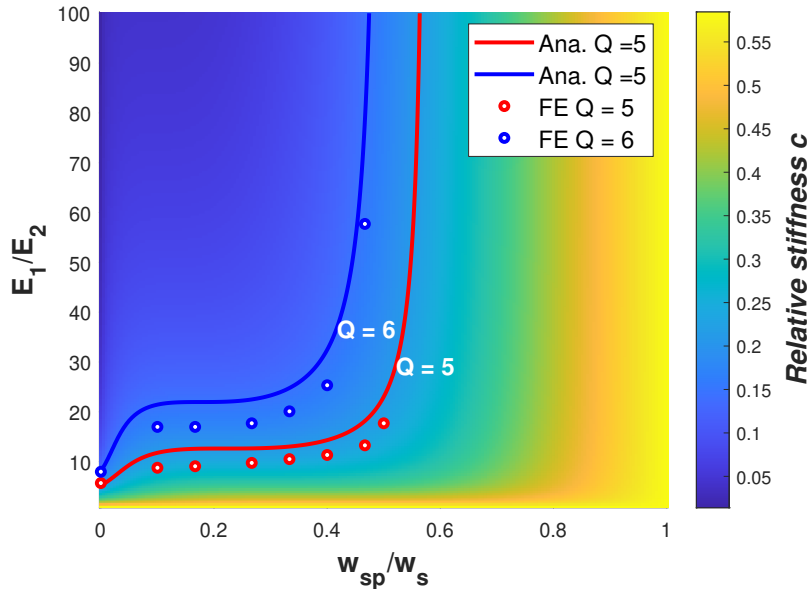


Figure 4.18: Comparison of critical stiffness contours of FEM points versus the analytical model for a system with $Q = 6$ and $Q = 5$

Firstly, these results indicate that the analytical and FE models exhibit similar trends in transition temperature as w_{sp}/w_s varies. However, the FE model consistently predicts lower critical values than the analytical model, a discrepancy that is evident in both the transition temperature and E_1/E_2 plots. It is an expected result based on the previous comparison in section 4.2.1 where it was observed that the analytical model predicts higher critical forces and therefore more bi-stability compared to the FEM model. Notably, since the stiffness ratio E_1/E_2 is highly sensitive to small changes in temperature, the relative error in transition temperature is at most 1.4%, whereas the relative error in E_1/E_2 reaches up to 39%. This is expected, as the stepwise temperature increment of 0.2°C can result in significant variations in E_1/E_2 , introducing challenges in achieving precise numerical agreement.

The ratio E_1/E_2 is a key component of the critical relative stiffness c_r , which remains constant for a given design parameter Q in the analytical model, independent of w_{sp}/w_s . The FE model, however, shows some deviation in the critical relative stiffness based on the predicted transition temperatures. A

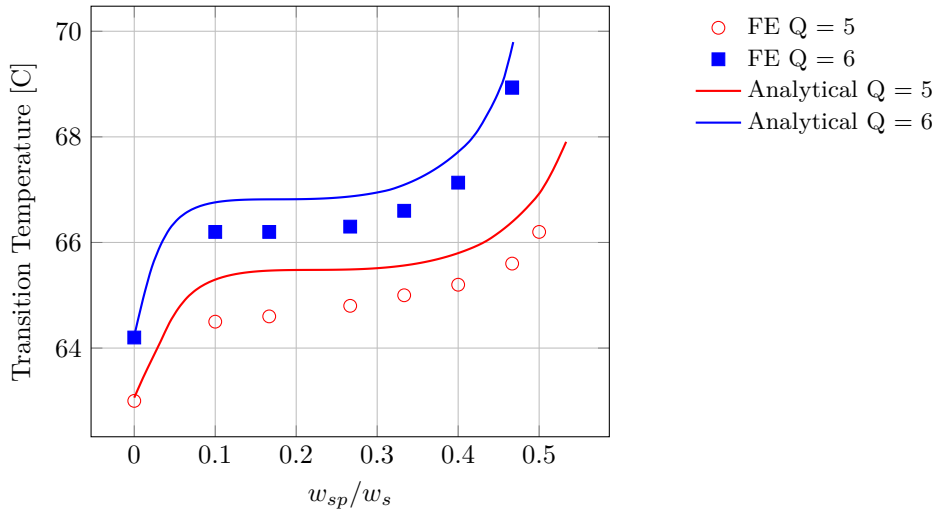


Figure 4.19: Comparison of transition temperatures between FE model and analytical model for $Q = 5$ and $Q = 6$, with varying w_{sp}/w_s

comparison between the analytically derived constant and the FEM results is presented in ??, illustrating the deviations observed in numerical predictions. In this plot it is observed that for both models, the support material composed entirely out of the active material shows the highest agreement between the analytical and the FEM model. The points with increased passive material in the support do not show a clear constant critical relative stiffness. The uncertainty of the critical relative stiffness derived from the FEA is due to the highly temperature dependent storage moduli whereby a small change can alter the result. Overall, the points from the FE are relatively close to the analytical model, but may improve with smaller step size and potentially with a smaller mesh size.

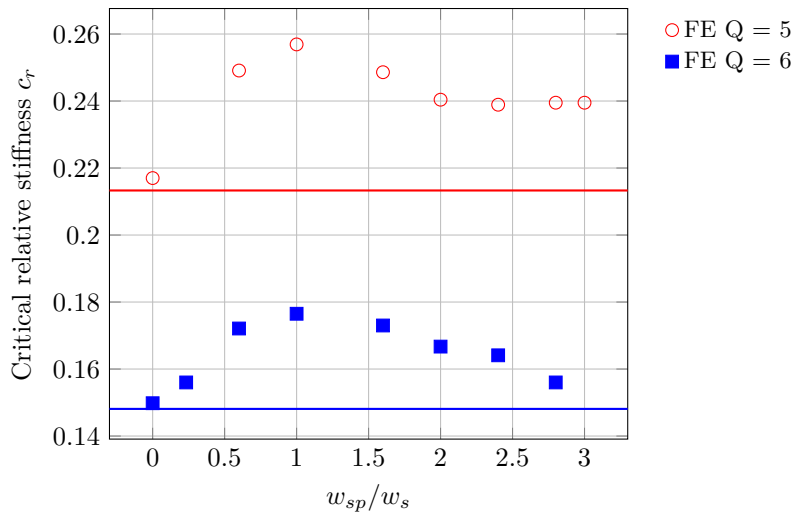


Figure 4.20: Comparison of critical relative stiffness derived from FE results and analytical model constant value for $Q = 5$ and $Q = 6$, with varying w_{sp}/w_s

4.2.3. Example simulation of Actively Programmed Multi-Stable Structure

Lastly, FEA can be employed to simulate more complex and layered structures that cannot be accurately captured by the analytical model. An example of such a structure is illustrated in fig. 4.21, which features a 2×2 configuration with curved supports (blue) instead of simple rectangular supports. The boundary conditions ensure that the load is uniformly applied while preventing rotation of the top plate, whereas the supports of the two layers remain free to bend. The different displacement states

during the loading sequence are illustrated by the figures above the plot. Initially, the structure is gradually loaded by 3.5 N over the first 2.5 seconds, at which point the top layer snaps. To verify the stability of this new configuration, the force is then reduced to 0 N, and it is observed that the new position is maintained. Then, the load is gradually increased again to 4.5 N, causing the bottom layer to snap. The force is then dropped to 0 N once more, and the system remains stable in its newly deformed state. To demonstrate the effect of active programming, a thermal load is applied to only the bottom support after a one-second hold. The temperature is gradually increased from 30°C to 80°C. As a result, the bottom layer snaps back at approximately 65°C, leading to a final configuration where the top layer remains closed while the bottom layer reopens. This effectively resets the system to its second configuration, demonstrating the desired effect described in fig. 2.1b and aligning with the functional requirements introduced in chapter 1. With passive programmability alone, this second configuration could only have been achieved by fully unloading the system to its completely open state before re-applying mechanical loading.

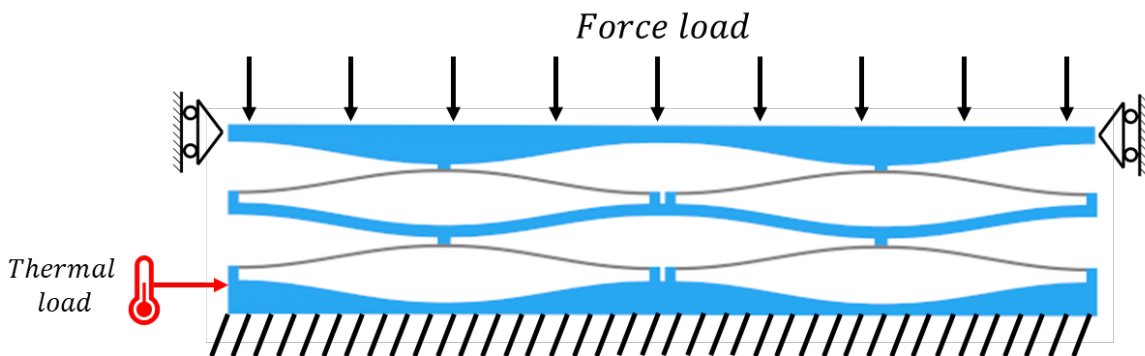


Figure 4.21: Constraints on 2x2 dome-shape structure with blue supports (active material) and grey beams (passive material). After a force load which deforms both layers, the bottom support is gradually heated to snap-back the bottom layer.

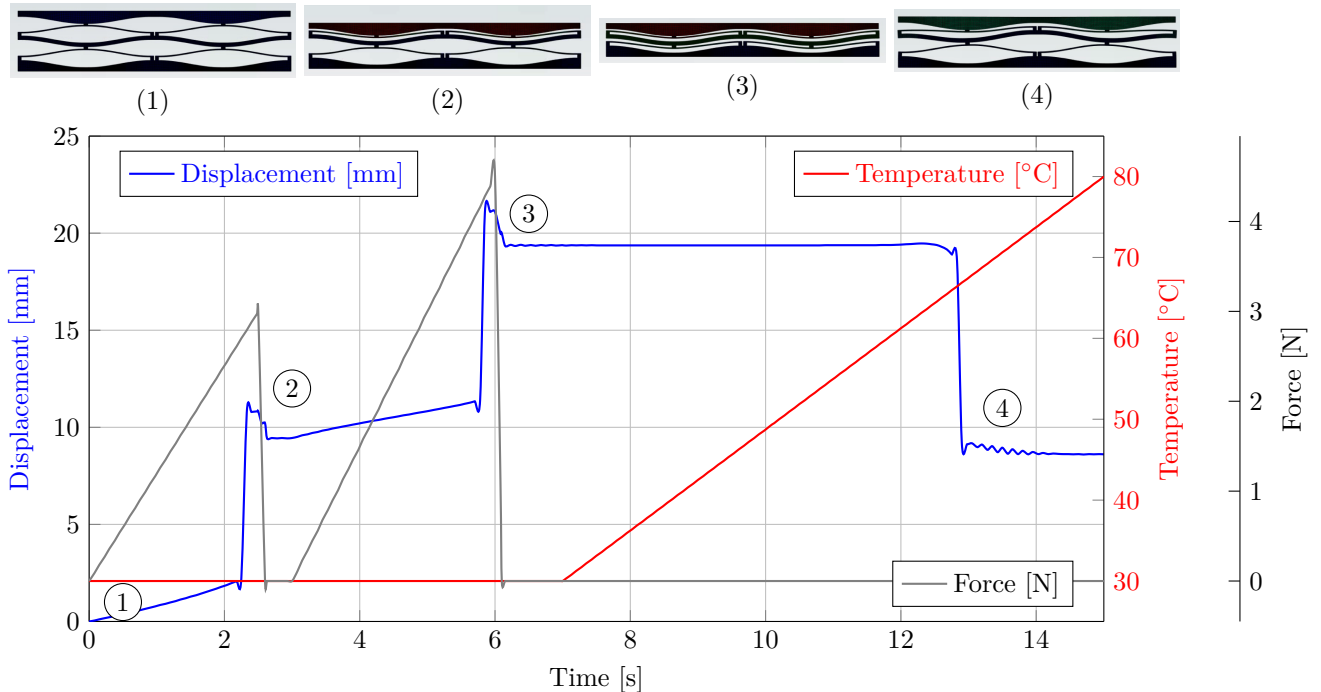


Figure 4.22: Plot of displacement, temperature, and force over time, with corresponding deformation images at key time points.

5

Experimental implementation

The experimental phase aimed to validate theoretical models through physical fabrication. However, transitioning from design to implementation introduced challenges related to material properties and heat application. These factors complicated the feasibility of the proposed programmability approach for the selected materials. This chapter discusses fabrication methods, material characterisation, and key experimental challenges, beginning with PolyJet printing, followed by fused filament fabrication. The findings and uncertainties are discussed in chapter 6.

5.1. PolyJet printing

PolyJet printing, developed by Stratasys, is an additive manufacturing technique that operates similarly to conventional inkjet printing. It uses multiple inkjet heads to dispense microscopic droplets of liquid photopolymer onto a build tray, which are then cured using ultraviolet (UV) light [64]. This process enables high-resolution multi-material printing, allowing for a minimum wall thickness of 1 mm, a layer resolution of 16 to 18 μm and an accuracy of 0.1–0.3 mm. A key advantage of PolyJet printing is its ability to simultaneously print multiple materials using digital materials (DM), which are composites formed by blending different photopolymers during printing. Previous research has investigated how the glass transition can be tuned with different combinations of digital materials [65]. The results of this study are presented in fig. 5.1. The multi-material printing allows for continuous transitions between rigid and flexible regions. However, material selection is limited to the photopolymers developed by Stratasys. Zhang et al. [49] made use of PolyJet-printed digital materials for their bi-stable unit cells. The Stratasys Connex 350 printer was used, employing the following DM:

- $m_1 = \text{RGD8530}$ (Primary: Vero White Plus + Secondary: Agilus Black)
- $m_2 = \text{FLX9895}$ (Primary: Agilus Black + Secondary: Vero White Plus)

In these compositions, Vero White Plus is the stiffer base material, while Agilus Black is a more elastic material. The exact formulation of these digital materials is not disclosed, but m_1 consists predominantly of Vero White Plus, while m_2 is primarily Agilus Black. For this study, a different PolyJet printer was used: the Stratasys MediJet J5. The selected digital materials were chosen for their expected similarity in properties to those used by Zhang et al.:

- $m_1 = \text{RGD8460}$ (Vero Black + Elastico Clear)
- $m_2 = \text{FLX95}$ (Vero Magenta + Elastico Clear)

Here, Vero Black serves as the stiffer component, while Elastico Clear provides elasticity, similar to the Agilus-based digital materials in previous studies. Zhang et al. [49] reported low transition temperatures (operating temperature $\sim 10^\circ\text{C}$, transition temperature $\sim 18^\circ\text{C}$). Additionally, their design relied on relatively wide supports ($\frac{w_s}{l} \approx 0.5$ at each end) to achieve bi-stability. This study aimed to address these challenges by introducing a multi-material support design. The intention was to increase the transition temperature to a more practical range for experimentation and maintain a compact design

by reducing support width. The digital materials were characterized through Dynamic Mechanical Analysis (DMA) which is detailed in the following section.

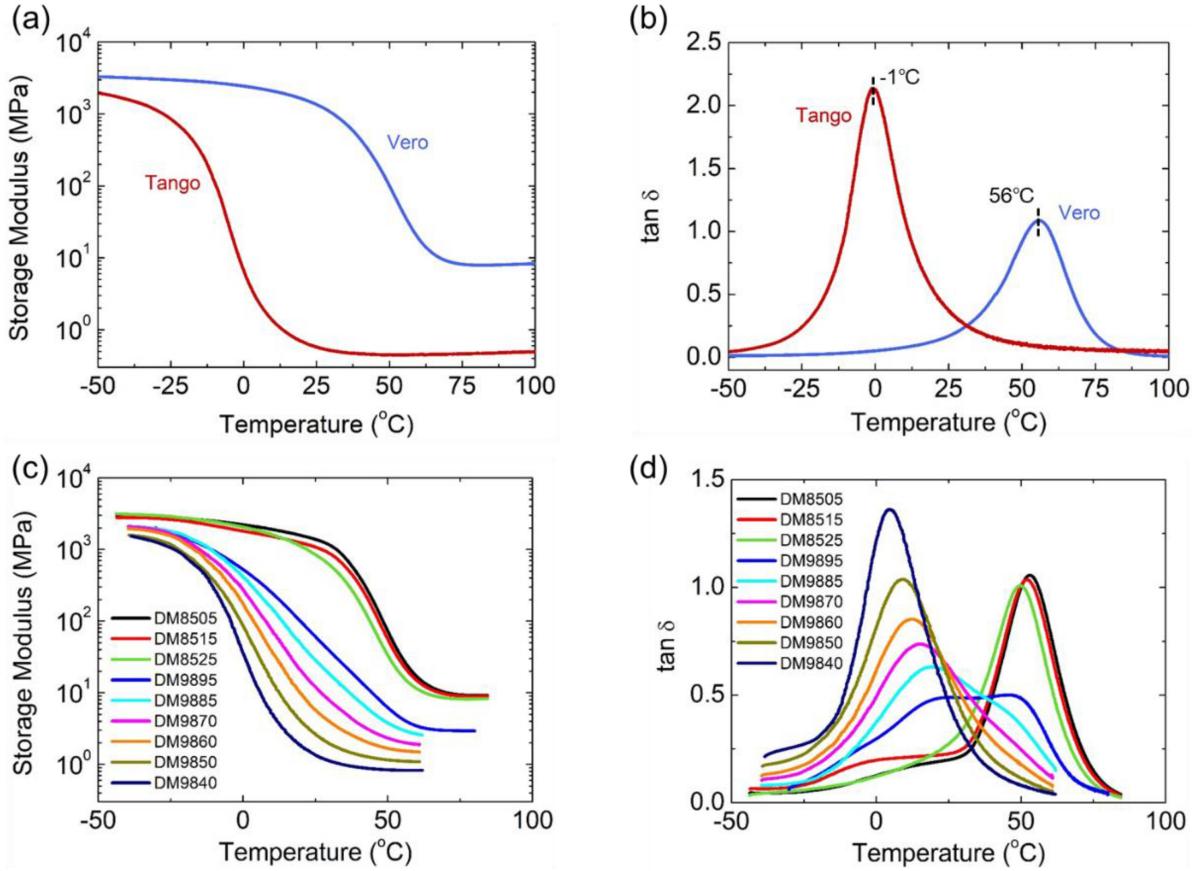


Figure 5.1: Thermomechanical properties of the base materials and commercially available digital materials for material jetting. a) Temperature-dependent storage modulus of Vero and Tango. b) Temperature-dependent $\tan \delta$ of Vero and Tango. c) Temperature-dependent storage modulus of nine commercially available digital materials. d) Temperature-dependent $\tan \delta$ of nine commercially available digital materials [65].

5.1.1. DMA PolyJet Materials

A Dynamic Mechanical Analysis (DMA) using a tension (film) clamp was conducted with the TA Instruments Q800. The conditions of the test were a constant strain of 0.03%, with a preload force of 0.01 N. Samples were equilibrated at -10°C for 10 minutes, followed by temperature ramp at $1^\circ\text{C}/\text{min}$ to 80°C for m_1 (and 60°C for m_2) at a frequency of 1 Hz. Three samples per material were tested, each with dimensions of $10 \text{ mm} \times 3 \text{ mm} \times 2 \text{ mm}$ (length \times width \times thickness). The samples were printed flat facing down in strips of 100 mm which were cut into the DMA sample sizes. The storage modulus from Zhang et al. are presented in table 5.1 in log scale alongside the values from this study.

Temperature (°C)	5	10	15	20	25	30	35	40	50
E1 Zhang (MPa)	2002	1859	1710	1538	1358	1174	983	769	n.a.
E2 Zhang (MPa)	526	378	264	171	105	60	35	20	n.a.
E1 Study (MPa)	2237	2078	1913	1717	1493	1249	1003	739	281
E2 Study (MPa)	1287	962	670	447	287	162	90	49	17

Table 5.1: Storage modulus E_1 and E_2 for Zhang et al. and this study at different temperatures

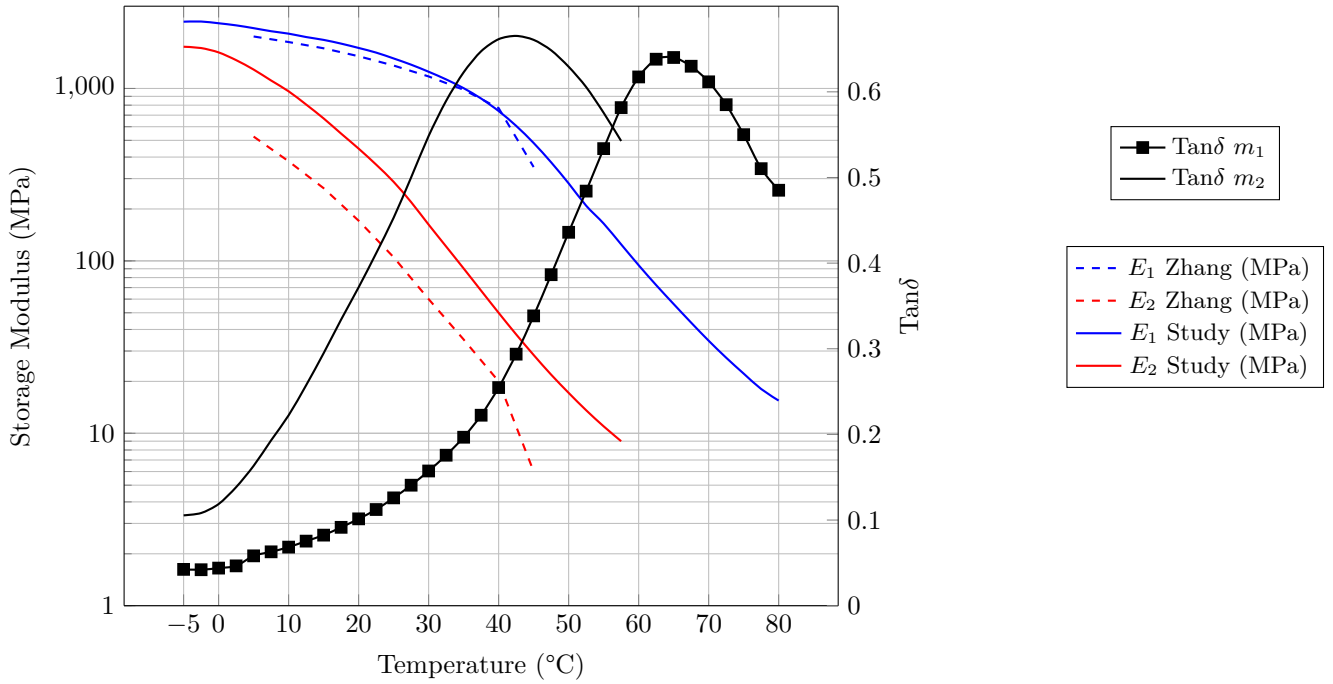


Figure 5.2: Storage modulus E_1 and E_2 from Zhang et al. and this study over temperature. The $\tan\delta$ is also plotted of this study

As shown in fig. 5.2, the rigid beam materials from both Zhang et al.'s work and this study display a comparable storage modulus values across the temperature range. However, the more flexible support material in this study exhibits significantly higher stiffness throughout. This difference is expected, as the base materials differ from those used in Zhang et al.'s study, and the DMA testing settings in their work were not specified. Conditions such as the frequency at which the materials are measured will have significant influence on the values. In addition to the storage modulus, the $\tan\delta$ of curves over temperature of this study are also presented, providing insight into the glass transition temperature of the materials. Based on the $\tan\delta$ peaks, it suggests the glass transitions are separated by approximately 20 °C. However, it is also noted that E_1 is already transitioning while E_2 is not beyond its glass transition temperature at approximately 42°C. This could cause the margin at which the transition temperature can take place to be tight.

5.1.2. Printed samples PolyJet

In order to create physical samples using PolyJet printing, multiple design iterations were made. The initial dimensions are listed in fig. 5.3 with the parameters displayed in fig. 5.4. These dimensions were selected based on the successful samples from Zhang et al. and theoretical expectations. To ensure optimal printing resolution in the beam thickness, samples were printed vertically with a layer height of $18\mu\text{m}$.

Dimension	Value [mm]
h	4.9
t	0.7
b	20
l	70
h_s	4.9
w_s	3
w_{sp}	1
h_{bp}	10

Figure 5.3: Dimensions for initial PolyJet physical samples

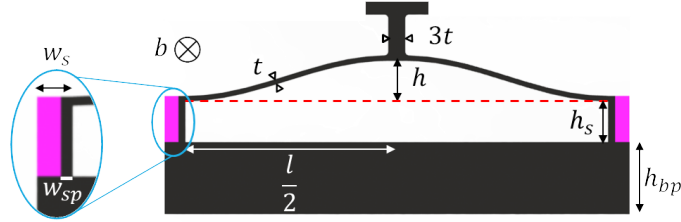


Figure 5.4: Parametric model of the unit cell design

A key requirement for the samples was achieving bi-stability at the operating temperature (20°C) and ensuring strong adhesion between the two materials. Consistent with previous literature, adhesion proved sufficient, as failure always occurred at stress concentration points within the beam rather than at the material interface (fig. 5.5a).

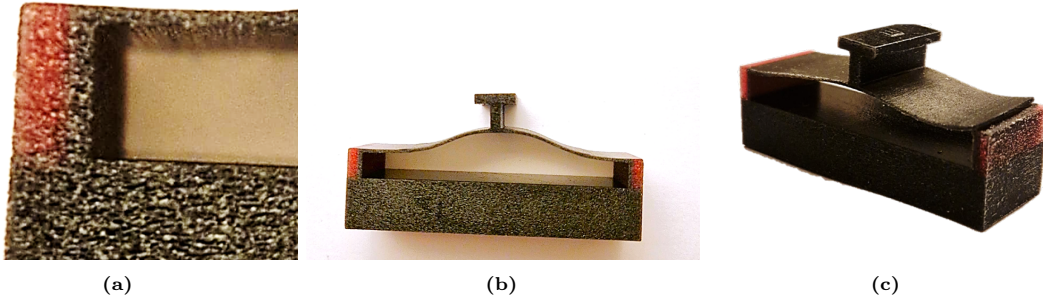


Figure 5.5: PolyJet initial sample results: (a) Close-up of the interface between the two materials of the PolyJet sample, (b) Initial printed sample front perspective, and (c) Breakage observed at the end of the beam.

Despite successful adhesion, the samples did not exhibit the desired bi-stable behaviour. Instead, a time-dependent response was observed, where the system gradually returned to its initial position after being deformed. The longer it remained compressed, the longer it took to snap back. This phenomenon, referred to as pseudo-bistability [66], arises from viscoelastic relaxation, a property not accounted for in the theoretical models, which assumed linear elasticity. Another contributing factor to the lack of bi-stability was potentially the unconstrained second buckling mode, which is addressed in more detail in chapter 6. Furthermore, the stresses in the system appeared to be exceeding the limits as the system failed at the stress concentrations as seen in fig. 5.5c. To mitigate these issues, design modifications were implemented to the thickness of the beam [30]. By introducing thickness modulation the stiffness of the beam was selectively reduced at critical stress points, creating hinge-like behaviour, which enhances bi-stability. The smooth variation in thickness was defined as:

$$t(x) = t_a \left[1 - \frac{\beta - 1}{\beta + 1} \cos \left(4\pi \frac{x}{l} \right) \right] \quad (5.1)$$

where t_a is the average beam thickness, and β represents the ratio of maximum to minimum thickness.

For this study, $t_a = 1$ mm and $\beta = 2.5$ were selected. A lower t_a or higher β would result in excessively thin features that would easily fracture. In addition, to prevent unintended contact between the beam and the bottom plate during deformation, a V-shaped groove was incorporated into the support structure. The refined design is shown in fig. 5.6.



Figure 5.6: Design of bi-stable beam with varying thickness to create hinge-like properties

Due to this design modulation, the second set of prints successfully achieved bi-stability. However, significant relaxation of the system was still observed. In an experimental setup with the adjusted design, the unit cell was loaded by a linear PI stage at a speed of 10 mm/s, equipped with a force sensor (see fig. 5.7). The results of this experiment are illustrated in fig. 5.8, which presents four loading and unloading cycles, with a relaxation period of two minutes between each cycle. This interval was necessary because, after unloading, the system in its original position exhibited a residual force of approximately -3 N. While resting in the initial position, the system first underwent rapid relaxation, indicated by an increase in the measured force from -3 N to 0.5 N, followed by a gradual decrease to zero over approximately two minutes. The comparison with the FEA results reveals notable differences. The FEA plot shows higher critical forces and no hysteresis. Despite achieving observable bi-stability in the printed sample, this behaviour was not reflected in the experimental measurements, as no negative forces were recorded during the loading step. It is likely that the system's relaxation occurred at such a rapid rate that, at the points negative forces were expected during buckling, the system had already partially relaxed, masking the characteristic force response associated with bi-stable behaviour.

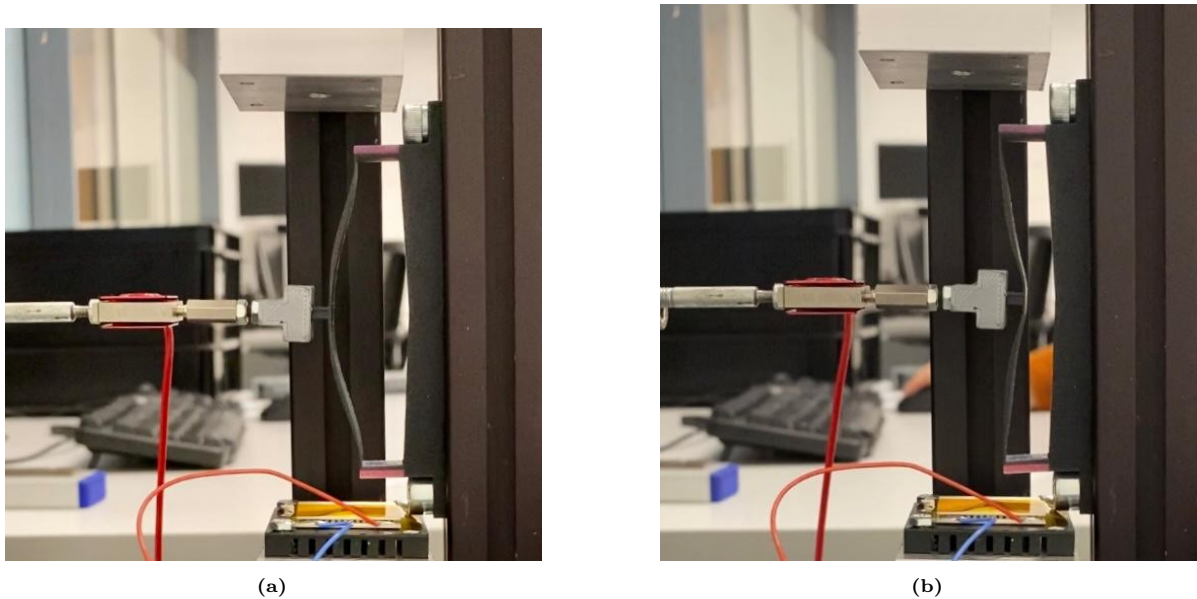


Figure 5.7: (a) Starting position of displacement loading the unit cell, showing the fixation of the bottom support and the attachment to the PI stage. (b) Closed position where the unit cell is displaced by twice its apex height.

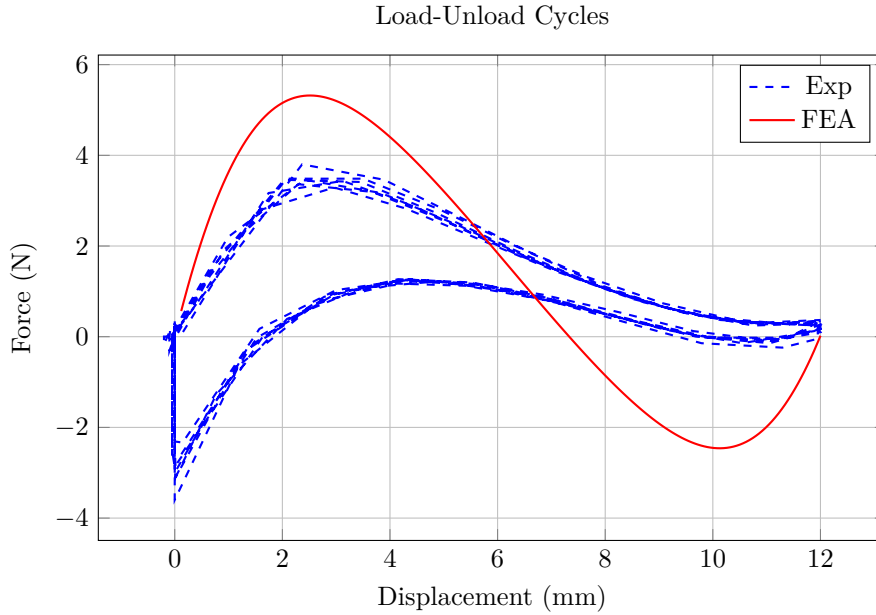


Figure 5.8: Plot of the experimental versus FE results for the force-displacement curve, showing significant hysteresis for the experimental unloading curve.

Finally, another challenge associated with this manufacturing technique was the limited lifetime of the printed samples. Although the samples initially exhibited viscoelastic behaviour on the day of printing, significant signs of ageing and brittleness became evident within a week, ultimately resulting in sample breakage under normal loading conditions. This required precise timing for performing tests. An improvement in the lifetime of the samples was found by storing the samples in a light-tight glass jar with water. However, the pronounced effects of visco-elasticity and ageing were deemed too dominant to experimentally verify the theoretical models. This led to the adoption of an alternative manufacturing technique, fused filament fabrication.

5.2. Fused Filament Fabrication

Fused Filament Fabrication (FFF) is a well-established extrusion-based printing technique, where objects are constructed by depositing melted material through a nozzle layer by layer. Compared to the PolyJet printing technique, FFF offers greater flexibility in adjusting printer settings. The printer used in this study, the Prusa Original MK3S, has a minimum layer thickness of 0.1 mm and a nozzle size of 0.4 mm, which offers a significantly lower resolution compared to the MediJet J5. An additional limitation of FFF is the lack of multi-material printing capability. Although this can be achievable in FFF, extensive iteration is required to ensure sufficient interlayer adhesion [67]. To address this challenge, a bonding approach inspired by Niknam et al. was adopted, using Loctite Super Glue-3 to join the two materials. The selected materials were Poly(lactic acid) (PLA) as the active material and Poly(ethylene terephthalate) glycol (PETG) as the passive beam material. This selection was based on availability and expected sufficiently distinct storage moduli [68, 69]. Both PLA and PETG have been previously employed in combination with thermoplastic polyurethane (TPU) to create thermally programmable bi-stable unit cells, with TPU serving as the passive material and PLA and PETG functioning as active components [36, 51]. However, no existing literature has reported on bi-stable systems utilizing PETG as the beam material and PLA as the active material.

5.2.1. DMA FFF Materials

A Dynamic Mechanical Analysis (DMA) using a tension (film) clamp was conducted with the TA Instruments Q800. The conditions of the test were a constant amplitude of $20\mu m$, with a preload force of 0.01 N. Samples were equilibrated at $-10^{\circ}C$ for 10 minutes, followed by temperature ramp at $1^{\circ}C/min$ to $80^{\circ}C$ for m_1 (and $60^{\circ}C$ for m_2) at a frequency of 1 Hz. Three samples per material were

tested, each with dimensions of 10 mm × 3 mm × 2 mm (length × width × thickness). The printing orientation corresponds to the orientation of the bi-stable samples. The printing settings are presented in table 5.2.

Table 5.2: Printing Settings for PETG and PLA DMA Samples

Parameter	Value
General Printing settings	
Infill Density	100%
Layer height	0.1 mm
Nozzle size	0.4 mm
Printing Orientation	Printed on long edge
PETG Printing Conditions	
Nozzle Temperature	240°C
Bed Temperature	90°C
PLA Printing Conditions	
Nozzle Temperature	215°C
Bed Temperature	65°C

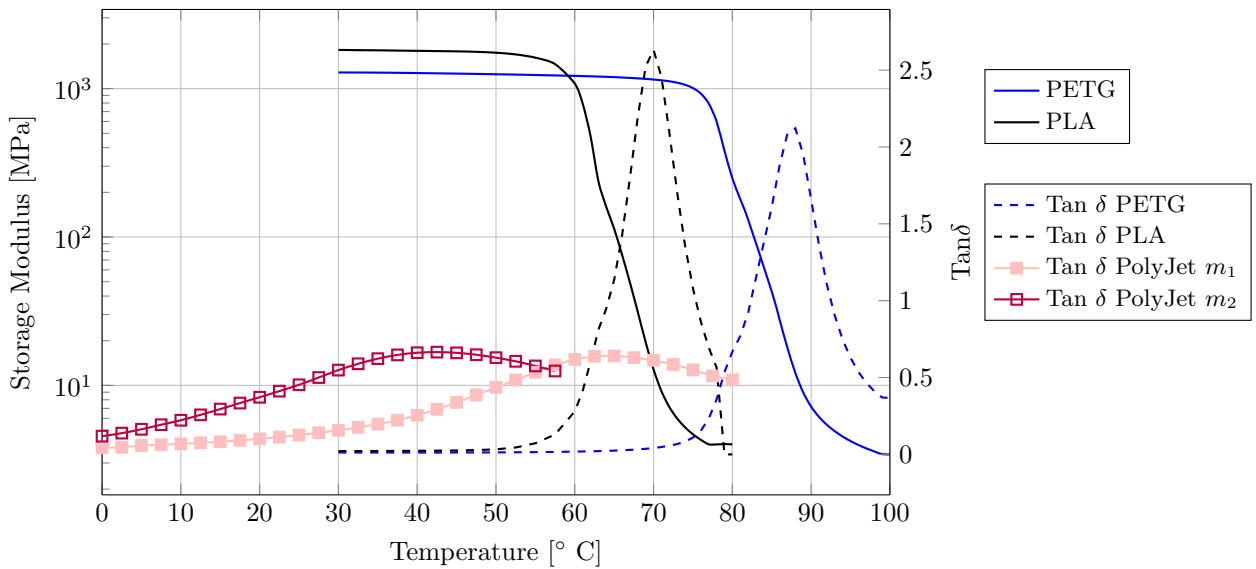


Figure 5.9: DMA results for PETG and PLA 3D printed samples showing the storage modulus and $\tan \delta$ over a temperature range. The $\tan \delta$ of the PolyJet materials are also plotted for comparison.

The DMA results for the FFF materials indicate a clear difference in T_g , with PLA exhibiting a T_g of approximately 70°C and PETG around 88°C. These values align well with literature on 3D-printed PETG and PLA, though variations in filament composition, printer settings, and DMA conditions may cause slight deviations [68, 69]. The first observation which can be made is that the $\tan \delta$ peaks of the FFF materials are much more pronounced than the PolyJet materials. By plotting both materials on the same graph, the effect of the heterogeneity of the PolyJet materials is demonstrated as the spread out peaks correspond to the presence of two storage moduli. This corresponds to the findings in fig. 5.1, whereby the DM9895 has a spread out peak compared to the more homogenous digital materials. The sharper transition, over a small temperature range observed in the FFF materials could be more suitable for rapid activation in this programming approach. However, the FFF materials demonstrate a relatively high peak $\tan \delta$ (approximately 2 to 2.5 for both), which indicates an increase in material damping and viscosity. This may interfere with the effectiveness of the programming approach.

5.2.2. Printed samples FFF

For the FFF samples, multiple iterations were made to create a bi-stable system. This proved to be challenging with the main issues stemming from the unconstrained 2nd buckling mode and the stress limits of the materials. Through experimentation it became clear the an unconstrained 2nd mode severely influences the bi-stability of the system. Despite literature stating that with a sufficiently large ratio Q , of 5.65, the system will be bi-stable even with an unconstrained 2nd mode, this was not found to be the case with the samples made of PETG beams [25]. For further investigation, a sample was created with a steel strip (0.07 mm) which did show bi-stability with an unconstrained 2nd mode (fig. 5.10). However, in that sample, the Q ratio was roughly 140 ($Q = \frac{10}{0.07}$), which was unattainable for these polymers in combination with the fabrication technique used.



Figure 5.10: Prototype of metal beam with PLA supports.

The stress limits of the system were observed in two distinct ways. Firstly, prints that were not initially bi-stable, could become bi-stable after more than 100 cycles of loading and unloading. This transformation was likely due to plastic deformation at stress concentrations, which locally reduced stiffness and effectively created hinge-like regions. The second effect observed was material yielding and failure at stress concentrations. To address these issues, the beam topology was modified. Inspired by existing literature on tuning the snap-through behaviour of bi-stable beams, different topologies were explored to improve performance [70, 71]. The designs of successful (bi-stable) iterations are presented in fig. 5.11. Here it can be seen that again, similarly to the adjustment of the PolyJet samples, hinge-like regions are created. In this case, by removing material at the stress concentrations. With the bi-stable samples, the programming approach using thermal stimuli could be applied, which is described in the following section.

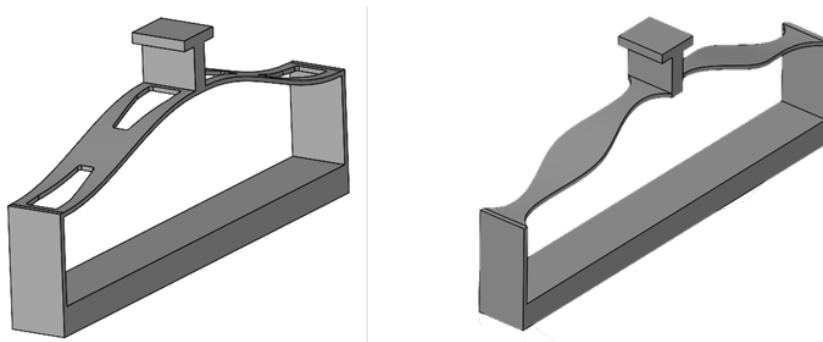


Figure 5.11: Variation of topology of the PETG designs resulting in hinge-like properties.

5.3. Heat application

To evaluate the thermal programming approach, a series of heating tests were conducted on FFF samples exhibiting bi-stability at room temperature. Various heat application methods, including water submersion, heat gun exposure, and local heating via Peltier elements, were tested to observe their effect on snap-back behaviour. The goal was to evaluate whether bi-stable snap-back occurred at the predicted transition temperature of approximately 60°C. From observations, the experimental results did not align with the theoretical expectations. A summary of the test conditions and observations is provided in table 5.3.

Heating Method	Temp. (°C)	Sample Type	Expected transition temperature	Observations
Water Submersion	40	Multi-material	60°	Snap-back consistently occurred within seconds.
	20	Multi-material	No snap-back expected	Occasional, inconsistent snap-back observed.
	40	Mono-material	No snap-back expected	No snap-back observed.
Heat Gun	50	Multi-material (clamped)	60°C	Snap-back consistently occurred.
	50	Mono-material (clamped)	No snap-back expected	No snap-back observed.
Peltier Elements	30 to 60	Multi-material (clamped)	60°C	No snap-back observed.

Table 5.3: Summary of heat application tests, expectations, and observations.

Water submersion tests involved placing samples in a heated water bath at either 40°C or 20°C after manually deforming them into their second stable state. The primary objective was to observe whether snap-back occurred and at what temperature. A control sample made of a single material was also tested at 40°C to determine whether snap-back was unique to the multi-material design.

Heat gun tests were conducted by exposing a clamped sample to 50°C heated air, with the heat applied to the supports and beam. This dry heating method removed the potential effects of water interaction, providing a closer step towards heating by radiation. It also introduced more restrictive boundary conditions by clamping the bottom plate. A limitation of this method is the uncontrolled heating application (non-uniform).

Peltier heating tests involved placing a fixed sample between two Peltier elements heated at temperatures from 30 to 60° C. A small gap was maintained to ensure that heat transfer primarily occurred through radiation. Unlike the previous methods, this setup specifically targeted the boundary supports to evaluate whether local heating could induce snap-back.

During testing in water at 40 °C, snap-back behaviour was observed at a temperature approximately 20 °C lower than predicted by both the analytical and FE models. This suggests that additional factors influenced the observed transitions. The most probable contributing factors include:

- The bi-stable cells were marginally bi-stable, meaning they required minimal disturbance to transition back to their preferred state.
- The second buckling mode of the samples was unconstrained, while this mode was constrained in the models.
- The boundary conditions of the physical samples were less restrictive than in the models.

With a marginally bi-stable system in combination with an unconstrained second buckling mode, the energy threshold is very low. This means a lower change in stiffness of the supports would be required to snap-back. Additionally, it is also likely that any small disturbance could trigger a snap-back. Furthermore, the system's bottom plate was not fixed to anything while being submerged in water which may have also contributed to less restrictive boundary conditions compared to the models, allowing for earlier snap-back behaviour. The heat gun samples also snapped back earlier than the water heated samples. These samples had more restrictive boundary conditions as their bottom plate was fixed. Still, they displayed snap-back behaviour consistently at a lower temperature than the expected theoretical transition temperature. Again, this may be attributed to the marginal stability in the deformed position requiring very little disturbance for the system to snap-back. The mono-material samples did not display snap-back behaviour. Upon observation, the mono-material samples seemed to be less responsive to small disturbances in general. This was potentially related to the increased integrity of the supports compared to the adhered ones of the multi-material supports, which could have provided more stability.

Considering these factors, an uncertainty remains regarding why the multi-material samples did not snap back at the same temperature under local heating of the Peltier elements. The Peltier elements were heated to 50 °C, and the sample was fixed between them, allowing sufficient space for the supports to bend while being close enough to absorb heat through radiation. A thermal image captured using a FLIR infrared camera is shown in fig. 5.12.

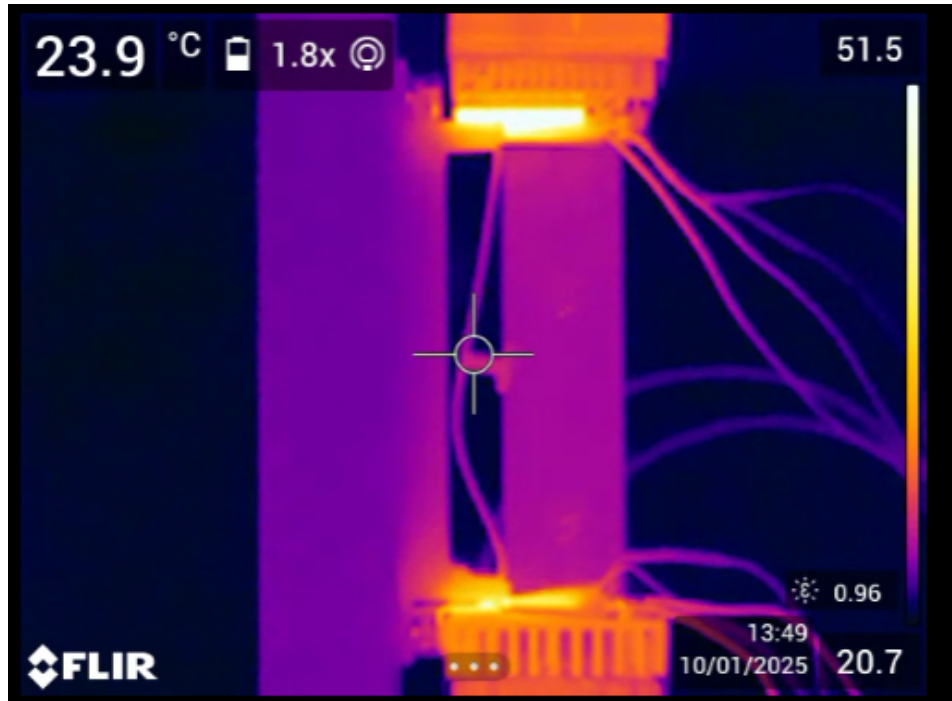


Figure 5.12: Infrared camera image of Peltier heating set up. The boundaries are heating up due to the radiation indicated by their change in colour.

Despite the image's low resolution, it is evident that the supports absorbed the heat successfully. However, even after multiple tests under prolonged heating (> 10 min), the system did not snap back. To assess whether the fixed boundary conditions were preventing the system from transitioning, the sample was manually held between the Peltier elements to eliminate any potential constraint. Despite this adjustment, no snap-back was observed. A primary difference between the water and the heat gun test compared to the Peltier elements were that in the former two, the entire beam or part of it was also subjected to heating. In theory, simultaneous softening of both the beam and the supports should counteract the snap-back response, as a sufficiently large relative stiffness between the beam and the supports (E_1/E_2) is required for the supports to bend effectively. Given that the beam was only marginally bi-stable and the second mode was not constrained, interactions with water or air flow from the heat gun may have facilitated slight beam rotation, influencing the observed behaviour.

6

Discussion

In this chapter the remaining uncertainties of the results are discussed. First, the factors contributing to the differences between physical and theoretical results are analysed. Secondly, the unaccounted for thermo-mechanical properties of polymers which potentially interfere with the approach are also addressed. Lastly, a refined flowchart reflecting the design choices for this programming approach is presented. This flowchart integrates the new findings from this study which improve the understanding of the programming approach and specifically what choices restrict its functionality.

6.1. Influence of testing conditions

In literature, multiple studies successfully demonstrated the working principle of thermal softening for programming bi- to mono-stability [36, 37]. This study introduced the less common aspects of using glass-state beams and the application of localized heating. Through analytical and numerical modelling, the design showed promising results. However, challenges arose during the experimental phase in realising bi-stability. One factor that was not initially considered is that most existing studies tested their physical samples either in a layer or an array, rather than as a single unit cell, which effectively constrains the second buckling mode. During physical implementation of the design, it became evident that the constraint of the second mode plays a crucial role in achieving bi-stable behaviour. In an isolated single beam unit cell, this mode will not be constrained. To illustrate the influence of this constraint, a model was simulated using FEA. The different force-displacement curves are presented in fig. 6.1.

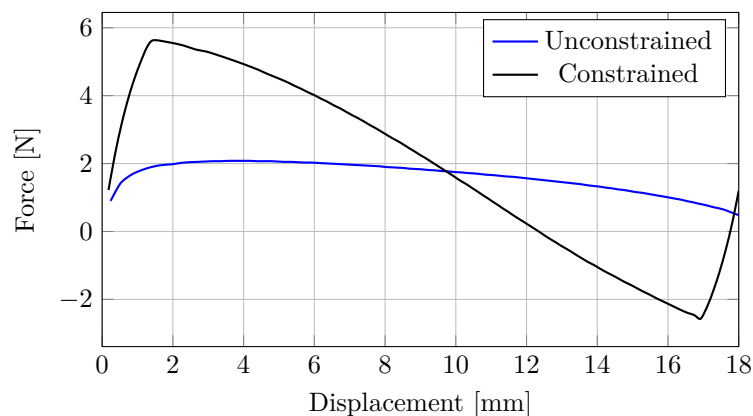


Figure 6.1: Force vs. displacement for unconstrained and constrained second mode.

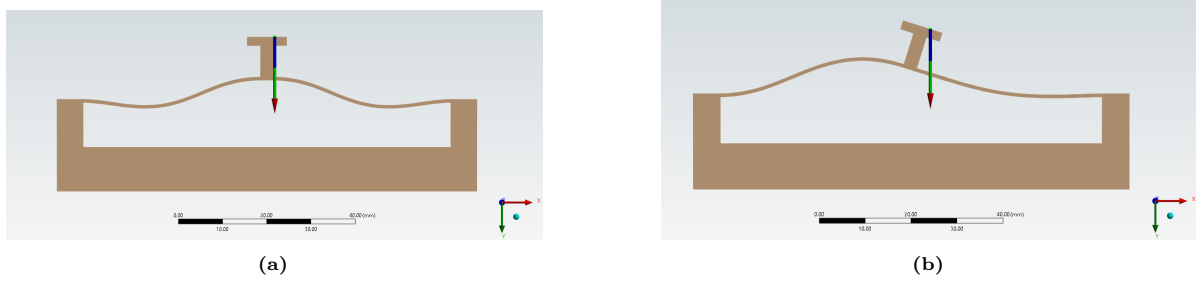


Figure 6.2: Snapshots of the FE model: (a) 2^{nd} mode constrained, showing the 3^{rd} buckling mode shape. (b) 2^{nd} mode unconstrained, showing the 2^{nd} buckling mode shape.

The results, shown in fig. 6.1, highlight the significant difference in force-displacement behaviour between constrained and unconstrained systems. Not only are the critical forces significantly lower in the unconstrained system, but it also fails to achieve bi-stability altogether. The difference in buckling mode shapes is illustrated in fig. 6.2, where fig. 6.2a shows the third buckling mode shape of the constrained system, while fig. 6.2b depicts the asymmetric second buckling mode shape of the unconstrained system. As stated the samples made with the FFF printer were not bi-stable straight from the printer and were manipulated to become bi-stable after many numerous cycles of loading and unloading. The bi-stability in these instances most likely stemmed from local plastic deformation at stress concentrations and therefore caused the system to be slightly bi-stable even though the second mode was not constrained. The result was a marginally bi-stable system which required very little disturbance to snap-back from a deformed position. To experimentally verify the impact of second-mode constraints, force-displacement measurements were conducted under three distinct loading conditions. The samples used were all marginally bi-stable. The experimental conditions are shown in fig. 6.3:

1. Constrained loading: The beam's rotation is restricted and is held in place throughout deformation with an attachment to the PI stage.
2. Unconstrained loading: The beam is allowed to deform freely by replacing the attachment with a bearing to allow for rotation of the beam.
3. Unconstrained with magnetic attachment: A magnet is attached to the top of the beam so that negative forces can be measured.

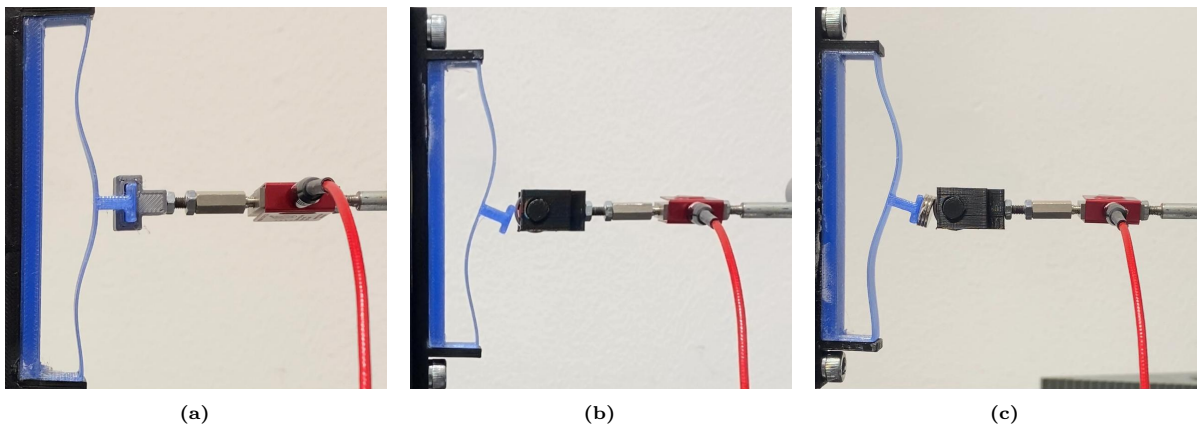


Figure 6.3: Experimental setups for force-displacement measurements. (a) Constrained loading, (b) Unconstrained loading, and (c) Unconstrained loading with magnetic attachment. These images serve as examples of the loading constraints and are not all the same sample.

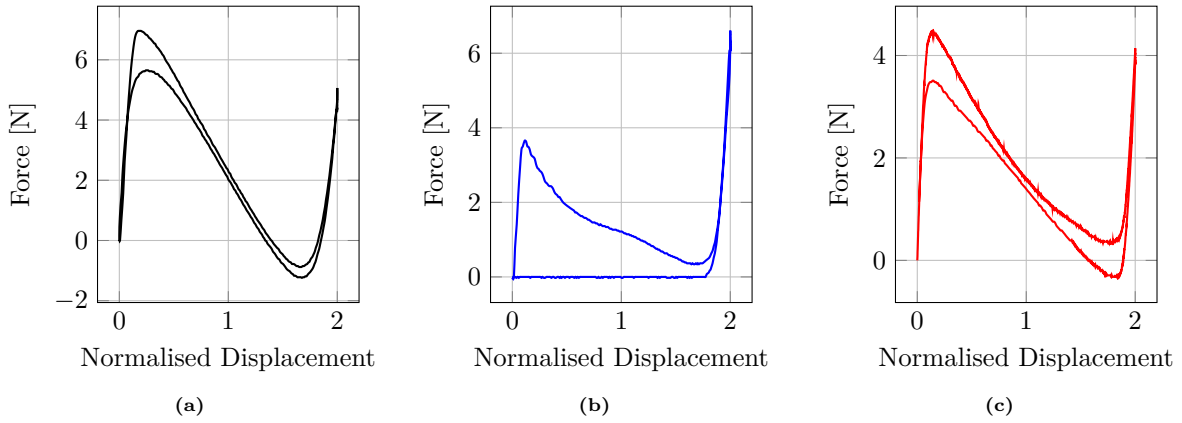


Figure 6.4: Force vs. displacement results for constrained and unconstrained loading. (a) Constrained force-displacement behaviour, (b) Unconstrained force-displacement behaviour, (c) Unconstrained force-displacement with magnet.

First it is observed that the buckling mode shapes in fig. 6.3 correspond to the results from the FEA simulation in ???. The constrained beam exhibits a distinct third buckling mode, whereas the two unconstrained configurations undergo an asymmetric second buckling mode. The corresponding force-displacement results for these three conditions on the same sample are shown in fig. 6.4. The constrained system requires significantly higher critical forces and exhibits bi-stability during both loading and unloading indicated by the negative forces upon loading and unloading. In contrast, the two unconstrained systems experience much lower forces, and neither system exhibits negative forces during loading. In the unconstrained system shown in fig. 6.3b, the force returns to zero, indicating that the beam remains in its deformed position. In the unconstrained system with the magnetic attachment, it might be expected that negative forces would be recorded during loading. However, this only occurs during unloading. A possible explanation is that the slope of the second buckling mode is very shallow, causing it to only cross the x-axis at the final stage of displacement. At this point, the negative force may be too small to be detected. If the beam is pushed beyond this point, it transitions to its first buckling mode, as indicated by the positive force curve at the end. Once it reaches this state, it becomes stable, and the negative energy is registered only upon unloading. These tests demonstrate the effect on the force-displacement curve, showing the significant influence of constraining the second mode both for the maximum critical force and the negative minimum critical force.

6.2. Influence of material properties

As was indicated in section 5.2, the samples did not transition at the theoretically determined transition temperature. If the samples had transitioned at the expected temperature, additional challenges would have arisen. One key issue is the temperature dependence of the yield strength in polymer materials [72]. When an FFF-printed model was tested in water at an elevated temperature of 60 °C, both the beam and the supports exhibited plastic deformation while in the second stable state. Notably, the PETG beam deformed despite being approximately 20 °C below its glass transition temperature (T_g). This behaviour is likely attributed to the reduction in yield strength at higher temperatures, which occurs even before the material reaches its T_g [73]. The effect of temperature on the yield strength of 3D-printed PETG was investigated by Vaňková et al., and their experimental results are presented in fig. 6.5.

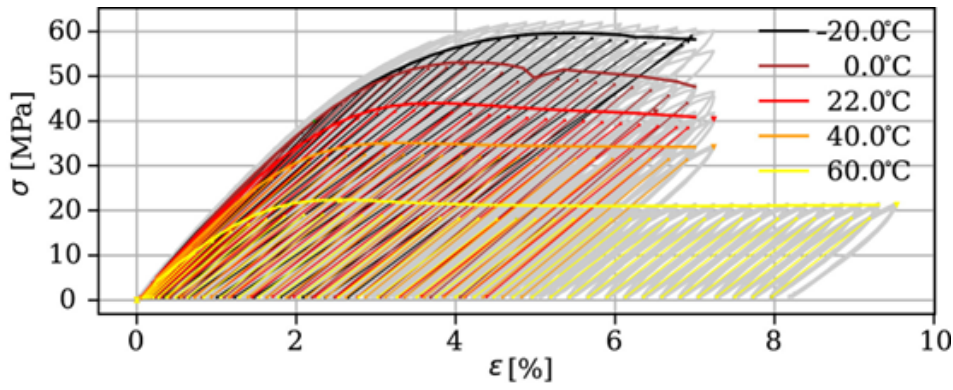


Figure 6.5: Averaged values determined from cyclic tension tests for 3D printed PETG samples at different temperatures [73]

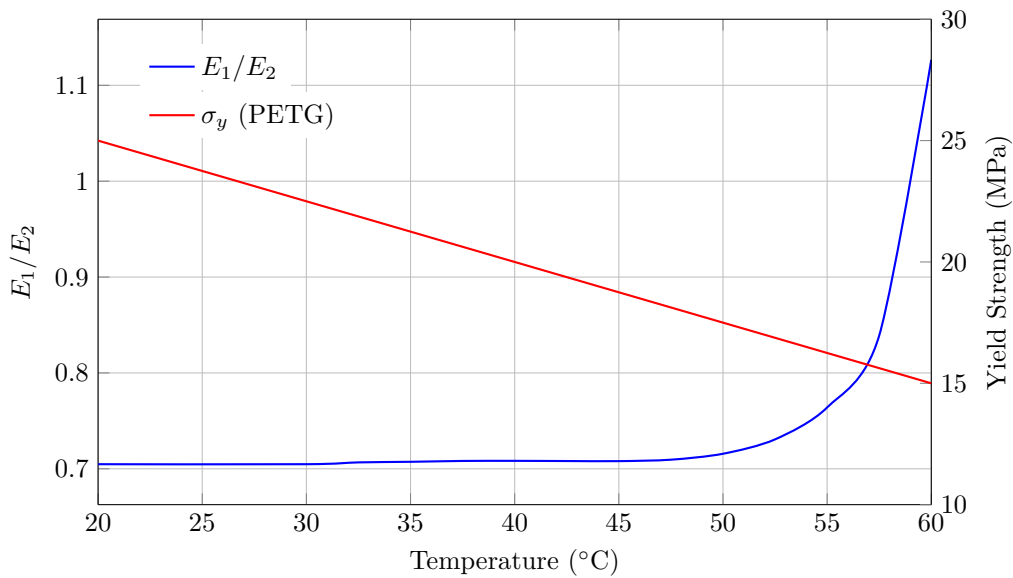


Figure 6.6: Comparison of E_1/E_2 and Yield Strength of PETG vs Temperature

The change in yield strength of PETG is extracted from fig. 6.5. These values are plotted against temperature and compared to the change in relative storage modulus with PLA (E_1/E_2) to see how the two rates compare, in fig. 6.6. This gives an indication of the narrow margin at which the system can reach a transition temperature, limited by the yield strength of the beam decreasing. For example, if a beam of certain dimensions experiences a stress of 20 MPa, and the calculated transition temperature is 60°C, the beam will most likely start to plastically deform preventing a snap-back. This demonstrates that even if the samples made of PETG and PLA would transition at the theoretically determined temperatures, the snap-back behaviour would be restricted. Therefore, an important finding for this programming approach is that materials with more spread-out storage moduli could provide a larger design space. Additionally, it may be worth considering a beam material that is not a polymer to fully investigate the working principle of the support softening.

Choosing a suitable combination of materials for this programming approach proved to be challenging during the experimentation phase. Aside from the unaccounted for the temperature dependent yield strength, we can also observe the role of the ratio E_1/E_2 and the choice of operating temperatures. To do this, we compare the passive (E_1) and active (E_2) moduli for both fabrication methods against temperature, where the effect on relative stiffness can be seen more clearly (fig. 6.7). It can be seen that the PolyJet materials undergo a much smaller change in relative stiffness compared to the FFF materials, with a maximum ratio of $E_1/E_2 \approx 17$ and ≈ 215 , respectively. Considering that the intended

operating temperature of the PolyJet materials was room temperature (21°C), at this point, the ratio is already increasing compared to the steady value of $E_1/E_2 \approx 0.7$ for the FFF materials at the same temperature.

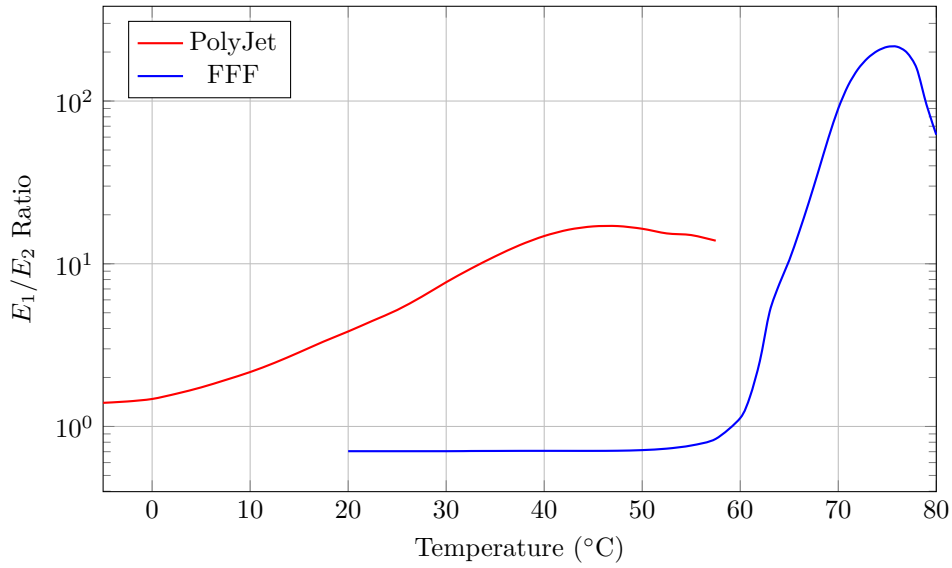


Figure 6.7: Comparison of relative stiffness ratio E_1/E_2 for PolyJet and FFF materials as a function of temperature.

This may explain why the PolyJet samples performed successfully at a lower operating temperature of around 10°C in the literature [22]. Starting at room temperature provides only a narrow window before reaching the maximum E_1/E_2 ratio, limiting the effectiveness of thermal softening. Additionally, the relatively weak variation in E_1/E_2 further complicates achieving a distinct transition, making these materials less suitable for thermal softening as a programming approach. Conversely, the FFF materials exhibit a much broader range in relative stiffness, as indicated by the variation of E_1/E_2 over temperature. However, their suitability is constrained by a relatively low yield strength of the beam material near the transition temperature, which restricts the available design space. This suggests that these materials may also be suboptimal for thermal softening as a programming approach.

6.3. Refined flow chart of programming approach

With insights gained from experimental implementation, the flowchart for the programming approach, outlining the key decisions in achieving bi- to mono-stable tuning, has been refined (see fig. 6.8).

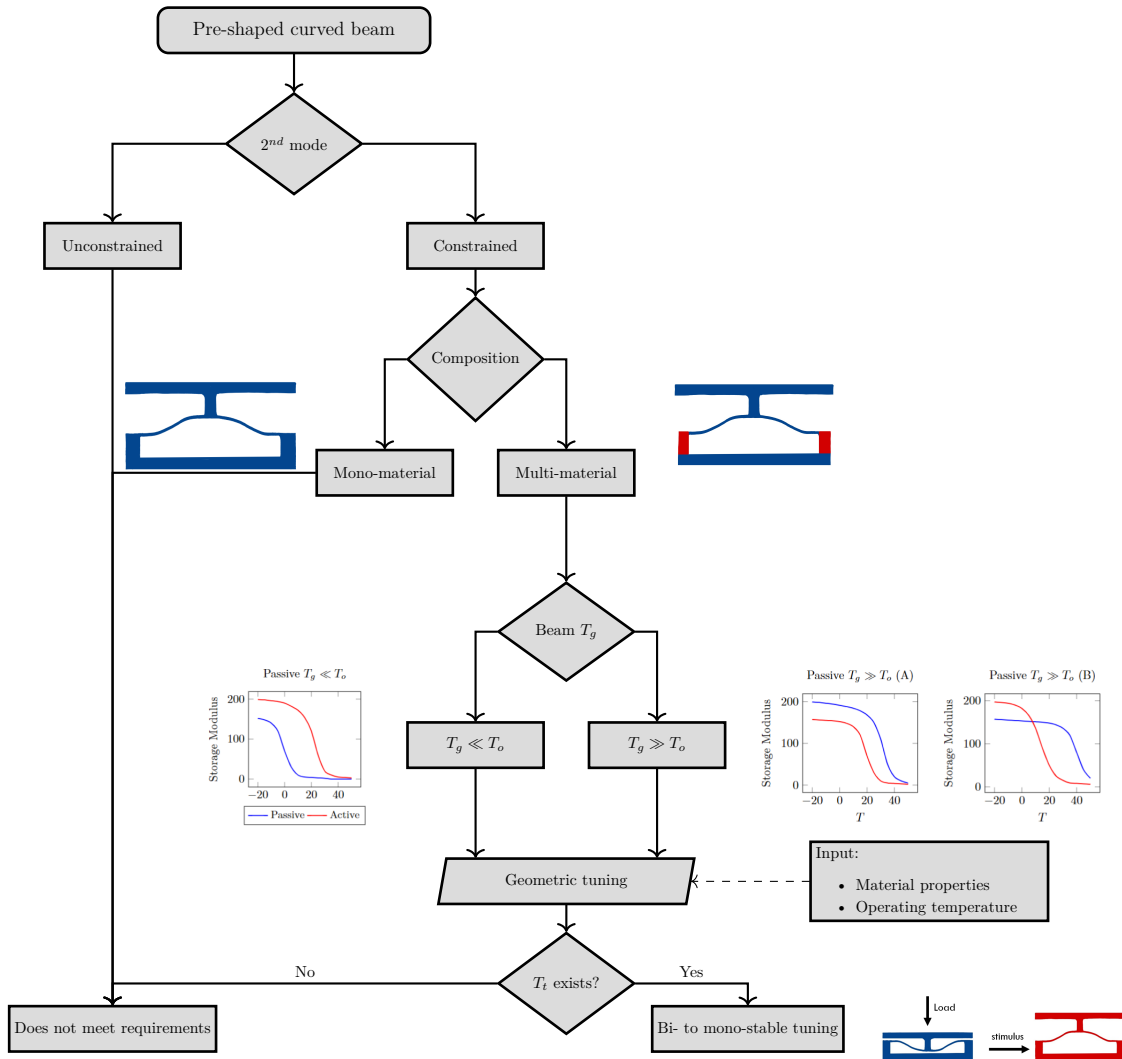


Figure 6.8: Refined flowchart of thermal softening as a programming approach for asymmetrically bi-stable beams.

This refined version emphasises the critical requirements for successful tuning of bi to mono-stability. The geometric deformation tuning is left out of this flowchart to focus on the main goal of this programming approach. The first key distinction is made at the initial stage, where instead of assuming that a pre-shaped curved beam is inherently bi-stable, the flowchart now explicitly considers whether the second buckling mode is constrained. This is an important clarification, as existing literature on mechanical metamaterials with bi-stable unit cells in metamaterials often overlooks this detail. A reason for this may be that in tessellated structures, the arrangement itself typically constrains the second mode automatically. However, in isolated unit cells, this is not necessarily the case, which can lead to unexpected issues in experimentation as was observed in this study. One method to constrain the second mode in a unit cell is with a parallel beam configuration, see fig. 6.9. This configuration refers to employing two parallel beams which are connected at their centres. The longer the center clamp or the gap between the two beams, the more the second mode can be overcome [30]. The additional beam constrains both beams from rotating into the second buckling mode, ensuring bi-stability.

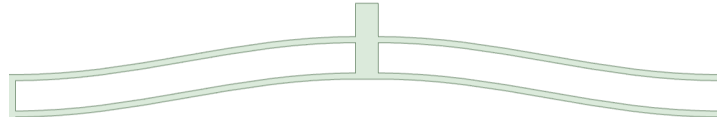


Figure 6.9: Representation of a parallel beam configuration

The second decision point, which is well established in literature, concerns whether the system is composed of a mono-material or a multi-material structure. This distinction determines whether a relative stiffness change between the beam and its support can occur, which is crucial for leveraging the thermal softening for a transition. Therefore, a mono-material does not meet the requirements for this programming approach. The third decision is related to the beam material selection. Depending on whether the beam is in its rubber (flexible) state or a glass-like (rigid) state during operation, three different storage modulus combinations can be achieved. The analytical model showed that this selection plays a significant role in geometric tuning of the transition temperature for multi-material supports. Two general observations were:

- If the beam is in a rubber-like state, increasing the proportion of passive material in the support lowers the transition temperature.
- If the beam is in a glass-like state, increasing the proportion of passive material in the support raises the transition temperature.

Furthermore, several key material properties, previously not explicitly identified in literature, have now been established as crucial for practical realization of the system. These include:

- The decrease in yield strength of constituent materials with increasing temperature, which will limit the design in terms of allowable stresses.
- The viscoelastic behaviour, especially near the glass transition temperature, which may either prevent snap-back behaviour or cause relaxation over time, reducing the effectiveness of the system.
- The spread of glass transition temperatures between the beam and the support. If they are too close together, the system may behave more like a mono-material, even if the absolute magnitudes of their storage moduli differ. This is because the relative stiffness may only change in a limited temperature range.

Ultimately, the three key design choices, (1) second mode constraint, (2) composition (mono vs. multi-material), and (3) material selection, will determine whether bi- to mono-stability can be achieved through thermal softening of the boundary conditions. Further limitations such as fabrication methods will most likely have an influence as well, but this would require more investigation.

7

Conclusion

This thesis investigated the feasibility of achieving local one-directional programmability in multi-stable mechanical metamaterials through thermally activated stiffness modulation of the boundary conditions. The findings contribute to the broader understanding of programmable multi-stable mechanical metamaterials and highlight the challenges associated with thermal softening as a programming approach.

A conceptual framework was first established to explore different actuation mechanisms for local one-directional programmability in bi-stable beams. This framework provided a systematic overview of existing and novel approaches based on relevant literature. Following an evaluation, localized thermal softening was identified as the most effective strategy for programming transitions between stable states. This decision was based on its expected ease of implementation, potential adaptability to 3-dimensional configurations, and prior success in recent literature.

From this, a novel multi-material unit cell design was developed, utilizing temperature-dependent stiffness modulation at the boundary conditions to induce a transition from bi-stability to mono-stability. This approach leveraged the drastic change in storage modulus, an inherent property of amorphous polymers when heated. The use of localized heating increased the system's level of addressability compared to existing methods. Furthermore, employing beams in their glass state allowed for an investigation into the applicability of this programming approach for structures utilizing PEEK as a beam material. This decision was related to the potential applications of mechanical metamaterials in precision motion systems whereby PEEK could be a suitable base-material.

An adapted analytical model was developed in chapter 4 to describe the force-displacement behaviour of bi-stable curved beams with temperature-dependent boundary conditions. This model builds on prior research on fixed boundary conditions by incorporating variable stiffness effects at the supports. Through this model, new stability thresholds were established, providing insight into the geometric relationships and their influence on bi-stability. Key differences in tuning for a certain transition temperature were identified between a system with a rubber-state beam versus a glass-state beam, confirming the observations from previous literature [36]. To verify the analytical findings, an FE model was developed. Although general agreement in trends and magnitude was found, it was determined that taking into account higher buckling modes in the analytical model could increase its accuracy. Additionally, the FE model facilitated the analysis of more complex structures and time-dependent loading conditions. The models showed promising results for achieving local one-directional programmability in multi-stable mechanical metamaterials.

Fabrication of physical samples to test the theoretical design revealed several challenges and sensitivities. Different manufacturing techniques were considered based on existing literature, with PolyJet printing initially being selected due to its multi-material printing capability, relatively high printing resolution, and tunable stiffness properties. Material characterization using DMA revealed two distinct storage moduli. However, the samples exhibited significant visco-elasticity interfering with the programming approach due to rapid relaxation. In prior research, this factor was not explicitly identified

as a potential limitation of thermal softening as a programming method. Attempts to minimise this relaxation effect relied on design adjustments, which reduced but did not eliminate the issue.

Consequently, a second fabrication method, fused filament fabrication, was employed using PLA and PETG as materials for the supports and beam respectively. With these new samples, the importance of constraining the second buckling mode was confirmed through experimental testing and FE simulations. It highlighted a fundamental limitation of testing single-beam unit cells, rather than in a layer or array structure. A unit cell with a parallel beam configuration, could provide a more robust solution for maintaining bi-stability. Using FFF samples, thermally induced snap-back behaviour was successfully demonstrated in heated water. Additionally, a heat gun proved to be effective in triggering transitions. However, when localised heating was applied using Peltier elements positioned on either side of the bi-stable element, snap-back behaviour was not observed. This result suggested other factors contributed to the snap-back behaviour in the prior heating techniques. It was further determined that the decrease in yield strength of the beam materials limited the transition temperature range of the programming approach.

Overall, this research provides deeper insight into achieving active programmability of multi-stable mechanical metamaterials and its challenges. The experimental phase highlighted the influence of material properties on the functionality of thermal softening as an active programming approach. Factors such as stress limits, visco-elasticity, and temperature-dependent yield strength of both the active and passive materials define the design margin within which the programming approach can function. As observed in this study, this margin can be narrow, making the realization of a physically functional sample particularly challenging. Nevertheless, the knowledge gained in this research can be incorporated into future work investigating this programming approach.

7.1. Recommendations

Based on the findings of this study, several recommendations can be made for future research on programming multi-stable mechanical metamaterials through thermal stiffness modulation. The key areas of improvement include material selection and design modifications to enhance the feasibility and effectiveness of the approach.

Material Investigation

Further investigation into material selection is essential for optimizing the programmability of the system. The following recommendations address key material-related considerations:

- **Exploring beam materials with significantly higher glass transition temperatures than the support materials.** Alternatively, non-polymer materials, such as metals, could be considered for the beam. This may expand the range of achievable transition temperatures, improving the feasibility of the programming approach.
- **Characterizing additional thermo-mechanical properties,** including yield strength, viscoelasticity, and thermal expansion. Incorporating these properties into finite element analysis (FEA) and using them as constraints in the geometric design space would provide a more comprehensive understanding of their impact on programmability.
- **Investigating creep and relaxation in deformed bi-stable polymer beams** to assess their long-term effectiveness in triggered snap-back behaviour. Polymer beams are expected to relax over time in their deformed state, which could increase the energy threshold required for activation. This may introduce a time-dependent limitation on the programming approach, making it a crucial factor for consideration in compact motion systems.

Design

If an appropriate material selection is achieved, several design strategies can be explored to enhance programmability:

- **Positioning the active material at the component that constrains the second buckling mode.** Given the importance of this constraint in maintaining bi-stability, an actively tunable

second mode constraint could be investigated as a means to trigger snap-back. One potential implementation could involve a parallel-beam structure in which one beam is actively programmable.

- **Experimenting with layered structures** as a method for constraining the second buckling mode. This would provide insight into the effectiveness of the programming approach when applied to tessellated configurations.
- **Developing a programmable dome-shaped unit cell.** The current study focused on unit cells operating within a 2D plane with 1D motion. Extending the approach to dome-shaped unit cells could enable programmable 3D structures for multi-degree-of-freedom (DOF) compact motion systems.
- **Integrating embedded heating elements within the structure** to enable more efficient and targeted actuation without relying on external heating sources. While this study conducted experimentation on unit cells, where simple heating applications were feasible, layered structures may require more complex heating strategies.
- **Exploring non-mechanical strategies for loading the system in the deformed position** while ensuring that the thermal programming approach remains unaffected (e.g. magnetic actuation). The loading actuation can be applied globally since the programming approach should allow for local unloading.

By implementing these recommendations, the understanding of thermal stiffness modulation as a programming approach can be further refined. This will provide deeper insight into its feasibility for enabling precise and addressable motion functionality in multi-stable mechanical metamaterials, ultimately advancing their potential for compact motion systems.

References

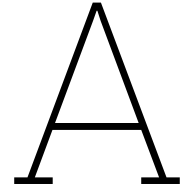
1. Zadpoor, A. A., Mirzaali, M. J., Valdevit, L. & Hopkins, J. B. Design, Material, Function, and Fabrication of Metamaterials. *APL Materials* **11**, 020401 (Feb. 2023).
2. Lu, C. *et al.* Architectural Design and Additive Manufacturing of Mechanical Metamaterials: A Review. *Engineering* **17**, 44–63 (Oct. 2022).
3. Govindaraman, L. T., Arjunan, A., Baroutaji, A., Robinson, J. & Olabi, A.-G. in *Encyclopedia of Smart Materials* (ed Olabi, A.-G.) 522–534 (Elsevier, Oxford, Jan. 2022). ISBN: 978-0-12-815733-6. <https://www.sciencedirect.com/science/article/pii/B9780128157329001273>.
4. Walia, S. *et al.* Flexible metasurfaces and metamaterials: A review of materials and fabrication processes at micro- and nano-scales. *Applied Physics Reviews* **2**, 011303 (Mar. 2015).
5. Valipour, A., Kargozarfard, M. H., Rakhshi, M., Yaghootian, A. & Sedighi, H. M. Metamaterials and their applications: An overview. en. *Proceedings of the Institution of Mechanical Engineers, Part L: Journal of Materials: Design and Applications* **236**, 2171–2210. ISSN: 1464-4207 (Nov. 2022).
6. Barchiesi, E., Spagnuolo, M. & Placidi, L. Mechanical metamaterials: a state of the art. *Mathematics and Mechanics of Solids* **24**, 212–234 (Jan. 2019).
7. Li, X. & Gao, H. Smaller and Stronger. *Nature Mater* **15**, Art. no. 4 (Apr. 2016).
8. Surjadi, J. U. & *et al.* Mechanical Metamaterials and Their Engineering Applications. *Advanced Engineering Materials* **21**, 1800864 (2019).
9. Zheng, X., Zhang, X., Chen, T.-T. & Watanabe, I. Deep Learning in Mechanical Metamaterials: From Prediction and Generation to Inverse Design. *Advanced Materials* **35**, 2302530 (Nov. 2023).
10. Zheng, X. *et al.* Ultralight, ultrastiff mechanical metamaterials. *Science* **344**, 1373–1377 (June 2014).
11. Greaves, G. N., Greer, A., Lakes, R. & Rouxel, T. Poisson’s ratio and modern materials. *Nature Materials* **10**, 823–837 (2011).
12. Lakes, R. Foam Structures with a Negative Poisson’s Ratio. *Science* **235**, 1038–1040 (Feb. 1987).
13. Bell, A. G. The Tetrahedral Principle in Kite Structure. *Natl. Geogr. Mag.* **14**, 219 (June 1903).
14. Peijnenburg, W. *et al.* Identification of emerging safety and sustainability issues of advanced materials: Proposal for a systematic approach. *NanoImpact* **23**, 100342 (July 2021).
15. Jiao, P., Mueller, J., Raney, J., Zheng, X. & Alavi, A. Mechanical metamaterials and beyond. *Nat Commun* **14**, 6004 (Sept. 2023).
16. Zadpoor, A. Mechanical meta-materials. *Mater. Horiz.* **3**, 371–381 (Aug. 2016).
17. Jiao, P. & Alavi, A. H. Artificial intelligence-enabled smart mechanical metamaterials: advent and future trends. *International Materials Reviews* **66**, 365–393 (Aug. 2021).
18. Shan, S. *et al.* Multistable Architected Materials for Trapping Elastic Strain Energy. *Advanced Materials* **27**, 4296–4301 (2015).
19. Yang, H. & Ma, L. Multi-stable mechanical metamaterials by elastic buckling instability. *J Mater Sci* **54**, 3509–3526 (Feb. 2019).
20. Cao, Y., Derakhshani, M., Fang, Y., Huang, G. & Cao, C. Bistable Structures for Advanced Functional Systems. *Advanced Functional Materials* **31**, 2106231 (2021).
21. Shi, J., Mofatteh, H., Mirabolghasemi, A., Desharnais, G. & Akbarzadeh, A. Programmable Multistable Perforated Shellular. *Advanced Materials* **33**, 2102423 (2021).

22. Zhang, Y., Wang, Q., Tichem, M. & van Keulen, F. Design and characterization of multi-stable mechanical metastructures with level and tilted stable configurations. *Extreme Mechanics Letters* **34**, 100593. <https://doi.org/10.1016/j.eml.2019.100593> (2019).
23. Xu, R. *et al.* The design, manufacture and application of multistable mechanical metamaterials—a state-of-the-art review. *Int. J. Extrem. Manuf.* **5**, 042013 (Oct. 2023).
24. Chi, Y. *et al.* Bistable and Multistable Actuators for Soft Robots: Structures, Materials, and Functionalities. *Advanced Materials* **34**, 2110384 (2022).
25. Hussein, H., Moal, P., Bourbon, G., Haddab, Y. & Lutz, P. Modeling and Stress Analysis of a Pre-Shaped Curved Beam: Influence of High Modes of Buckling. *International Journal of Applied Mechanics* **7**, 20 p (2015).
26. Vangbo, M. An analytical analysis of a compressed bistable buckled beam. *Sensors and Actuators A: Physical* **69**, 212–216. ISSN: 0924-4247 (Sept. 1998).
27. Cazottes, P., Fernandes, A., Pouget, J. & Hafez, M. Bistable Buckled Beam: Modeling of Actuating Force and Experimental Validations. *Journal of Mechanical Design* **131**. ISSN: 1050-0472. <https://doi.org/10.1115/1.3179003> (Sept. 2009).
28. Comescaisse, B., Fernandes, A. & Pouget, J. Bistable buckled beam and force actuation: Experimental validations. *International Journal of Solids and Structures* **51**, 1750–1757. ISSN: 0020-7683 (May 2014).
29. Pane, I. Z. & Asano, T. Investigation on Bistability and Fabrication of Bistable Prestressed Curved Beam. en. *Japanese Journal of Applied Physics* **47**, 5291. ISSN: 1347-4065 (June 2008).
30. Qiu, J., Lang, J. H. & Slocum, A. H. A curved-beam bistable mechanism. *Journal of Microelectromechanical Systems* **13**, 137–146 (Apr. 2004).
31. Albertini, F., Tarantino, M. G. & Daniel, L. Mechanical behavior of embedded bistable dome shell with tunable energy barrier asymmetry. *International Journal of Mechanical Sciences* **263**, 108762. <https://linkinghub.elsevier.com/retrieve/pii/S0020740323006641> (2024).
32. *Mechanical Metamaterials for Compact Motion Systems (MECOMOS)* Accessed: Dec. 02, 2023. TU Delft. <https://www.tudelft.nl/3me/over/afdelingen/precision-and-microsystems-engineering-pme/research/mechatronic-system-design-msd/msd-research/mechanical-metamaterials-for-compact-motion-systems-mecomos>.
33. Bloembergen, M. *Internal report: Programmability of Multi-stable Mechanical Metamaterials* tech. rep. (Delft University of Technology, 2024).
34. Qi, J. *et al.* Recent Progress in Active Mechanical Metamaterials and Construction Principles. *Advanced Science* **9**, 2102662 (2022).
35. Decroly, G. *et al.* Programmable Stimuli-Responsive Actuators for Complex Motions in Soft Robotics: Concept, Design and Challenges. en. *Actuators* **9**, 131. ISSN: 2076-0825 (Dec. 2020).
36. Niknam, H., Akbarzadeh, A., Therriault, D. & Bodkhe, S. Tunable thermally bistable multi-material structure. *Applied Materials Today* **28**, 101529 (Aug. 2022).
37. Zhang, Y., Velay-Lizancos, M., Restrepo, D., Mankame, N. D. & Zavattieri, P. D. Architected material analogs for shape memory alloys. en. *Matter* **4**, 1990–2012. ISSN: 25902385 (June 2021).
38. Meng, Z., Qin, W., Mei, T. & Chen, C. Q. Bi-material sinusoidal beam-based temperature responsive multistable metamaterials. *International Journal of Solids and Structures* **277–278**, 112343 (Aug. 2023).
39. Potekhina, A. & Wang, C. Review of Electrothermal Actuators and Applications. en. *Actuators* **8**, 69. ISSN: 2076-0825 (Dec. 2019).
40. Lin, Y. *et al.* Magnetically Induced Low Adhesive Direction of Nano/Micropillar Arrays for Microdroplet Transport. en. *Advanced Functional Materials* **28**, 1800163. ISSN: 1616-3028 (2018).
41. Ramachandran, V., Bartlett, M. D., Wissman, J. & Majidi, C. Elastic instabilities of a ferroelastomer beam for soft reconfigurable electronics. en. *Extreme Mechanics Letters* **9**, 282–290. ISSN: 23524316 (Dec. 2016).

42. Zhang, Y.-L. *et al.* Electro-responsive actuators based on graphene. *The Innovation* **2**, 100168. ISSN: 2666-6758 (Nov. 2021).
43. Ji, Q. *et al.* 4D Thermomechanical metamaterials for soft microrobotics. en. *Communications Materials* **2**, 1–6. ISSN: 2662-4443 (Sept. 2021).
44. Zou, B., Liang, Z. & Ju, J. Coupling of a Magnetic Field With Instability for Multimodal and Multistep Deformations of a Curved Beam With Asymmetric Magnetic Torque. *Journal of Applied Mechanics* **90**, 021001 (Feb. 2023).
45. Abbasi, A., Sano, T. G., Yan, D. & Reis, P. M. Snap buckling of bistable beams under combined mechanical and magnetic loading. *Philosophical Transactions of the Royal Society A: Mathematical, Physical and Engineering Sciences* **381**, 20220029 (Feb. 2023).
46. Stoychev, G., Kirillova, A. & Ionov, L. Light-Responsive Shape-Changing Polymers. en. *Advanced Optical Materials* **7**, 1900067. ISSN: 2195-1071 (2019).
47. Zhang, C. *et al.* A review on reprogrammable bistable structures. en. *Smart Materials and Structures* **33**, 093001. ISSN: 0964-1726 (Aug. 2024).
48. Ji, J., Zhang, K. & Guo, X. Shape memory polymer lattice structures with programmable thermal recovery time. en. *Smart Materials and Structures* **33**, 085027. ISSN: 0964-1726 (July 2024).
49. Zhang, H., Wu, J., Fang, D. & Zhang, Y. Hierarchical mechanical metamaterials built with scalable tristable elements for ternary logic operation and amplitude modulation. *Science Advances* **7**, eabf1966 (Feb. 2021).
50. Che, K., Yuan, C., Qi, H. J. & Meaud, J. Viscoelastic multistable architected materials with temperature-dependent snapping sequence. *Soft Matter* **14**, 2492–2499 (2018).
51. Fu, Z., Zhu, Z. & Deng, Z. Thermally active programmable metamaterials with holey tilted struts. *Smart Mater. Struct.* **33**, 015006 (Dec. 2023).
52. Tao, R. *et al.* 4D printed multi-stable metamaterials with mechanically tunable performance. *Composite Structures* **252**, 112663 (Nov. 2020).
53. TA Instruments. Introduction to Dynamic Mechanical Analysis and its Application to Testing of Polymer Solids. *TA Instruments Technical Note*. Accessed: 2024-02-22. <https://www.tainstruments.com/> (2023).
54. Vilar, Z. T., Grassi, E. N. D., de Oliveira, H. M. R. & de Araujo, C. J. Use of Dynamic Mechanical Analysers to Characterize Shape Memory Alloys: Cautions and Considerations from an Experimental Analysis. *International Journal of Thermophysics* **44** (2023).
55. Landel, R. F. & Nielsen, L. E. *Mechanical Properties of Polymers and Composites* en. Google-Books-ID: 10xUDwAAQBAJ. ISBN: 978-1-4822-7743-2 (CRC Press, Dec. 1993).
56. *Beam theory: Stiffness of combined loads* en. <https://www.jpe-innovations.com/precision-point/beam-theory-stiffness-combined-loads/>.
57. Choudhury, S. S., Pandey, M. & Bhattacharya, S. Recent Developments in Surface Modification of PEEK Polymer for Industrial Applications: A Critical Review. en. *REVIEWS OF ADHESION AND ADHESIVES* **9**. <https://raajournal.com/menuscript/index.php/raajournal/article/view/138> (Dec. 2021).
58. Alvaredo-Atienza, Á., Chen, L., San-Miguel, V., Ridruejo, Á. & Fernández-Blázquez, J. P. Fabrication and Characterization of PEEK/PEI Multilayer Composites. en. *Polymers* **12**, 2765. ISSN: 2073-4360 (Dec. 2020).
59. Hua, J., Zhou, Y. & Chen, C. Q. Design and analysis of a tunable multistable mechanical metamaterial. *International Journal of Mechanical Sciences*, 109170 (Mar. 2024).
60. Timoshenko, S. & Gere, J. *Theory of Elastic Stability* ISBN: 978-0-486-13480-2. <https://books.google.nl/books?id=98B6J0W2HiUC> (Dover Publications, 2012).
61. Hussein, H., Khan, F. & Younis, M. I. A monolithic tunable symmetric bistable mechanism. *Smart Mater. Struct.* **29**, 075033 (June 2020).
62. Beer, F. P. *Mechanics of materials* Seventh edition. en. ISBN: 978-0-07-339823-5 (McGraw-Hill Education, New York, NY, 2015).

63. DesignerData. *Polyetheretherketone (PEEK) - Material Properties* 2024. <https://designerdata.nl/materials/plastics/thermo-plastics/polyetheretherketone>.
64. Islam, M. A. *et al.* Additive manufacturing in polymer research: Advances, synthesis, and applications. *Polymer Testing* **132**, 108364. ISSN: 0142-9418 (Mar. 2024).
65. Yuan, C., Wang, F., Rosen, D. W. & Ge, Q. Voxel design of additively manufactured digital material with customized thermomechanical properties. *Materials Design* **197**, 109205. ISSN: 0264-1275 (Jan. 2021).
66. Gomez, M., Moulton, D. E. & Vella, D. Dynamics of viscoelastic snap-through. *Journal of the Mechanics and Physics of Solids* **124**, 781–813. ISSN: 0022-5096 (Mar. 2019).
67. Richter, F. & Wu, D. Interfacial adhesion between dissimilar thermoplastics fabricated via material extrusion-based multi-material additive manufacturing. *Materials Design* **252**, 113688. ISSN: 0264-1275 (Apr. 2025).
68. Wang, S., Ma, Y., Deng, Z., Zhang, S. & Cai, J. Effects of fused deposition modeling process parameters on tensile, dynamic mechanical properties of 3D printed polylactic acid materials. *Polymer Testing* **86**, 106483. ISSN: 0142-9418 (June 2020).
69. Subbarao, C. V., Reddy, Y. S., Inturi, V. & Reddy, M. I. Dynamic Mechanical Analysis of 3D Printed PETG Material. en. *IOP Conference Series: Materials Science and Engineering* **1057**, 012031. ISSN: 1757-899X (Feb. 2021).
70. Hua, J., Lei, H., Gao, C.-F. & Fang, D. A Novel Design of Multistable Metastructure With Nonuniform Cross Section. *Journal of Applied Mechanics* **89** (Mar. 2022).
71. Liang, K. *et al.* Programmable and multistable metamaterials made of precisely tailored bistable cells. *Materials & Design* **227**, 111810 (Mar. 2023).
72. Huang, P.-Y., Guo, Z.-S. & Feng, J.-M. General Model of Temperature-dependent Modulus and Yield Strength of Thermoplastic Polymers. en. *Chinese Journal of Polymer Science* **38**, 382–393. ISSN: 1439-6203 (Apr. 2020).
73. Vaňková, T., Kroupa, T., Zemčík, R., Krystek, J. & Zemčík, H. Identification of temperature-dependent parameters for an elastic–plastic–damage material model of 3D-printed PETG. *Polymer* **284**, 126295. ISSN: 0032-3861 (Oct. 2023).
74. *Nanoscribe Photoresins Specifically Designed for Two-Photon Polymerization* Photoresins Specifically for Two-Photon Polymerization. www.nanoscribe.com/en/products/ip-photoresins/#tab-15622. Year. (2024).
75. Frenzel, T. *et al.* Tailored Buckling Microlattices as Reusable Light-Weight Shock Absorbers. *Advanced Materials* **28**, 5865–5870 (2016).
76. Che, K., Yuan, C., Wu, J., Qi, H. J. & Meaud, J. Three-Dimensional-Printed Multistable Mechanical Metamaterials With a Deterministic Deformation Sequence. *Journal of Applied Mechanics* **84** (Oct. 2016).
77. Yang, H. & Ma, L. 1D to 3D multi-stable architected materials with zero Poisson’s ratio and controllable thermal expansion. *Materials & Design* **188**, 108430 (Mar. 2020).
78. Chen, B. *et al.* Novel multifunctional negative stiffness mechanical metamaterial structure: Tailored functions of multi-stable and compressive mono-stable. *Composites Part B: Engineering* **204**, 108501 (Jan. 2021).
79. Giri, T. R. & Mailen, R. Controlled snapping sequence and energy absorption in multistable mechanical metamaterial cylinders. *International Journal of Mechanical Sciences* **204**, 106541 (Aug. 2021).
80. Mofatteh, H. *et al.* Programming Multistable Metamaterials to Discover Latent Functionalities. *Advanced Science* **9**, 2202883 (2022).
81. Jules, T., Reid, A., Daniels, K. E., Mungan, M. & Lechenault, F. Delicate memory structure of origami switches. *Phys. Rev. Research* **4**, 013128 (Feb. 2022).
82. Ghavidelnia, N., Yin, K., Cao, B. & Eberl, C. Curly beam with programmable bistability. *Materials & Design* **230**, 111988 (June 2023).

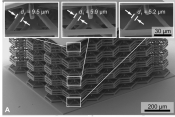
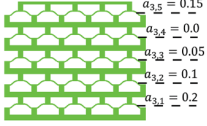
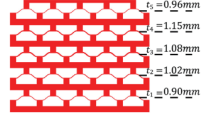
83. Hyatt, L. P. & Harne, R. L. Programming metastable transition sequences in digital mechanical materials. *Extreme Mechanics Letters* **59**, 101975 (Mar. 2023).
84. Hu, W. *et al.* Deformation behavior and band gap switching function of 4D printed multi-stable metamaterials. *Materials & Design* **200**, 109481 (Feb. 2021).
85. Jafarabadi, A., Ferretto, I., Mohri, M., Leinenbach, C. & Ghafoori, E. 4D printing of recoverable buckling-induced architected iron-based shape memory alloys. *Materials & Design* **233**, 112216 (Sept. 2023).
86. Xin, X., Liu, L., Liu, Y. & Leng, J. 4D Printing Auxetic Metamaterials with Tunable, Programmable, and Reconfigurable Mechanical Properties. *Advanced Functional Materials* **30**, 2004226 (2020).
87. Aldawood, F. K. A Comprehensive Review of 4D Printing: State of the Arts, Opportunities, and Challenges. *Actuators* **12**, 3 (Mar. 2023).
88. Novelino, L. S., Ze, Q., Wu, S., Paulino, G. H. & Zhao, R. Untethered control of functional origami microrobots with distributed actuation. *Proceedings of the National Academy of Sciences* **117**, 24096–24101 (Sept. 2020).
89. Tan, X. *et al.* Real-time tunable negative stiffness mechanical metamaterial. *Extreme Mechanics Letters* **41**, 100990 (Nov. 2020).
90. Korpas, L. M., Yin, R., Yasuda, H. & Raney, J. R. Temperature-Responsive Multistable Metamaterials. *ACS Applied Materials & Interfaces* **13**, 31163–31170 (July 2021).
91. Chen, T., Pauly, M. & Reis, P. M. A reprogrammable mechanical metamaterial with stable memory. *Nature* **589** (Jan. 2021).
92. Zhao, Z. & Zhang, X. S. Encoding reprogrammable properties into magneto-mechanical materials via topology optimization. *npj Comput Mater* **9** (Apr. 2023).



Literature review

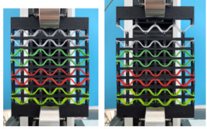
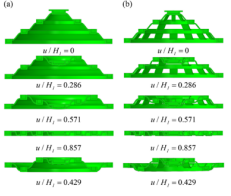
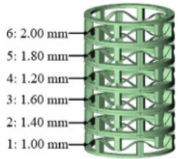
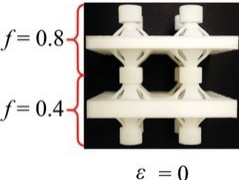
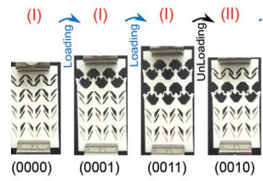
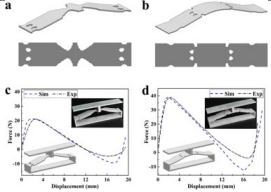
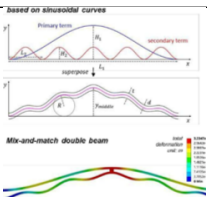
Passive programmability is manifested in the design phase, and the programmed behaviour cannot be altered post-fabrication. Passive programmability primarily makes use of geometric variation to alter the stiffness of a unit cell or row of unit cells. The main methods to achieve this are either by changing the dimensions of the elements or by changing the shape/topology of the buckling element. These different approaches will be explored with the use of a few examples from existing literature which are listed in the table A.1. The **Types** of examples are categorized as Dimensional adjustment (D) or Shape/topological adjustment (S), and with distinction between variance per row or per unit cell. The **Function** column refers to the function intended by the authors of the paper. The **2D/3D** column indicates in how many dimensions the unit cell is adjusted for programming. The **Unit cell size** column gives a close estimation to the volume of one unit cell. Lastly the **Material** and **Author/Publishing Date** are provided.

A.1. State of the art passive programmability

Image	Type (Level)	Function	2D/3D	Unit cell size	Material	Author (Date)
	D Row	Shock absorption	3D	$100\mu m \times 100\mu m \times 100\mu m$	IP-S ¹	Frenzel et al. [75] (2016)
	S Row	Shape morphing	2D	$20\text{ mm} \times 20\text{ mm} \times 10\text{ mm}$	DM9895 ²	Che et al. [76] (2016)
	D Row	Shape morphing	2D	$20\text{ mm} \times 20\text{ mm} \times 10\text{ mm}$	DM9895	Che et al. [76] (2016)

¹Resin material by Nanoscribe for applications such as mechanical metamaterials [74]

²A digital material derived by mixing two base materials: TangoblackPlus and Verowhite[76]

	D Row	Energy absorption	2D	27 mm × 15 mm × 1 mm	GBR-PA12 ³	Yang et al. [77] (2020)
	S Unit Cell	Energy absorption	3D	74 mm × 74 mm × 47 mm	TPU ⁴	Chen et al. [78] (2021)
	D Row	Energy absorption	2D	77.48 mm × 41.78 mm × 12.70 mm	TPU	Giri et al. [79] (2021)
	D/S Unit Cell	Shape morphing	3D	50 mm × 50 mm × 50 mm	TPU	Shi et al. [21] (2021)
	D Row	Mechanical memory	2D	40 mm × 33 mm × 30 mm	TPU	Mofatteh et al. [80] (2022)
	S Row	Energy absorption	2D	60 mm × 9 mm × 1 mm	Nylon	Hua et al. [70] (2022)
	D Row	Shape morphing	2D	32 mm × 32 mm × 65 mm	Mylar sheet	Jules et al. [81] (2022)
	S Row	Shape morphing	2D	55 mm × 5 mm × 0.55 mm (beam size)	PLA	Ghavidelnia et al. [82] (2023)

³HP Jet Fusion 3D 4200 printing material with (black) glass beads reinforced with polyamide 12

⁴The flexible buckling elements are made of TPU (thermoplastic polyurethane) and the rigid elements are made of PLA (polylactic acid).

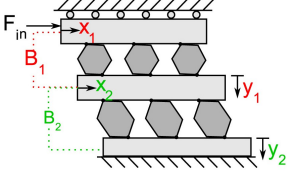
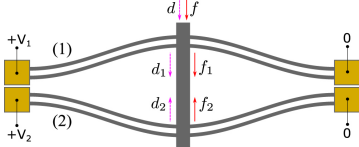
	S Row	computing functional- ity	2D	10 mm × 10 mm × 15 mm	polyurethane rubber	Hyatt et al. [83] (2023)
-----------------------------------------------------------------------------------	----------	---------------------------------	----	--------------------------	------------------------	--------------------------------

Table A.1: State-of-the-art passively programmed bi-/multi-stable structures

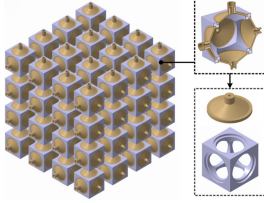
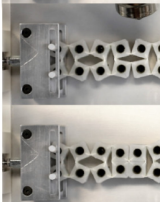
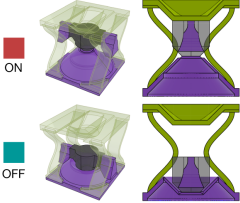
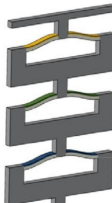
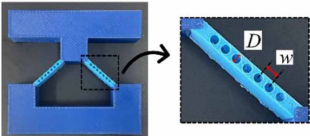
A.2. State of the art active programmability

In literature, active programming can also be referred to as 4D programming/printing [52, 84–86]. In those examples, 4D refers to the added dimension of the material’s response to environmental stimuli over time. This method is not limited to metamaterials and has a broad range of applications in fields such as electronics, renewable energy, aerospace, food, healthcare, and fashion wear [87]. Using external stimuli to activate a metamaterial makes it possible to program the system post-fabrication, thereby expanding the tunability compared to passively programmed structures. In Table A.2, multiple examples from literature are presented which make use of this attractive feature. Some of these structures use a combination of passive programming (geometric adjustment) and active programming (stimuli-dependence), in order to achieve a certain deformation sequence. The examples presented are either Thermally or Magnetically stimulated. Notably, these two methods are less comparable to each other than the passive programming methods (dimensional vs shape adjustment). The thermal stimuli soften materials with increased heat, achieving one directional state changes, whereas magnetic stimuli can achieve bi-directional actuation. Table A.2 shows an **image** of the approaches from recent literature. The **External stimuli** column indicates which stimulus is used and whether it is applied globally or locally. Note, a state change may still occur only on one layer even if the stimulus is applied globally. Next the **Function** mentioned by the authors is noted, followed by the size of a single unit cell, the materials used and the author and publishing date.

Image	External stimuli	Function	Unit cell size	Material	Author (Date)
	Thermal (Global)	Tunable stiffness	12 mm × 7 mm × 6 mm	PEGDA DM9895 ⁵	Che et al. [50] (2018)
	Thermal (Global)	Controllable deforma- tion	14 mm × 6.2 mm × 10 mm	RGD8530 VeroWhite 6	Tao et al. [52] (2020)
	Thermal (Local)	Tunable deforma- tion	2 mm (length)	Doped silicon	Hussein et al. [61](2020)

⁵DM9895 is a digital material obtained by mixing the two base materials of the printer, TangoBlack and VeroWhite

⁶These digital SMP materials are directly printed by a multi-material inkjet 3D printer (Objet 350, Stratasys, USA) capable of precisely printing digital polymer materials with various thermomechanical properties.

	Magnetic (Global)	Shape transform- ing	21 mm × 24 mm × 24 mm	Origami- paper silicone rubber NdFeB ⁷	Novelino et al. [88] (2020)
	Air pressure (global)	tunable stiffness	20 mm × 20 mm × 5 mm (cone size)	urethane elastomer	Tan et al. [89] (2020)
	Thermal (Local)	Shape adaption	20 mm × 20 mm × 20 mm	LCE/PDMS ⁸	Korpas et al. [90] (2021)
	Magnetic (Local)	Tunable stiff- ness/strength	30 mm × 30 mm × 30 mm	VPS/NdFeB ⁹	Chen et al. [91] (2021)
	Thermal (Global)	Self- sensing actuators	50 mm × 80 mm ×	TPU/CFR Nylon	Niknam et al. [36] (2022)
	Thermal (Global)	Shock at- tenuation	66 mm × 10 mm × 6 mm (beam)	PLA/TPU	Meng et al. [38] (2023)
	Thermal (Global)	Self- induced actuators	100 mm × 6 mm × 30 mm (beam)	TPU/PETG	Fu et al. [51] (2023)

⁷3-mm-thick magnetized plate that is made from a mix of Ecoflex 00-30 silicone rubber and NdFeB (neodymium–iron–boron) particles (30 vol%) [88]

⁸A silicone, poly(dimethylsiloxane) (PDMS), and a temperature-responsive liquid crystal elastomer (LCE) are joined via a silicone sealant

⁹ The magnetic cap is cast using an elastomer composite made of vinyl polysiloxane (VPS) mixed with magnetized NdFeB particles.

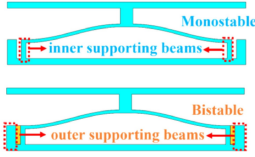
	Magnetic (Global)	Adaptable snap buckling	60 mm × 6 mm × 8 mm	PDMS/ NdFeB	Zhao et al. [92] (2023)
	Magnetic (Global)	Multimodal transfor- mation	23 mm × 0.6 mm × 3 mm (beam)	PDMS/ NdFeB	Zou et al. [44] (2023)
	Mechanical (Local)	Tunable load- bearing	60 mm × 1 mm × 15 mm (beam)	nylon	Hua et al. [59] (2024)

Table A.2: State-of-the-art approaches to active programming of multi-stable mechanical metamaterials

B

Continuation of Analytical Model fixed-fixed boundary conditions

By combining the normalisations in eqs. (4.15) and (4.20) and the mode superposition in eqs. (4.16) to (4.19) , the relations in eqs. (4.9) to (4.14) can now be expressed as

$$\Delta = 1 - 2 \sum_{j=1,5,9,13,\dots} A_j \quad (\text{B.1})$$

$$S = 1 + \sum_{j=1}^{\infty} \frac{A_j^2 N_j^2}{4} \quad (\text{B.2})$$

$$\frac{N^2}{12Q^2} = (S)_{W=\bar{w}} = S = \frac{N_1^2}{16} - \sum_{j=1}^{\infty} \frac{A_j^2 N_j^2}{4} \quad (\text{B.3})$$

$$\partial(U_b) = \partial \left[\frac{(\frac{1}{2} - A_1)^2 N_1^4}{4} + \sum_{j=2}^{\infty} \frac{A_j^2 N_j^4}{4} \right] \quad (\text{B.4})$$

$$\partial(U_s) = -N^2 \partial(S) = -N^2 \partial \left(\sum_{j=1}^{\infty} \frac{A_j^2 N_j^2}{4} \right) \quad (\text{B.5})$$

$$\partial(U_f) = -F \partial(\Delta) = 2F \sum_{j=1,5,9,13,\dots} A_j \quad (\text{B.6})$$

The variation of the total energy, U_t , within the buckling beam is the sum of eqs. (B.4) to (B.6), which results in

$$\begin{aligned} \partial(U_t) &= \left(\frac{N_1^4 - N^2 N_1^2}{2} A_1 - \frac{N_1^4}{4} + 2F \right) \partial(A_1) \\ &+ \sum_{j=2,3,4,6,7,\dots} \left(\frac{N_j^4 - N^2 N_j^2}{4} \right) \partial(A_j^2) \\ &+ \sum_{j=5,9,13,\dots} \left(\frac{N_j^4 - N^2 N_j^2}{2} A_j + 2F \right) \partial(A_j) \end{aligned} \quad (\text{B.7})$$

The mode amplitudes should minimize U_t , therefore

$$\partial(U_t) \geq 0 \quad (\text{B.8})$$

In order to satisfy eq. (B.8), the coefficients of $\partial(A_j)$, $j = 1, 5, 9, 13 \dots$ terms in eq. (B.7) should be zero. This yields the solutions

$$A_1 = -\frac{1}{2} \frac{N_1^2}{N^2 - N_1^2} + \frac{4F}{N_1^2 (N^2 - N_1^2)} \quad (\text{B.9})$$

$$A_j = \frac{4F}{N_j^2 (N^2 - N_j^2)}, \quad \text{for } j = 5, 9, 13, \dots \quad (\text{B.10})$$

The $\partial(A_j^2)$, $j = 2, 3, 4, 6, 7 \dots$ terms in eq. (B.7) must also satisfy eq. (B.8) which leads to a number of conclusions.

$$A_j^2 \begin{cases} = 0 & N^2 < N_j^2 \\ \text{must have been constrained} & N^2 > N_j^2 \\ \text{can take any value as long as} & N^2 = N_j^2 \end{cases} \quad j = 2, 3, 4, 6, 7 \dots \quad (\text{B.11})$$

Since only the second mode can be easily constrained mechanically, without affecting the first mode, the second condition dictates that j can only take the value of 2 when the second mode is not constrained, or 3 when the second mode is constrained. This results in three solutions whereby the first kind is

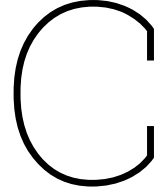
$$\begin{cases} F = F_1 \\ N^2 < \begin{cases} N_1^2, & \text{with the second mode constrained} \\ N_2^2, & \text{with the second mode not constrained} \end{cases} \\ A_j = 0, \quad j \neq 1, 5, 9, 13, \dots \end{cases} \quad (\text{B.12})$$

the second kind is

$$\begin{cases} F = F_2 \\ N^2 = N_2^2 \\ A_j = 0, \quad j \neq 1, 2, 5, 9, 13, \dots \end{cases} \quad (\text{B.13})$$

and the third kind is

$$\begin{cases} F = F_3 \\ N^2 = N_3^2 \\ A_j = 0, \quad j \neq 1, 3, 5, 9, 13, \dots \end{cases} \quad (\text{B.14})$$



Passive vs Active programmability

Active programmability offers an increased amount of control of multi-stable mechanical metamaterial versus passive programmability. The level of programmability of a one-degree-of-freedom (1-DOF) multi-stable metamaterial composed of stacked bi-stable layers can be calculated. For this calculation, Pascal's triangle can serve as a representation of a system with n layers (fig. C.1).

$n = 0$		1				$2^0 = \mathbf{1}$		
$n = 1$		1	1			$2^1 = \mathbf{2}$		
$n = 2$		1	2	1		$2^2 = \mathbf{4}$		
$n = 3$		1	3	3	1	$2^3 = \mathbf{8}$		
$n = 4$		1	4	6	4	1	$2^4 = \mathbf{16}$	
$n = 5$		1	5	10	10	5	1	$2^5 = \mathbf{32}$

Figure C.1: Pascal's triangle labelled by row number n and corresponding sums 2^n .

A system with n layers has 2^n unique stable positions, which corresponds to the sum of all elements in the n^{th} row of Pascal's triangle. However, it is important to note that the heights of these stable positions may not always be unique, as multiple combinations of open and closed layers can result in the same overall height. Each element in Pascal's triangle represents a binomial coefficient:

$$\binom{n}{k} = \frac{n!}{k!(n-k)!} \quad (\text{C.1})$$

where k represents the horizontal position of the element in the row. The first element in a row is indexed as $k = 0$, and the last element is indexed as $k = n$. Each row in Pascal's triangle can be interpreted as a representation of the possible configurations of a system with n layers:

- 0 represents a layer in its open position.
- 1 represents a layer in its closed position.

A fully open system has all n layers at 0, while a fully closed system has all n layers at 1. These two extreme states correspond to the outermost ones in the n^{th} row of Pascal's triangle. Between these extremes in the n^{th} , the binomial coefficient dictates how many configurations exist with exactly k closed layers in a system with n layers. For example:

- A system with two layers ($n = 2$) has one fully open $(0,0)$, one fully closed $(1,1)$ and two configurations where one layer is closed:

$$(0, 1), \quad (1, 0)$$

- A system with three layers has one fully open $(0,0,0)$, one fully closed $(1,1,1)$ and:

- three configurations where one layer is closed:

$$(1, 0, 0), \quad (0, 1, 0), \quad (0, 0, 1)$$

- three configurations where two layers are closed:

$$(1, 1, 0), \quad (1, 0, 1), \quad (0, 1, 1)$$

This pattern continues for larger systems. Now, consider a passively programmed system where the deformation sequence is predefined by the geometry of each layer, and the system can only be globally loaded or unloaded, one layer at a time. In this case, we are interested in calculating the number of paths available to transition between the 2^n stable configurations. The behaviour of the system is constrained by the following rules:

1. From the fully open state, the system can only transition to a state where exactly one layer is closed. This is uniquely determined by the geometry of the weakest layer, meaning only one path exists to the next configuration.
2. Similarly, from the fully closed state, the system can only transition to a state where exactly one layer is open, which is again pre-determined by the geometry so there is only one.
3. Any intermediate configurations can either be loaded or unloaded, meaning each has two possible outward paths leading to different configurations.

Thus, the number of possible transitions follows a simple summation of the outward paths at each step, leading to a final derivation of P_n number of paths:

$$P_n = 2 \cdot 1 + (2^n - 2) \cdot 2 = 2^{n+1} - 2 \quad (\text{C.2})$$

An example of a system with 2 layers is presented in fig. C.2.

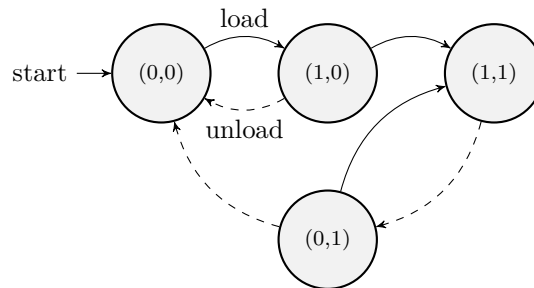


Figure C.2: Passive: Mechanical Loading and Unloading

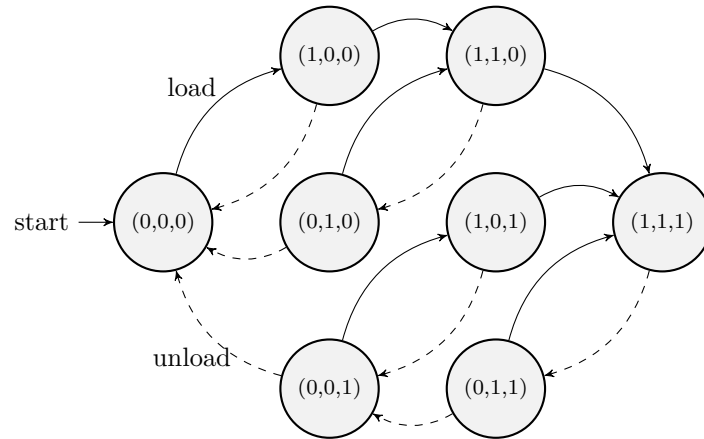


Figure C.3: Passive: Mechanical Loading and Unloading for $n = 3$

Notice that in the system with $n = 2$ layers, to go from $(1,1)$ to $(1,0)$ the system first needs to fully open to $(0,0)$ and then load once, so three loading and unloading steps are required. For a system with $n = 3$ layers, to move from $(1,1,1)$ to $(1,1,0)$ it would require three unloading steps and two loading steps, as can be seen in fig. C.3. The number of minimum steps between some states will drastically increase.

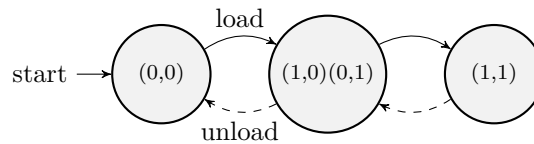


Figure C.4: Passive: Mechanical Loading and Unloading

Naturally, this issue does not arise in systems with equally sized layers, as each configuration with k closed layers would result in the same height. In this case, there would only be $n + 1$ unique height levels, as illustrated in fig. C.4 for a system with $n = 2$ layers. By contrast, if all 2^n configurations correspond to unique heights, a system with 10 layers would have 1024 distinct height positions, whereas a system with equally sized layers would be limited to just 11 unique heights. While the system with identical layers still possesses 1024 possible configurations to reach those 11 heights, this highlights the inefficiency of such a setup for use in positioning systems. Thus, for the effective use of multi-stable mechanical metamaterials in positioning applications, it is advantageous to design systems with multi-sized layers. However, with this added complexity comes the need for active addressability between configurations, allowing transitions beyond what is possible through passive programmability alone.

To improve the programmability of such a system, an alternative approach is to introduce active transitioning, where an external stimulus is applied to directly move between stable states. Unlike the passive system, which follows a strictly predetermined sequence, active transitioning allows for more efficient repositioning. In this work, the desired active programmability assumes:

- Active transitioning is only possible in one direction (unloading).
- The stimulus can be applied locally, allowing multiple layers to be transitioned simultaneously.
- The system still requires a global loading force for deformation.

To demonstrate the increase in newly accessible transition paths, we refer back to Pascal's triangle. As stated, the passively programmed system has $2^{n+1} - 2$ paths. In the active system, every configuration with more than one closed layer gains additional paths. Note that all configurations already have an existing passively determined path, and that a system with a certain i^{th} layer open, cannot transition to a system with the i^{th} layer closed simply by unloading. Remember that there are $\binom{n}{k}$ for each system with k layers closed. So for each state with $k \geq 1$ the additional paths are $\binom{n}{k} \cdot (2^k - 2)$. Adding this to the existing paths from the passively programmed system results in.

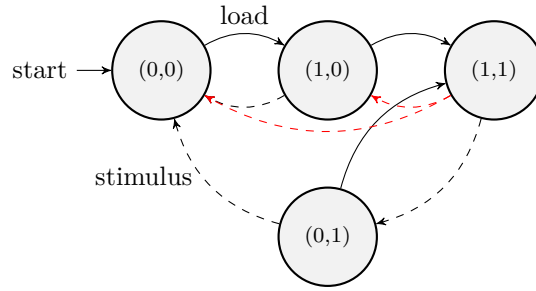


Figure C.5: Active: Mechanical loading and external stimulus for $n = 3$

$$P_{na} = 2^{n+1} - 2 + \sum_{k=1}^n \binom{n}{k} (2^k - 2) \quad (\text{C.3})$$

This equation also seems to correspond to the more simple equation $3^n - 1$. To illustrate the effect, a system with $n = 2$ and $n = 3$ layers is presented in figs. C.5 and C.6, respectively.

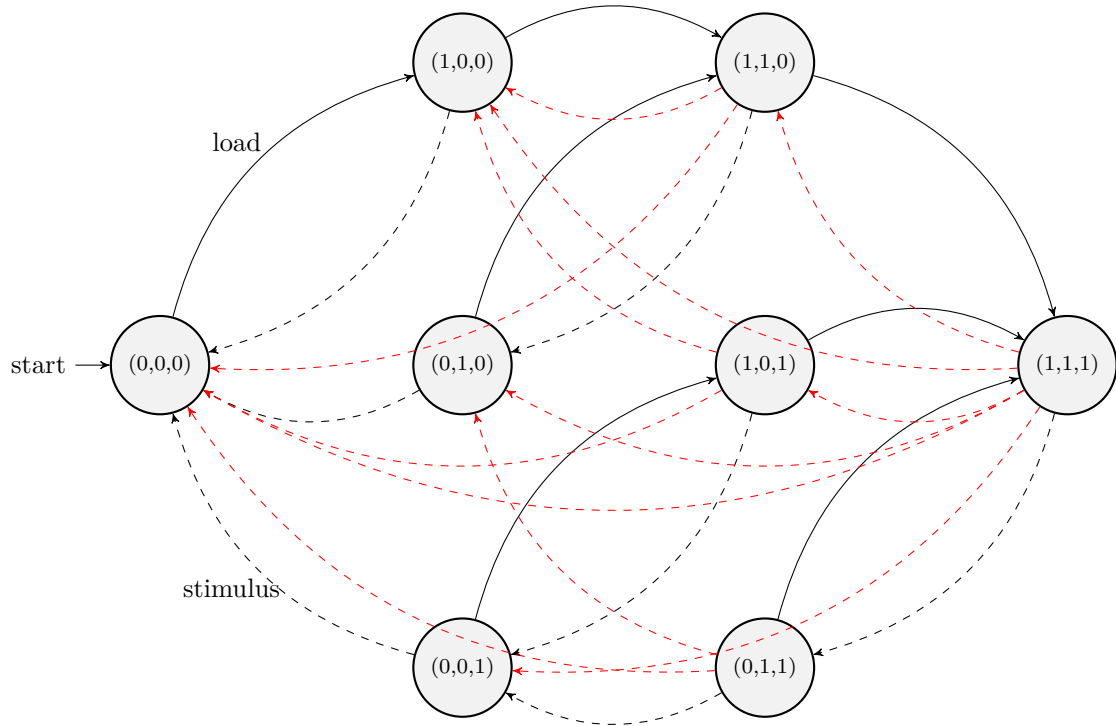


Figure C.6: Active: Mechanical Loading and external stimulus for $n = 3$

We can now plot the paths accessible in both passive and active programmability versus the number of layers. Note that this demonstrates the increase of addressability specifically for one-directional programmability (in unloading). In addressable loading there is still room for improvement. For bi-directional programmability which can be applied locally and simultaneously, all configurations can transition in one step to any configuration resulting in:

$$P_{ba} = 2^n \cdot (2^n - 1) = 2^{2n} - 2^n \quad (\text{C.4})$$

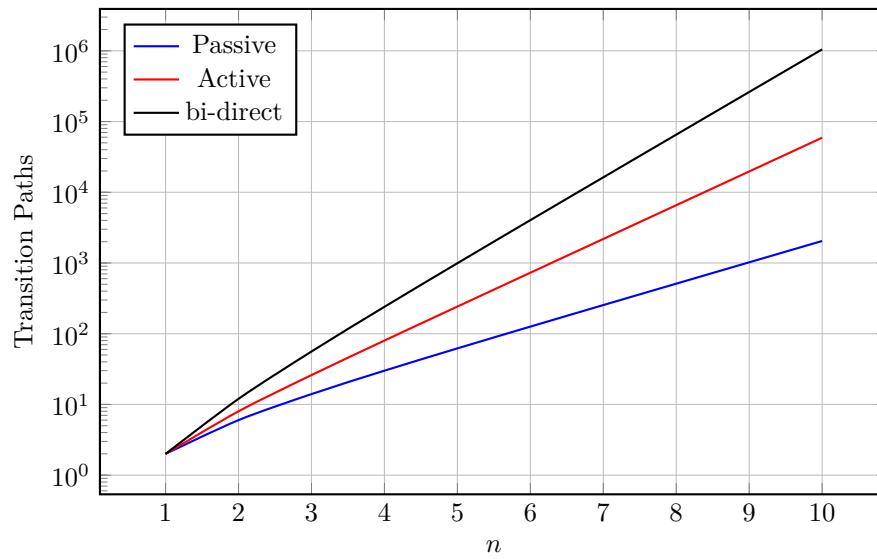


Figure C.7: Comparison of Transition Paths for Passive and Active Systems